

AD-A145 353

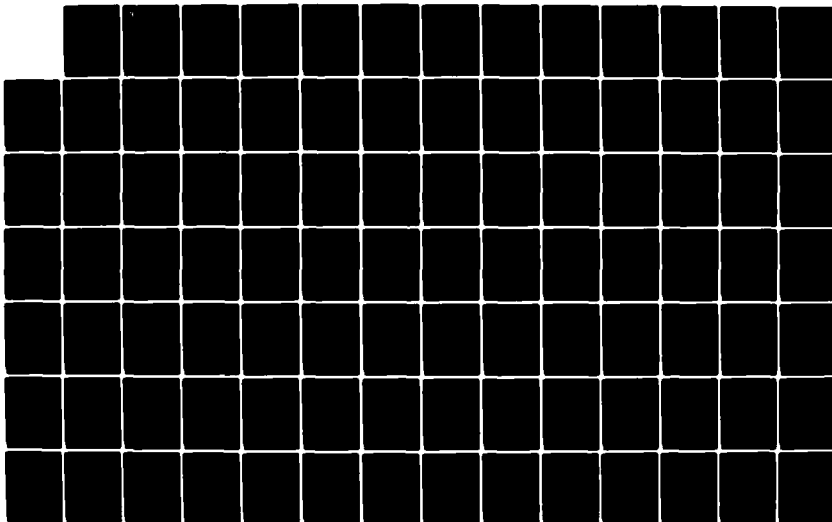
CONSIDERATIONS ON THE RETRIEVAL OF PLUME PARTICLE
PROPERTIES FROM THE AFR. (U) AEROSPACE CORP EL SEGUNDO
CA S J YOUNG AUG 84 TR-0084(4623-02)-2 AFRPL-TR-84-047
F04701-83-C-0084

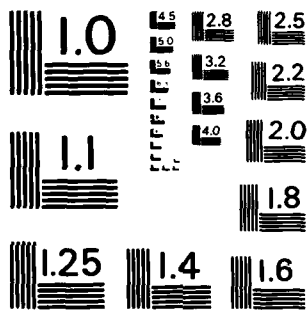
1/2

UNCLASSIFIED

F/G 20/8

NL





MICROCOPY RESOLUTION TEST CHART
NATIONAL BUREAU OF STANDARDS-1963-A



AFRPL TR-84-047

AD:

Final Report
for the period
April 1983 to
June 1984

Considerations on the Retrieval of Plume Particle Properties from the AFRPL Transmissometer and Polarization-Scattering Experiments

August 1984

Authors:
S. J. Young

The Aerospace Corporation
El Segundo, California 90245

TR-0084(4623-02)-2
F04701-83-C-0084

Approved for Public Release

Distribution unlimited. The AFRPL Technical Services Office has reviewed this report, and it is releasable to the National Technical Information Service, where it will be available to the general public, including foreign nationals.

prepared for the: **Air Force
Rocket Propulsion
Laboratory**

Air Force Space Technology Center
Space Division, Air Force Systems Command
Edwards Air Force Base,
California 93523

AD-A145353

FILE COPY


NOTICE

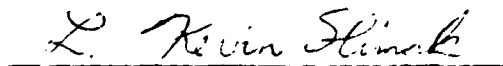
When U.S. Government drawings, specifications, or other data are used for any purpose other than a definitely related Government procurement operation, the Government thereby incurs no responsibility nor any obligation whatsoever, and the fact that the Government may have formulated, furnished, or in any way supplied the said drawings, specifications, or other data is not to be regarded by implication or otherwise, or in any manner licensing the holder or any other person or corporation, or conveying any rights or permission to manufacture, use, or sell any patented invention that may be related thereto.

FOREWORD

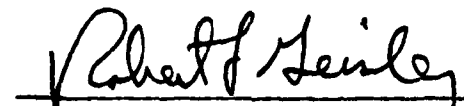
This final report was submitted by Aerospace Corporation, El Segundo, California 90245, under Contract No. F04701-83-C-0084 with the Air Force Rocket Propulsion Laboratory, Edwards AFB, California 93523, under Air Force Project Task 314800AP. The report documents the development of rocket exhaust plume particle size retrieval methodologies including the Single-Color Transmissometer Plume Diagnostic Code (A32CODE). A User's Manual which describes the operation of the A32CODE has also been published as AFRPL-TR-84-048.

This report has been reviewed and approved for publication in accordance with the distribution statement on the cover and on the DD form 1473.


JAMES A. MISENER, 2LT, USAF
Project Manager


L. KEVIN SLIMAK
Chief, Interdisciplinary Space Tech Br

FOR THE DIRECTOR


ROBERT L. GEISLER
Chief, Propulsion Analysis Division

AD-A145254

SECURITY CLASSIFICATION OF THIS PAGE

REPORT DOCUMENTATION PAGE

| | | | | |
|---|-------|--|---|---|
| 1a. REPORT SECURITY CLASSIFICATION UNCLASSIFIED | | | 1b. RESTRICTIVE MARKINGS | |
| 2a. SECURITY CLASSIFICATION AUTHORITY | | | 3. DISTRIBUTION/AVAILABILITY OF REPORT Approved for Public Release; Distribution Unlimited | |
| 2b. DECLASSIFICATION/DOWNGRADING SCHEDULE | | | | |
| 4. PERFORMING ORGANIZATION REPORT NUMBER(S) TR-0084(4623-02)-2 | | | 5. MONITORING ORGANIZATION REPORT NUMBER(S) AFRPL-TR-84-047 | |
| 6a. NAME OF PERFORMING ORGANIZATION The Aerospace Corporation | | 6b. OFFICE SYMBOL (If applicable) | | 7a. NAME OF MONITORING ORGANIZATION Air Force Rocket Propulsion Laboratory |
| 6c. ADDRESS (City, State and ZIP Code) El Segundo CA 90245 | | | 7b. ADDRESS (City, State and ZIP Code) Stop 24 Edwards AFB CA 93523 | |
| 8a. NAME OF FUNDING/SPONSORING ORGANIZATION Space Division | | 8b. OFFICE SYMBOL (If applicable) | | 9. PROCUREMENT INSTRUMENT IDENTIFICATION NUMBER F04701-83-C-0084 |
| 8c. ADDRESS (City, State and ZIP Code) Los Angeles Air Force Station Los Angeles CA 90009 | | | 10. SOURCE OF FUNDING NOS. | |
| | | | PROGRAM ELEMENT NO. 62302F | TASK NO. 00 |
| | | | PROJECT NO. 3148 | WORK UNIT NO. AP |
| 11. TITLE (Include Security Classification) Considerations on the Retrieval of Plume Particle Properties from ... | | | | |
| 12. PERSONAL AUTHOR(S) Young, Stephen J. | | | | |
| 13a. TYPE OF REPORT Final | | 13b. TIME COVERED FROM 83/04 TO 84/06 | | 14. DATE OF REPORT (Yr. Mo., Day) 84/08 |
| 15. PAGE COUNT 129 | | | | |
| 16. SUPPLEMENTARY NOTATION | | | | |
| 17. COSATI CODES | | | 18. SUBJECT TERMS (Continue on reverse if necessary and identify by block number) | |
| FIELD | GROUP | SUB. GR. | | |
| 21 | 08 | | Low visibility rocket plumes Retrieval diagnostics | |
| | | | Plume diagnostics | |
| | | | Plume particulates | |
| 19. ABSTRACT (Continue on reverse if necessary and identify by block number) Assessment is made of the usefulness of data currently being obtained in two particle-diagnostic experiments at Air Force Rocket Propulsion Laboratory (AFRPL). In one experiment, simple laser transmission measurements are made over a full diameter line of sight through the plume. It is shown here that the measured degree of beam attenuation caused by plume particle absorption and scattering, and from auxiliary knowledge of the total mass loading in the plume, a measure of the mean particle size can be deduced to accuracies of < 20% even when the index of refraction and size distribution of the particles are relatively unknown. In the second experiment, measurements are made of the polarization of the laser light as it is scattered through angles of 15 to 150 degrees. It is shown here, that for the conditions under which these data are currently taken, there is little hope of obtaining any information on particle size or size distribution. As a preliminary step to the assessment of the polarization/scattering diagnostic, however, an analysis is made of a three-color laser scattering diagnostic that could lead to successful particle size distribution retrieval. | | | | |
| 20. DISTRIBUTION/AVAILABILITY OF ABSTRACT UNCLASSIFIED/UNLIMITED <input checked="" type="checkbox"/> SAME AS RPT. <input type="checkbox"/> DTIC USERS <input type="checkbox"/> | | | 21. ABSTRACT SECURITY CLASSIFICATION Unclassified | |
| 22a. NAME OF RESPONSIBLE INDIVIDUAL Lt James A. Misener | | | 22b. TELEPHONE NUMBER (Include Area Code) (805) 277-5584 | 22c. OFFICE SYMBOL AFRPL/DYSO |

DD FORM 1473, 83 APR

EDITION OF 1 JAN 73 IS OBSOLETE.

SECURITY CLASSIFICATION OF THIS PAGE

Block 11. the AFRPL Transmissometer and Polarization-Scattering Experiments (U)

CONTENTS

| | | |
|-------|--|-----|
| 1. | INTRODUCTION..... | 7 |
| 1.1 | Background..... | 7 |
| 1.2 | Scope of Present Study..... | 12 |
| 2. | SIZE DISTRIBUTION RETRIEVAL FROM SCATTERING DATA..... | 15 |
| 2.1 | Required Experimental Data..... | 15 |
| 2.2 | Inversion Integral Equation..... | 19 |
| 2.3 | Kernel Functions..... | 21 |
| 2.4 | Inversion Algorithm..... | 24 |
| 2.5 | Test Inversion Conditions..... | 26 |
| 2.6 | Results..... | 29 |
| 2.7 | Modified Inversion Method..... | 39 |
| 2.8 | Final Results..... | 41 |
| 2.9 | Error Analysis..... | 54 |
| 3. | SIZE DISTRIBUTION FROM POLARIZATION/SCATTERING DATA..... | 65 |
| 3.1 | Introduction and Review..... | 65 |
| 3.2 | Linear Inversion on Polarization Components..... | 68 |
| 3.3 | Linearization of Polarization Equation..... | 71 |
| 3.4 | Inversion Algorithm..... | 80 |
| 3.5 | Test Inversions and Results..... | 82 |
| 4. | TRANSMISSOMETER DIAGNOSTIC FOR MEAN RADIUS..... | 89 |
| 4.1 | Introduction..... | 89 |
| 4.2 | Single-Color Diagnostic..... | 90 |
| 4.2.1 | Basic Retrieval Method..... | 90 |
| 4.2.2 | Sensitivity to Size Distribution..... | 94 |
| 4.2.3 | Extension to Bimodal Size Distribution..... | 99 |
| 4.2.4 | Sensitivity to Index of Refraction..... | 107 |
| 4.2.5 | Retrieval and Error Results..... | 113 |
| 4.3 | Two-Color Diagnostic..... | 120 |
| | REFERENCES..... | 127 |

FIGURES

| | |
|---|----|
| 1. Experimental Measurement Geometry..... | 16 |
| 2. Scattering Kernel Functions..... | 22 |
| 3. Twomey Nonlinear Inversion Algorithm..... | 27 |
| 4. Mass Loading Size Distribution..... | 30 |
| 5. Synthetic Scattering Data..... | 32 |
| 6. Size Distribution Retrieval Results..... | 34 |
| 7. Smoothed Size Distribution Retrieval Results..... | 37 |
| 8. Convergence Residual..... | 38 |
| 9. Variation of Retrieval Result with Initial Guess for Uniform Size Distribution..... | 40 |
| 10. Size Distribution Retrieval Results at Fifth Reiteration..... | 42 |
| 11. Size Distribution Retrieval Results for $\lambda = 0.308 \mu\text{m}$ | 45 |
| 12. Size Distribution Retrieval Results for $\lambda = 0.6328 \mu\text{m}$ | 47 |
| 13. Size Distribution Retrieval Results for $\lambda = 1.06 \mu\text{m}$ | 49 |
| 14. Composite of Size Distribution Retrieval Results..... | 51 |
| 15. Final Size Distribution Retrieval..... | 52 |
| 16. Composite of Size Distribution Retrieval Results For 5% Error Superposition..... | 55 |
| 17. Final Size Distribution Retrieval Results for 5% Error Superposition..... | 57 |
| 18. Composite of Size Distribution Retrieval Results for 10% Error Superposition..... | 59 |
| 19. Final Size Distribution Retrieval Results for 10% Error Superposition..... | 60 |
| 20. Comparison of Retrieval Size Distribution with $\pm 10\%$ Bias Error..... | 63 |

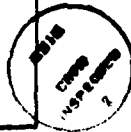
FIGURES (Continued)

| | |
|---|-----|
| 21. Scattering Kernel Functions for $I_1(\theta)$ | 70 |
| 22. Linear Approximation Scattering Kernels..... | 74 |
| 23. Size Distribution Retrieval for Uniform Size Distribution..... | 84 |
| 24. Size Distribution Retrieval for Size Distribution of Fig. 4..... | 85 |
| 25. Extinction Efficiency for Monodispersion at $\bar{a} = a_{32}$ | 93 |
| 26. Retrieval Error Band Caused by Ignorance of Unimodal Size Distribution Function..... | 98 |
| 27. Bimodal Rectangular Size Distribution..... | 100 |
| 28. Mean Scattering Efficiency Results for Bimodal Distribution..... | 104 |
| 29. Variation of Extinction Efficiency with n | 109 |
| 30. Variation of Extinction Efficiency with κ | 110 |
| 31. Retrieval Error Bound Caused by Ignorance of Size Distribution Function and Index of Refraction..... | 111 |
| 32. ρ_{32} Retrieval Result ($\kappa_{\max} = 0.02$)..... | 114 |
| 33. ρ_{32} Error Result ($\kappa_{\max} = 0.02$)..... | 115 |
| 34. ρ_{32} Retrieval Result ($\kappa_{\max} = 0.50$)..... | 116 |
| 35. ρ_{32} Error Result ($\kappa_{\max} = 0.50$)..... | 117 |
| 36. ρ_{32} Error versus ρ_{32} | 119 |
| 37. Error Bounds in Q Ratio..... | 123 |

TABLES

| | |
|---|-----|
| 1. Plume and Particle Size Distribution Parameters..... | 28 |
| 2. Synthetic Polarization Data Using Constant Size Distribution..... | 83 |
| 3. Synthetic Polarization Data Using Size Distribution of Fig. 4..... | 87 |
| 4. Laser Wavelengths..... | 121 |

| | |
|--------------------|-------------------------------------|
| Accession For | |
| NTIS GRA&I | <input checked="" type="checkbox"/> |
| DTIC TAB | <input type="checkbox"/> |
| Unannounced | <input type="checkbox"/> |
| Justification | |
| By | |
| Distribution/ | |
| Availability Codes | |
| Dist | Avail and/or Special |
| A-1 | |



1. INTRODUCTION

1.1 Background

For the past few years, the Air Force Rocket Propulsion Laboratory (AFRPL) has sponsored a series of theoretical and experimental programs on the retrieval of plume flow-field properties by analysis of the infrared radiative and absorptive properties of plumes. This report concludes the participation in these programs by The Aerospace Corporation. The first phase (Ref. 1) was a study of the classic problem of retrieving radial profiles of gas temperature and concentration in cylindrically symmetric, gaseous plumes from transverse emission and absorption (E/A) profiles obtained in a fixed spectral bandpass. The E/A profiles are defined in terms of the radial profiles of pressure, temperature, and concentration (pTc profiles) by integral equations of radiative transfer. Retrieval of the pTc profiles from the E/A profiles involves a numerical inversion of these integral equations.

In this first phase study, an inversion procedure was developed and incorporated into the computer code EMABIC. The inversion algorithm is an iterative Abel inversion. The well-known Abel inversion procedure is valid for optically thin sources; for the general case of optical thickness, an iterative procedure is required. The code has been applied to several synthetic and experimental data and performs satisfactorily as a diagnostic for most gas-only plume problems. Some problems occur when the temperature profile has a deep minimum on the plume axis or when the input E/A profiles are particularly noisy, even if they are adequately smoothed. This is an

-
1. S. J. Young, Inversion of Plume Radiance and Absorptance Data for Temperature and Concentration, AFRPL-TR-78-60, U. S. Air Force Rocket Propulsion Laboratory, Edwards Air Force Base, California, 29 September 1978.

inherent feature of inversion, however, and is not restricted to the method of inversion. A similar inversion code has been developed at the Arnold Engineering Development Center (AEDC) (Ref. 2). A random error propagation routine was added to EMABIC so that retrieval error could be estimated automatically from E/A measurement error (Ref. 3).

The second phase of study was the consideration of multispectral inversion and the effects of particle loading in tactical motor plumes. In multispectral inversion, retrieval is made on the basis of how E/A spectra vary in wavelength for a fixed measurement line of sight. It was found that this inversion scheme is not applicable in the infrared on either a monochromatic or wide-band spectral scale near the exit plane for small plumes with mild temperature gradients, such as those characteristic of tactical rocket motors. Even under ideal circumstances, temperature and concentration retrieval errors up to 30% were encountered. The failure of the method is caused by the lack of spatial resolution inherent in the inversion weighting functions. Results of this study are reported in Ref. 4. Because this method failed for purely gaseous plumes, it was never applied to two-phase plumes. It was decided to revert to the multiposition inversion diagnostic of the first study phase and to pursue its application to two-phase, tactical rocket motor plumes.

2. C. C. Limbaugh, W. T. Bertrand, E. L. Kiech, and T. G. McRae, Nozzle Exit Plane Radiation Diagnostic Measurements of the Improved Transtage Liquid Rocket Injector Program, AEDC-TR-79-29, ARO Inc., Arnold Engineering Development Center, Arnold Air Force Station, Tennessee, March 1980.
3. S. J. Young, Random Error Propagation Analysis in the Plume Diagnostic Code EMABIC, AFRPL-TR-81-59, U. S. Air Force Rocket Propulsion Laboratory, Edwards Air Force Base, California, July 1981.
4. S. J. Young, Multicolor Inversion Diagnostic for Tactical Motor Plumes, AFRPL-TR-80-30, U. S. Air Force Rocket Propulsion Laboratory, Edwards Air Force Base, California, May 1980.

The primary goal of the first part of the third phase was to determine quantitative limits of particle loading in realistic tactical rocket motor plumes for which the gas properties of the plume could be retrieved with standard E/A inversion diagnostic without having to account for the radiating, absorbing, and scattering effects of the particles. The procedure was to assume flow-field properties for two-phase plumes of interest, generate E/A profiles with account of particles using a single-scattering plume radiation code (EAPROF, Ref. 5), retrieve the gas properties from the E/A profiles with the gas-only inversion code EMABIC under the assumption that the profiles were caused by gas alone, and compare the retrieved gas properties with the assumed properties. Generally, the degree of particle loading was treated as a parameter. The work focused on tactical rocket motors where the particle loading level is small, that is, to motors where the particulate material is added to the fuel only as a stabilizer (e.g., Al_2O_3), or to motors where the plume particulate results from chemical reactions (e.g., carbon) but not to motors in which the major fuel is itself a metal. The procedure was applied to a minimum smoke propellant (MSP) model, an advanced liquid propellant (ALP) model, and a reduced smoke propellant (RSP) model. The results are reported in Ref. 6.

Two important results were obtained. The first is that the limit of particle loading at which reasonable (< 10% error) retrieval results can be

-
5. S. J. Young, User's Manual for the Plume Signature Code EAPROF, AFRPL-TR-81-08, U. S. Air Force Rocket Propulsion Laboratory, Edwards Air Force Base, California, January 1981.
 6. S. J. Young, Retrieval of Flow-Field Gas Temperature and Concentration of Low-Visibility Propellant Rocket Exhaust Plumes, AFRPL-TR-82-13, U. S. Air Force Rocket Propulsion Laboratory, Edwards Air Force Base, California, March 1982.

obtained is generally smaller than the nominal loading level for the plume. The important implication of this result is that, to the extent that the systems studied are typical, E/A diagnostics on plumes generated by even low and reduced smoke-type propellants require some account of particle effects. The second result is that the maximum loading level for acceptable gas temperature retrieval is much higher (about an order of magnitude) than that for gas concentration retrieval. Consequently, in applications where temperature retrieval is of primary concern, the use of gas-only E/A diagnostics may be justified even though the total retrieval results may be substantially in error.

Analysis was also made of a procedure in which first-order corrections were made to the total gas-plus-particle E/A profiles by using particle-only E/A profiles obtained outside the gas absorption band. The corrected profiles provided better estimates to the gas-only profiles needed in the gas-only inversion. The particle loading limit for valid use of this procedure is the value for which the total extinction of radiation by particles over a full diameter of the plume is about 10%. (Note that if this condition is met, then the condition is also met that the attenuation by scattering alone over this path is less than about 10%. The latter condition is required by the single-scattering assumption used in the work.) For the two cases (MSP and RSP) where the nominal loading limit roughly satisfied this condition, the use of the procedure resulted in retrieved gas properties that were accurate to within the convergence criteria set on the inversion. For the ALP model, the nominal loading level was well above this limit, and the retrieved results were poor.

In the second part of the third phase (Refs. 7 and 8), the work begun in Ref. 6 was expanded in two significant aspects. First, the restriction of the first-order, off-band (FOOB) correction procedure that the plume be optically thin to total extinction was relaxed. This was accomplished essentially by using the full, two-phase, single-scattering radiation model in the inversion code EMABIC, as well as in the plume radiation code EAPROF. The second significant expansion was that retrieval diagnostics for particle properties were developed. The previous work on two-phase plume diagnostic assumed that all particle properties (e.g., species, index of refraction, spatial and size distribution) were known. The new work defined procedures for retrieving the volume cross sections for particle absorption, scattering, and extinction, as well as the particle scattering phase function and radial temperature profile.

As in the preceding work of this phase, the analyses presented were made with synthesized E/A/S data, that is, data computed from assumed known plume properties. No application to experimental data was made. Also, since the main emphasis of this work was on the feasibility of retrieval and not its practical application, no treatment of random or bias error propagation was made. Application of the inversion procedure was made to the MSP, ALP, and RSP models described in Ref. 5. Results and discussion of the application are reported in Refs. 7 and 8.

-
7. S. J. Young, Retrieval of Flow-Field Temperature and Concentration of Low-Visibility Propellant Rocket Exhaust Plumes, AFRPL-TR-82-038, U.S. Air Force Rocket Propulsion Laboratory, Edwards Air Force Base, California, January 1983.
 8. S. J. Young, User's Manual for the Flow-Field Diagnostic Code EMABIC, AFRPL-TR-82-037, U.S. Air Force Rocket Propulsion Laboratory, Edwards Air Force Base, California, February 1983.

1.2 Scope of Present Study

In the course of this third-phase work, it was suggested that further study be made on the retrieval of particle size distribution and concentration from the volume scattering cross section, volume absorption cross section, and scattering phase function obtained with these diagnostics. Subsequent analysis has shown that this approach is not likely to succeed. The major problem is that the retrieved cross sections and phase function are obtained at only one wavelength (the off-band wavelength mentioned above) and, in addition, at a wavelength that is inappropriate for particle size retrieval. Typically, the off-band wavelength will be greater than about 3 μm ; but, the appropriate wavelength for retrieval of size distributions is about the same as the mean particle size, and this is typically less than 1 μm .

Recognizing this limitation, a new procedure for obtaining size distributions was formulated. As in the previous diagnostic schemes, scattering data are obtained with a traversing laser apparatus. Actually, data are obtained at three laser wavelengths that center on and bound the expected size distribution. An Abel inversion is made of these data and these inversion results used in an iterative inversion scheme (Twomey, nonlinear) to retrieve the size distribution. In its most general form, the radial profile of the size distribution and particle loading can be retrieved. A detailed discussion of the method and an example of its application to the simplified case where the laser apparatus is not scanned (and thus Abel inversion is not required) comprise the work described in Section 2 of the present report. The retrieved size distribution in this example reflects some average size distribution over the plume axial station. An error propagation analysis for the example is also presented.

In addition to providing a candidate particle size diagnostic for future application to small rocket motor plumes, the work of Section 2 provides the foundation for analysing the data which have actually been taken at AFRPL in the Scattering-Angle/Polarization experiment. These data consist of measurements of the polarization of laser radiation which has been scattered by plume particulates. The analysis is presented in Section 3 and suggests that the experimental conditions under which the data are currently taken is inappropriate and that no useful information on particle size or distribution can be obtained.

In Section 4, an analysis is made of another on-going AFRPL measurement diagnostic--the single-color transmissometer experiment. In these measurements, simple transmission measurements of laser radiation through a diameter of the plume are made. With auxiliary measurements made on the total mass loading of the plume, these transmission results can be used to infer a "characteristic" mean particle size that is relatively insensitive to knowledge of either the particle size distribution or index of refraction. The results of this analysis are quite encouraging and indicate that the mean particle size may be retrieved with errors of < 10 to 20% under good experimental conditions.

2. SIZE DISTRIBUTION RETRIEVAL FROM SCATTERING DATA

In this section, a three-color, laser scattering diagnostic is developed for the retrieval of particle size distributions in low-visibility propellant, solid rocket motor plumes. An iteration algorithm based on Twomey's nonlinear iteration method is employed. An example application for Al_2O_3 is given for synthetic data at $\lambda = 0.308, 0.6328, \text{ and } 1.06 \mu\text{m}$ and seven scattering angles between $\theta = 5$ and 20 deg .

In Section 2.1, the experimental geometry and required experimental results are discussed. The integral equations relating this result to the desired particle size distribution is derived in Section 2.2, and some important aspects of the equations are discussed in Section 2.3. The inversion algorithm that affects the retrieval is presented in Section 2.4. Hypothetical test conditions and retrieval results are reported in Sections 2.5 and 2.6, respectively. A modification to the method that results in better retrieval results is discussed in Section 2.7, and results of the improved method are presented in Section 2.8. Finally, an estimate of the effects of experimental error on the quality of inversion is given in Section 2.9.

2.1 Required Experimental Data

The geometry of the scattering problem is shown in Fig. 1. Light from a laser at wavelength λ enters the plume perpendicular to the plume axis along the optical path s located a transverse distance z from the plume diameter. The intensity of light scattered through an angle θ into a sensor a distance D away with entrance aperture A is

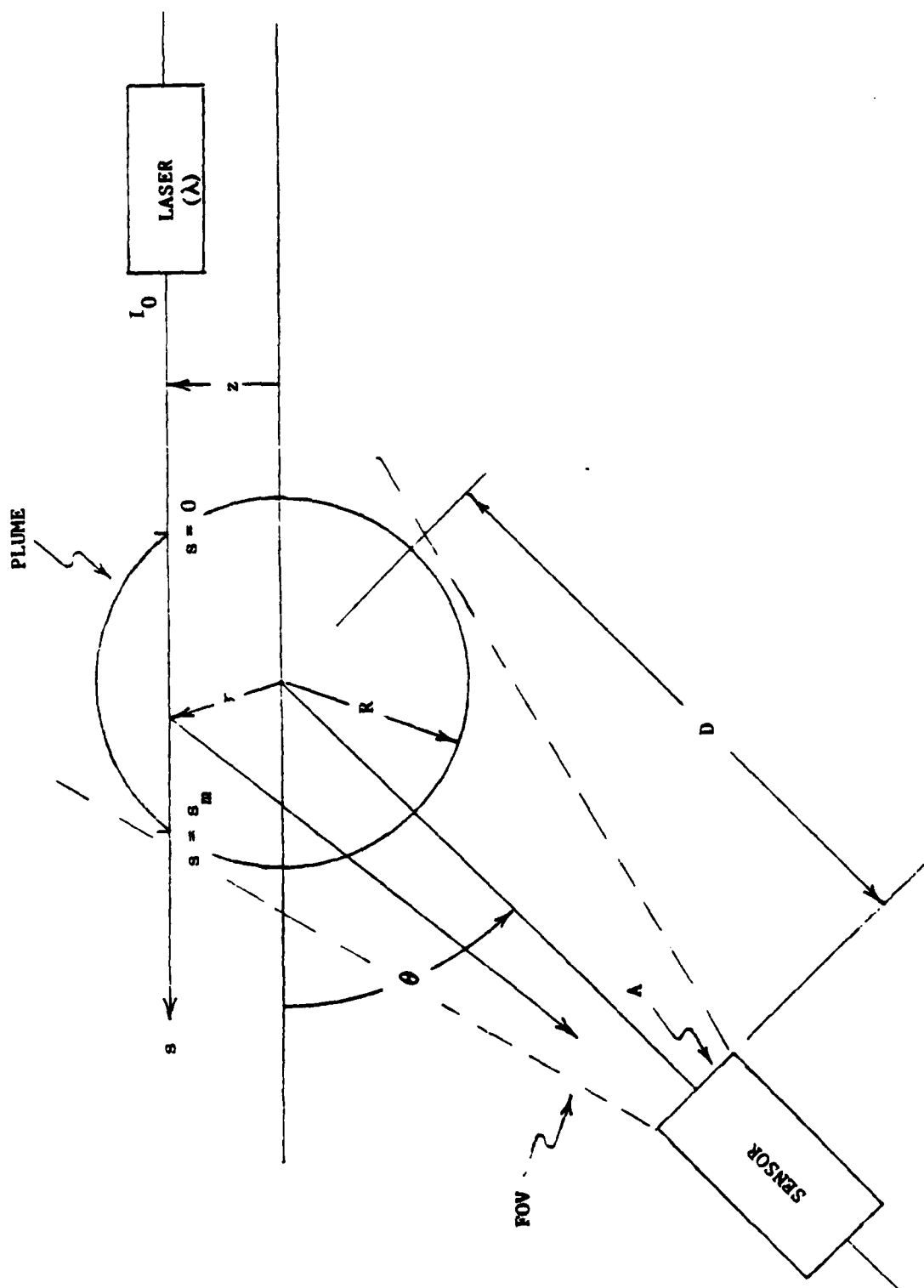


Fig. 1. Experimental Measurement Geometry

$$I(\theta) = I_0 \left(\frac{A}{D^2} \right) \int_0^{s_m} N(s) \frac{d\sigma_s(s, \theta)}{d\Omega} ds \quad (1)$$

where I_0 is the incident laser power, $N(s)$ is the particle number density at s , and $d\sigma/d\Omega$ is the differential scattering cross section at s . The integration over s indicates that all light along the chord s scattered at angle θ contributes to the signal. Thus, the field of view of the sensor should be wide enough to view the entire plume diameter. The validity of Eq. (1) also requires that $D \gg R$ where R is the plume radius, and that absorption and multiple scattering within the plume may be neglected.

Define

$$F(\theta) = \frac{I(\theta)}{I_0} \left(\frac{D^2}{A} \right) \quad (2)$$

$$g(\theta, s) = N(s) \frac{d\sigma_s(s, \theta)}{d\Omega} \quad (3)$$

so that Eq. (1) may be written as

$$F(\theta) = \int_0^{s_m} g(\theta, s) ds. \quad (4)$$

Transformation to cylindrical coordinates (Ref. 1) with the assumption that N and $d\sigma_s/d\Omega$ (and thus g) are functions of radial coordinate r only, and inserting the dependence on z yields the Abel integral equation

$$F(\theta, z) = 2 \int_z^R g(\theta, r) \frac{r dr}{(r^2 - z^2)^{1/2}}. \quad (5)$$

If the function $F(\theta, z)$ is measured for all z in $0 < z < R$, then a standard Abel inversion (Ref. 1) of this equation can be made to obtain the radial function

$$g(\theta, r) = N(r) \frac{d\sigma_s(r, \theta)}{d\Omega} . \quad (6)$$

This scattering function result is the primary input for retrieving the size distribution.

If absorption does occur in the plume, by either gas or particle species, the function $g(\theta, r)$ can still be retrieved by making an auxiliary attenuation scan at $\theta = 0$ and employing an iterative Abel inversion (Ref. 7). Single-scattering, however, must still be obtained.

A significant simplification occurs for the retrieval of $g(\theta, r)$ if there is reason to believe that the particle loading size distribution and differential scattering cross section are constant in radius (or, if not, if one is only interested in retrieving the "average" properties of the plume). In this case, $g(\theta, r)$ is not (or assumed not) a function of r and Eq. (5) can be immediately integrated and the result solved for $g(\theta)$ to obtain

$$g(\theta) = \frac{F(\theta, z)}{2 (R^2 - z^2)^{1/2}} . \quad (7)$$

$F(\theta, z)$ need only be measured at one value of z (say $z = 0$) to obtain

$$g(\theta) = \frac{F(\theta)}{2R} . \quad (8)$$

2.2 Inversion Integral Equation

From the function $g(r, \theta)$, one can obtain the size distribution of particles within the plume at each r . In this section, the integral equation defining $g(r, \theta)$ in terms of the size distribution is derived. Let $n(a, r)$ be the particle number density size distribution at r , and a the particle radius. The total number density at r is

$$N(r) = \int_0^{\infty} n(a, r) da. \quad (9)$$

The function $g(r, \theta)$ is

$$g(r, \theta) = N(r) \frac{d\sigma_g(r, \theta)}{d\Omega} = \int_0^{\infty} \pi a^2 Q(\theta, a, r) n(a, r) da \quad (10)$$

where $Q(\theta, a, r)$ is the Mie differential scattering efficiency that obtains for scattering angle θ , particle radius a , and the index of refraction for the plume conditions at r . Since r is only a parameter in Eq. (10), we can unencumber the notation by dropping r and remembering that the following analysis must be repeated for each r of interest.

The following development is made in terms of the mass loading size distribution $m(a)$ rather than $n(a)$ directly. The relationship between the two is

$$m(a) = d \frac{4}{3} \pi a^3 n(a) \quad (11)$$

where d is the bulk material density of the particulate species. In terms of this function, we have from Eq. (10)

$$g(\theta) = \int_0^{\infty} \frac{3}{4d} \frac{Q(\theta, a)}{a} m(a) da. \quad (12)$$

In place of the variable a , we use the dimensionless size parameter

$$x = \frac{2\pi a}{\lambda}. \quad (13)$$

Then

$$g(\theta) = \int_0^{\infty} \frac{3\pi}{2d\lambda} \frac{Q(\theta, x)}{x} m(x) dx \quad (14)$$

where $m(x)$ is the size distribution in x and is related to $m(a)$ by

$$m(a) = \frac{2\pi}{\lambda} m(x). \quad (15)$$

Equation (14) is the final relationship between the function $g(\theta)$ and the size distribution function $m(x)$. It may be rewritten in the standard inversion form (Ref. 9) as

$$g(\theta) = \int_0^{\infty} K(\theta, x) m(x) dx \quad (15a)$$

$$K(\theta, x) = \frac{3\pi}{2d\lambda} K_0(\theta, x) \quad (16b)$$

-
9. S. Twomey, Introduction to the Mathematics of Inversion in Remote Sensing and Indirect Measurements, Elsevier, New York, 1977.

$$K_0(\theta, x) = \frac{Q(\theta, x)}{x} \quad (16c)$$

where $K(\theta, x)$ is the so-called kernel function. This function is essentially a weighting function that determines the relative contribution that particles with radius $a = \lambda x/2\pi$ make to the function $g(\theta)$.

2.3 Kernel Functions

Equation (16) relates the measured function $g(\theta)$ to the desired function $m(x)$ through an integration with the kernel function $K(\theta, x)$. The ability to perform an inversion of Eq. (16), and the accuracy with which it can be accomplished lies largely in the functional form of the kernel (Ref. 9).

Examples of kernels used in the present analysis are shown in Fig. 2. The function $K_0(\theta, x) = Q(\theta, x)/x$ was evaluated for the seven angles $\theta = 5.0, 7.5, 10.0, 12.5, 15.0, 17.5$, and 20 deg at the 2520 values of $x = 0.1, 0.2, \dots, 252.0$. The curves of Fig. 2 have been degraded from this resolution to the constant logarithm increment shown on the figure. The calculations were made with an index of refraction $n = 1.75 - 0.0i$, which approximates the index for pure Al_2O_3 from the near UV to the near IR (Ref. 10). $Q(\theta, x)$ was computed with standard Mie scattering algorithms (Ref. 11).

The 0.1 resolution on the x -grid was chosen so that simple trapezoidal integration using these grid points would yield integration results to better

-
10. C. B. Ludwig et al., Standardized Infrared Radiation Model (SIRRM), AFRPL-TR-81-54, U. S. Air Force Rocket Propulsion Laboratory, Edwards Air Force Base, California, August 1981; American Institute of Physics Handbook, McGraw Hill, New York, 1957.
 11. D. Diermendjian, Electromagnetic Scattering on Spherical Polydispersions, Elsevier, New York, 1969.

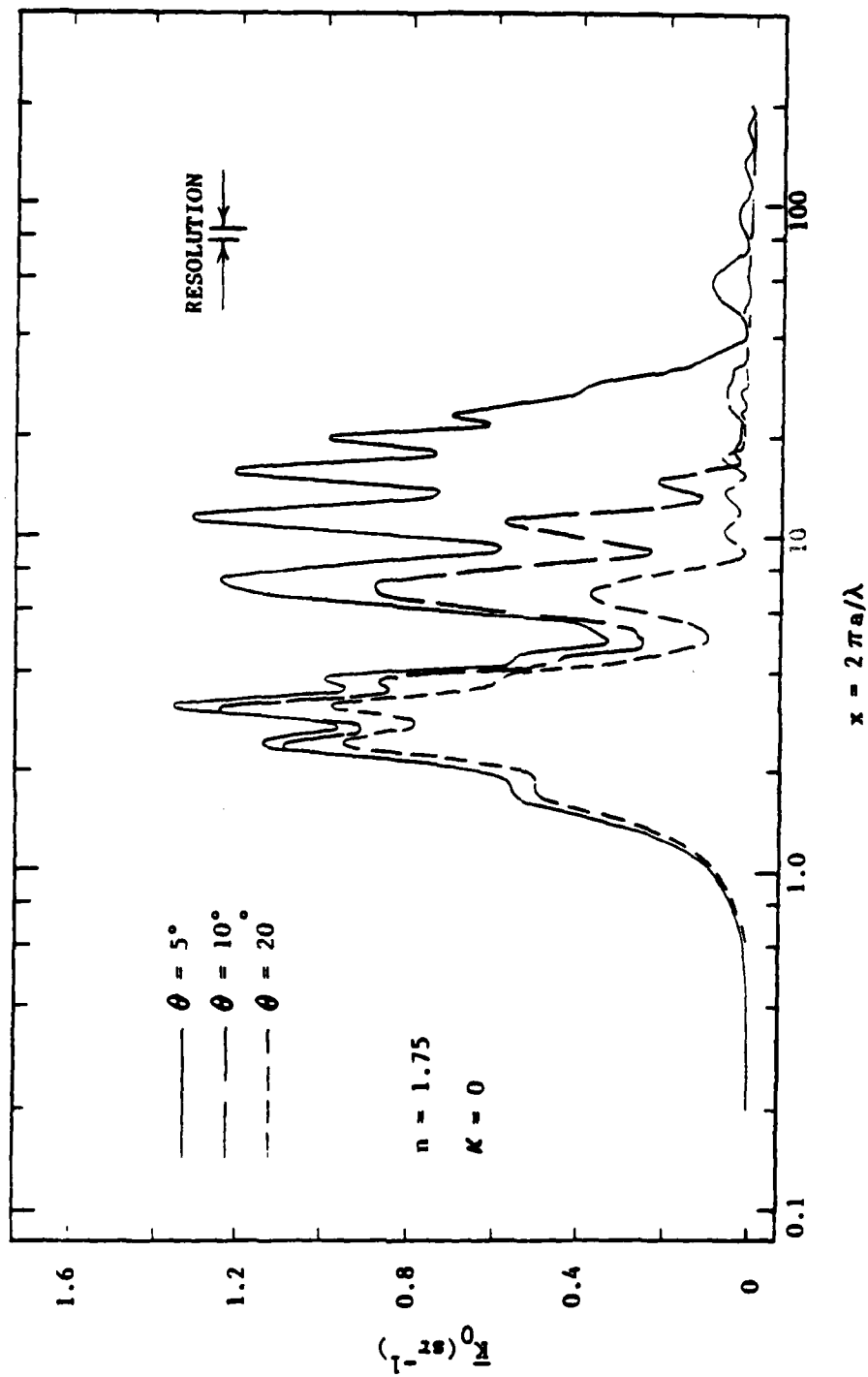


Fig. 2. Scattering Kernel Functions

than $\sim 1\%$. The angle grid was chosen to represent a possible experimental array in which (1) the spacing between angles is large enough to accommodate individual sensors at each angle, (2) the smallest angle is far enough away from $\theta = 0$ that no directly propagated laser radiation is seen, (3) the scattering is largely forward scattering so that the largest signals may be obtained, and (4) the total range of θ is small enough that the expected signal does not range over more than about an order of magnitude.

Three features of the kernels shown in Fig. 2 warrant discussion with respect to inversion. First, the kernels limit the range of x over which an inversion can be made. The kernel at $\theta = 5$ deg is the widest and is sensibly different from zero only between $x \approx 0.8$ and ≈ 100 while the half width extends only from $x = 2.0$ to $x \approx 24$. Outside this region, the kernel is essentially zero and no contribution is made to $g(\theta)$ from $m(x)$ regardless of what $m(x)$ is [assuming it is a realistic $m(x)$]. Conversely, no information about $m(x)$ can be obtained outside the region. As a conservative estimate, using the half width, retrieval can be made over only about an order of magnitude in size from $x \approx 2$ to $x \approx 20$. If it is expected that a size distribution is wider than an order of magnitude, then this kernel "window" must be moved across the distribution by varying the wavelength. The x -window remains fixed, but the a -window varies directly with λ . For example, at $\lambda = 0.4 \mu\text{m}$ the a -window is $a \approx 0.13$ to $13 \mu\text{m}$ and at $\lambda = 0.8 \mu\text{m}$ it is $a \approx 0.25$ to $25 \mu\text{m}$.

The second important feature of the kernels is that their width varies with θ . As the angle increases, the width decreases whereas the peak height at $x \approx 2.5$ remains reasonably constant. Thus, with changing θ , the kernel acts as a variable-width bandpass filter with the lower cut-off fixed. It is, in fact, this feature that makes an inversion possible at all. If the kernels

did not change with θ , then measurements at all angles would give the same result for $g(\theta)$ and the problem would be degenerate.

The third feature worth noting is the highly fluctuating structure of the kernels even in the degraded plots of Fig. 2. The consequence of these fluctuations will be discussed later.

2.4 Inversion Algorithm

The preceding formulation and discussion on kernel functions is relevant to any method of inverting Eq. (16) for the unknown function $m(x)$, and several methods are discussed in Ref. 9. The two approaches that appear most applicable to the present problem are constrained linear inversion (the Phillips-Twomey method) and nonlinear iteration. In this report, Twomey's method of nonlinear iteration is employed. This method, or minor variations of it, has been used by Twomey in retrieving particle size distributions from screening measurements (Refs. 9 and 12) and by Hansen (Ref. 13) in obtaining atmospheric aerosol distributions from optical scattering measurements.

The nonlinear algorithm as used here is shown as a computational flowchart in Fig. 3. One begins with the known function measurements $g_i = g(\theta_i)$ on the angle grid θ_i ($i = 1, 2, \dots, N$), the known kernel functions $K_i(x) = K(\theta_i, x)$, the maxima (over x) of the kernel functions K_i^{\max} , and a first guess solution $m(x)$. A loop is then made over all of the measurements. First the value g'_i is calculated that would result if the first guess solution were the true solution. This value is then used in conjunction with the observed g_i to

12. S. Twomey, J. Comp. Physics 18, 188 (1975).

13. M. Z. Hansen, Applied Optics 19, 3441 (1980).

compute a correction parameter ξ . Note that if the guess is indeed the true solution, then $\xi \equiv 0$. The correction parameter is then used with the normalized kernel K/K^{\max} to modify the first guess solution. If $\xi = 0$, no modification occurs. The loop is continued over all of the angles θ_i . The end result is one cycle of the iteration process. A second cycle is then made with the final $m(x)$ obtained in the first cycle as the first guess for the second cycle. The process is continued until some convergence criterion is met.

Some of the modifications of the method that have been used by Twomey and Hansen, and in some of the preliminary work here include (1) restrictions on the range of ξ , (2) variation in the functional form of kernel correction, and (3) timing of correction. Twomey suggests (Ref. 9) that it might be advisable to restrict the range of ξ in order to slow down the rate of convergence (although he gave no explicit reason why). The unrestricted range is $-1 < \xi < \infty$. Preliminary work indicated that restriction was not really necessary and that no detrimental effects developed with use of the whole range. Nevertheless, a restriction to the range $-0.99 < \xi < 100$ was imposed in the interest of prudence. Hansen (Ref. 13) achieved a similar kind of convergence damping by modifying the functional form of kernel correction. Rather than the form $1 + \xi K_1/K_1^{\max}$, he used $1 + s|\xi K_1/K_1^{\max}|^R$ where s is +1 or -1 depending on whether ξ is + or - and R is an exponent less than or equal to one. His work did show significant changes in convergence behavior with R . $R = 0.7$ provided the stablest convergence. The third modification, that is, the timing of corrections has the biggest effect on the present work. In Twomey's original method of application, the individual corrections were not applied immediately. The calculation of g'_1 in the first step of the loop in

Fig. 3 was always made with the first guess solution, not the solution obtained by modification in previous loops. The effect of this variation of the method in the present work was devastating. No convergence at all could be achieved. This result is in direct conflict with Twomey's statement (Ref. 9) that there is not much difference between the two methods.

The significant advantages of this nonlinear iteration algorithm are that it is straightforward to implement, stable, transparent as to how it works, and mostly, that it always yields a positive solution so long as the initial guess solution is positive. Other inversion methods, including the popular method of constrained linear inversion can give unrealistic negative values for $m(x)$. Also, this method is purported to be better able than others to handle retrieval of functions with large dynamic range. The one serious flaw of the method will be pointed out later along with a method for reducing its effect.

2.5 Test Inversion Conditions

In order to test the inversion algorithm, a model test case was established using Al_2O_3 as the particulate species. The particle size and distribution parameters used were based largely on results obtained from actual measurements of small tactical motors (Ref. 14) and are listed in Table 1.

The loading and size distribution of particules within the plume were assumed to be uniform in radius. The size distribution function used was

-
14. T. D. McCay et al., Laser Mie Scattering Measurements of Particulate Size in Solid Rocket Motor Exhaust, JANNAF 12th Plume Technology Meeting, November 1980.

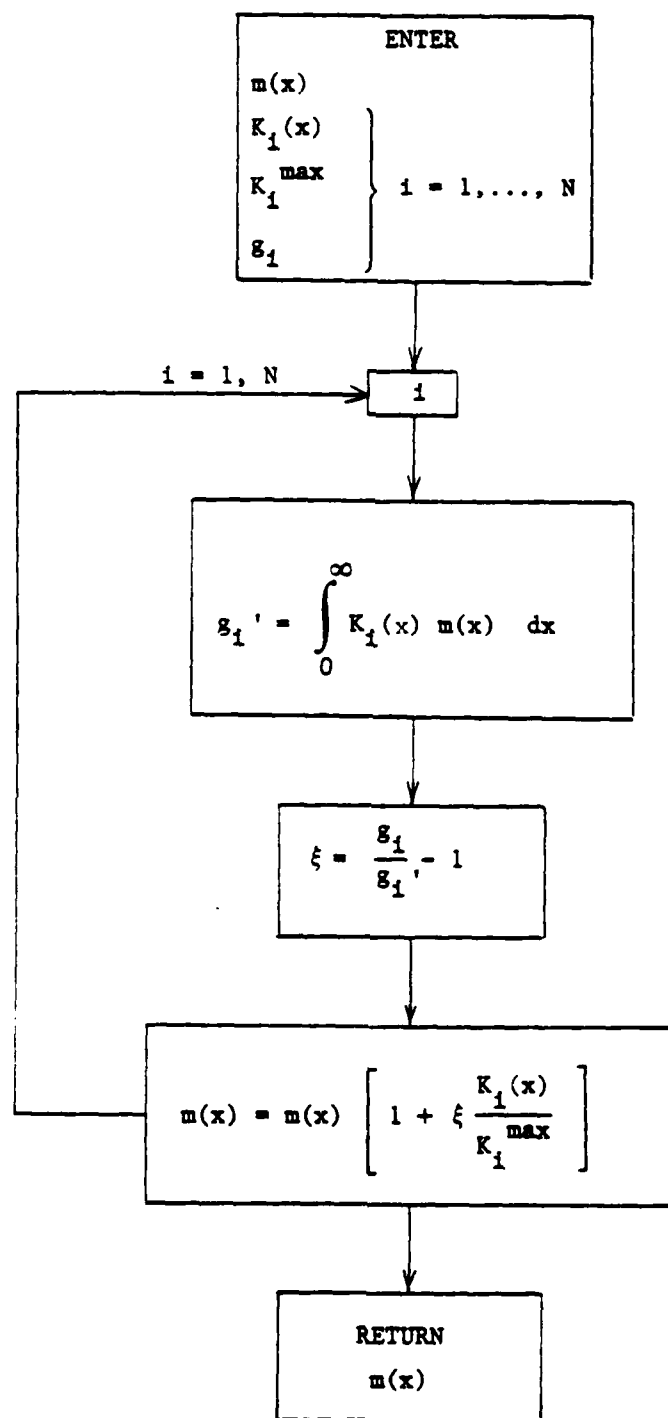


Fig. 3. Twomey Nonlinear Inversion Algorithm

Table 1. Plume and Particle Size Distribution Parameters.

| | | | |
|--------------------------|------------|---|-------------------------------------|
| Plume Radius | R | = | 5 cm |
| Typical Particle Size | a | = | 0.5 μm |
| Mass Loading | M | = | $1.0 \times 10^{-6} \text{ g/cm}^3$ |
| Bulk Density | ρ | = | 3.7 g/cm^3 |
| Particle Loading | N | = | $1.16 \times 10^5/\text{cm}^3$ |
| Wavelength | λ | = | 0.6328 μm (HeNe) |
| Index of Refraction | n | = | 1.75 - 0.01 |
| Extinction Cross Section | σ_e | = | $4.4 \times 10^{-8} \text{ cm}^2$ |

Size Distribution Parameters

| | | |
|----------|---|---|
| α | = | 3 |
| β | = | 1 |
| γ | = | $6 \mu\text{m}^{-1}$ |
| a_{32} | = | 1.0 μm |
| a_c | = | 0.5 μm (number density distribution) |
| | | 1.0 μm (mass loading distribution) |
| A | = | 388.8 M μm |

$$M(a) = A a^{\alpha+3} e^{-\beta a^\gamma} \quad (17)$$

which corresponds to the large-size peak of the bimodal distribution used in previous work (Ref. 6). The parameters of the distribution are given in Table 1. Linear and logarithmic plots of the distribution are shown in Figs. 4a and 4b, respectively. (The normalization of this function is $\int_0^\infty m(a) da = M$; the normalization constant is $A = \gamma \beta^{(\alpha+4)/\gamma} \Gamma[(\alpha+4)/\gamma]$ where Γ is the gamma function; and the relationship between mass loading and particle number density is $M = \frac{4}{3} \pi N \frac{\rho}{\beta^{3/\gamma}} \Gamma(\frac{\alpha+4}{\gamma}) / \Gamma(\frac{\alpha+1}{\gamma})$.)

The mass loading was taken as $M = 1.0 \times 10^{-6} \text{ g/cm}^3$, which corresponds to a particle number density of $N = 1.16 \times 10^5/\text{cm}^3$. At $\lambda = 0.6328 \text{ } \mu\text{m}$ (HeNe laser), the extinction cross section for the size distribution is $\sigma_e \approx 4.4 \times 10^{-8} \text{ cm}^2$. The extinction over a full diameter ($2R = 10 \text{ cm}$) of the plume is then $1 - e^{-2RN\sigma} \approx 0.05$, which indicates that the test case easily satisfies the conditions of single-scattering and negligible absorption.

2.6 Results

With the test conditions discussed in Section 2.5, simulated experimental results for $g(\theta)$ were calculated with Eq. (12). The result is shown in Fig. 5 ($\lambda = 0.6328 \text{ } \mu\text{m}$). The values at the $NA = 7$ angles $\theta = 5.0, 7.5, 10.0, \dots, 20.0$ were then used as input to the nonlinear inversion algorithm. Retrieval was made in the range $a = 0.06$ to $6.0 \text{ } \mu\text{m}$ with $MD = 50$ equal divisions of $\text{Log}(a)$. A constant initial guess of $m(a) = 0.25 \times 10^{-6} \text{ g/cm}^3$ across the retrieval range was used. Convergence was deemed complete when the root-mean-square (rms) difference

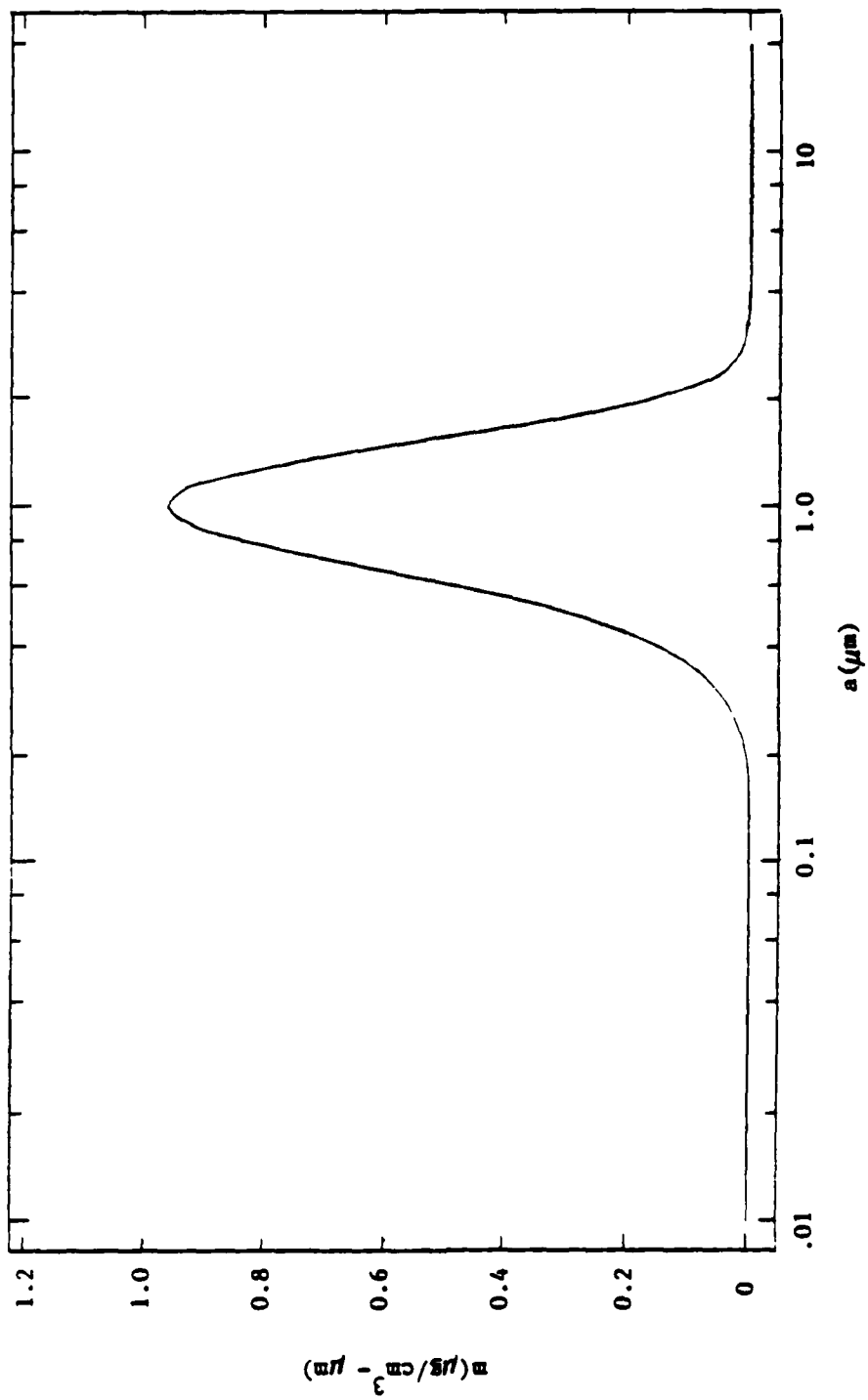


Fig. 4a. Mass Loading Size Distribution (Linear Plot)

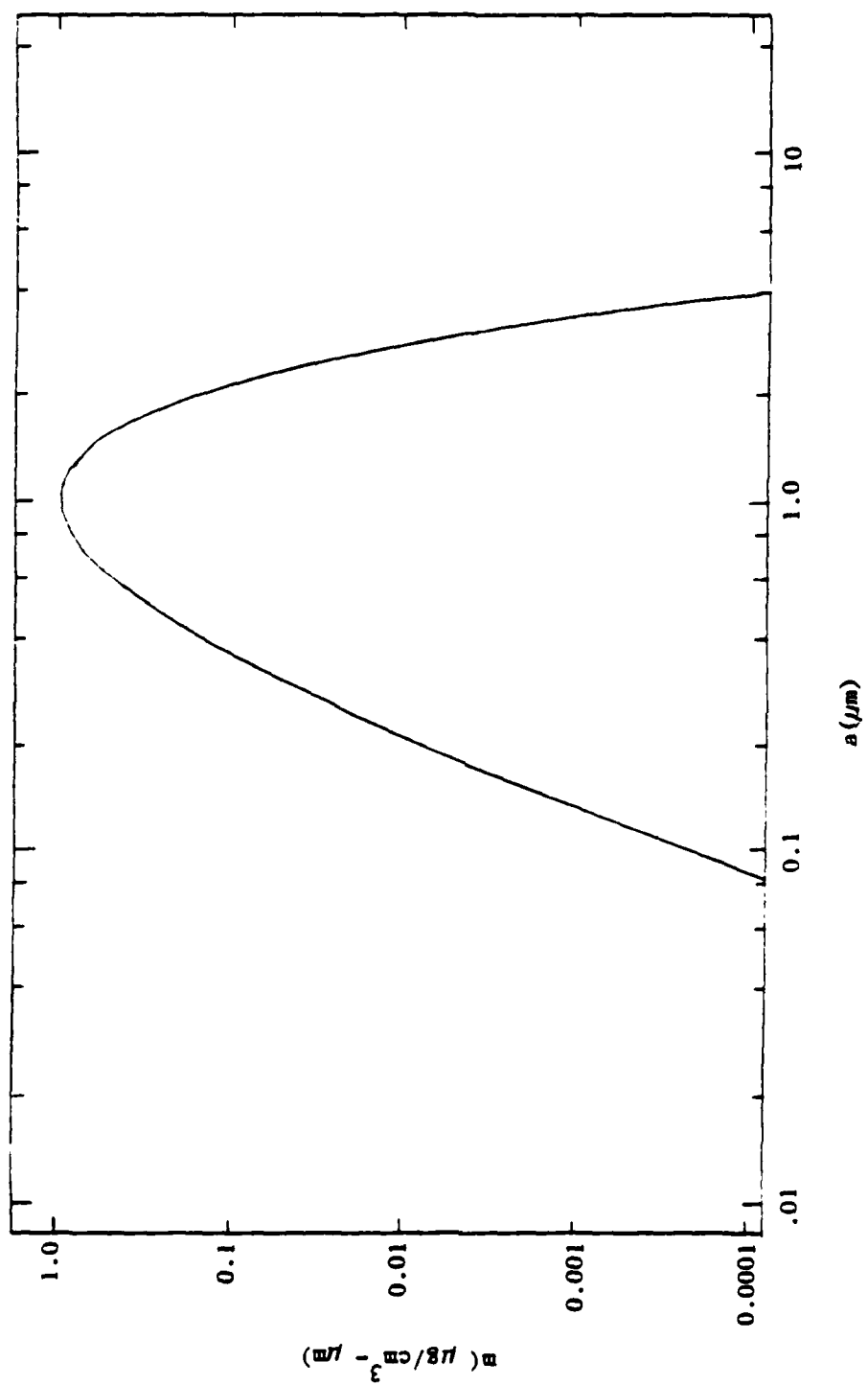


Fig. 4b. Mass Loading Size Distribution (Log Plot)

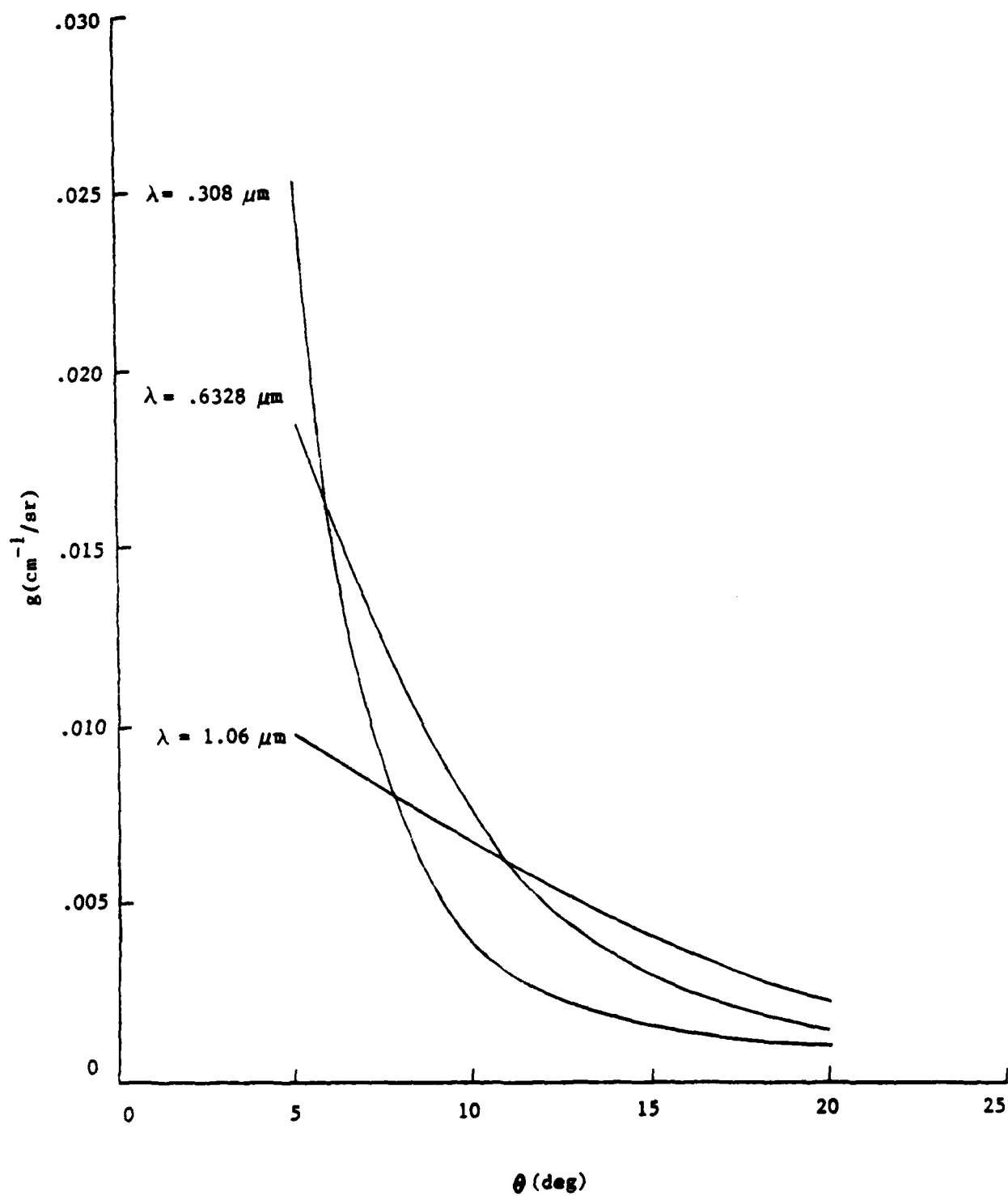


Fig. 5. Synthetic Scattering Data

$$\Delta f = \sqrt{\frac{1}{MD} \sum_{j=1}^{MD} \left(\frac{m'(j) - m(j)}{m(j)} \right)^2} \quad (18)$$

between two successive iterations (primed and unprimed) was less than or equal to 1%. This was achieved at the 22nd iteration. The retrieved mass distribution is shown in Figs. 6a and 6b.

The results elicit both optimism and pessimism. On the optimistic side, the general features of the retrieval are as expected. In the window region from $a \approx 0.3$ to $\approx 2.0 \mu\text{m}$, the retrieved distribution is of the order of magnitude of the true distribution, whereas well outside the region ($a < 0.1$ and $a > 3.0 \mu\text{m}$), the initial guess distribution has not been severely disturbed. Also, the retrieval window corresponds very closely to the window predicted in Section 2.3 on the basis of the functional form of the kernel. The discouraging result is the degree of fluctuation of the retrieved result in the window. These fluctuations result from the strong influence of the kernel functions on the solution. Twomey has shown (Refs. 9 and 12), in fact, that the nonlinear inversion algorithm essentially forms a solution using the kernel functions as a basis set. That is, the solution generated is of the form

$$m(x) = \sum_{i=1}^{NA} C_i K_i(x). \quad (19)$$

On the other hand, the kernel functions in no way approximate a complete basis set, and thus it is not possible to approximate the solution accurately in this way.

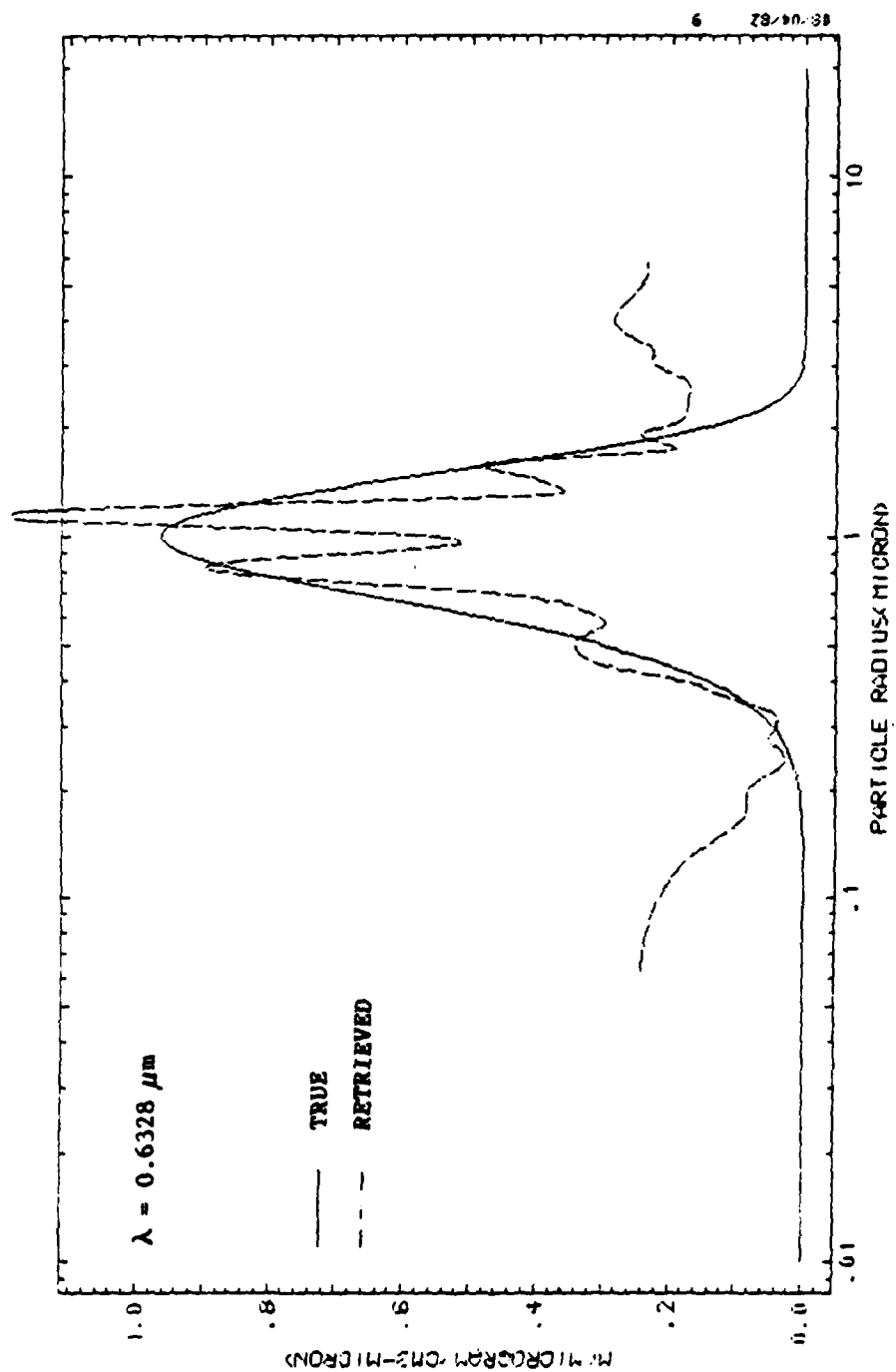


Fig. 6a. Size Distribution Retrieval Results (Linear Plot)

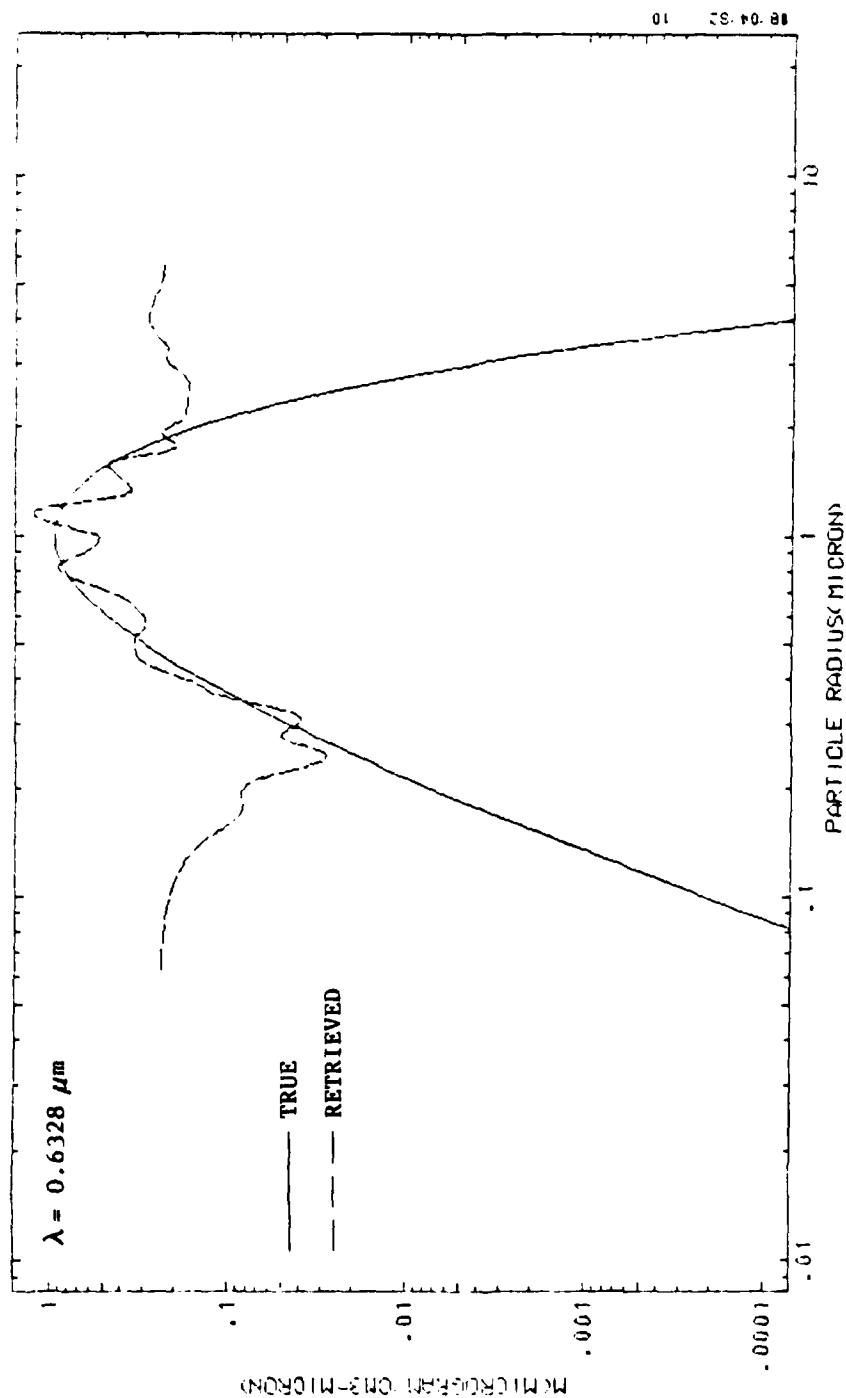


Fig. 6b. Size Distribution Retrieval Results (Log Plot)

Attempts were made to suppress the fluctuation by implicit (using smaller values of MD) and explicit smoothing. In no case was significant improvement achieved. When smaller values of MD were used, the frequency of fluctuations was reduced, but the magnitude of fluctuations was not. In Fig. 7 an example of explicit smoothing of the form

$$\bar{m}(j) = \frac{1}{2MS + 1} \sum_{k=j-MS}^{j+MS} m(k) \quad (20)$$

with $MS = 3$ is shown. Again, the frequency of fluctuations is reduced but the overall agreement between the retrieved and true distributions is not good. A method which does successfully eliminate the strong influence of the kernels is presented in the next section.

The convergence stability result for the inversion is shown in Fig. 8. The residual rms difference between the reconstructed (primed) and input (unprimed) profiles

$$\Delta g = \sqrt{\frac{1}{NA} \sum_{i=1}^{NA} \left(\frac{g'(i) - g(i)}{g(i)} \right)^2} \quad (21)$$

is plotted versus iteration. At convergence ($\Delta f < 0.01$), the residual is $\Delta g \approx 2\%$. This value is consistent with Twomey's observation (Refs. 9 and 12) that even for error free data, the accuracy of the retrieved solution is seldom better than about 1%.

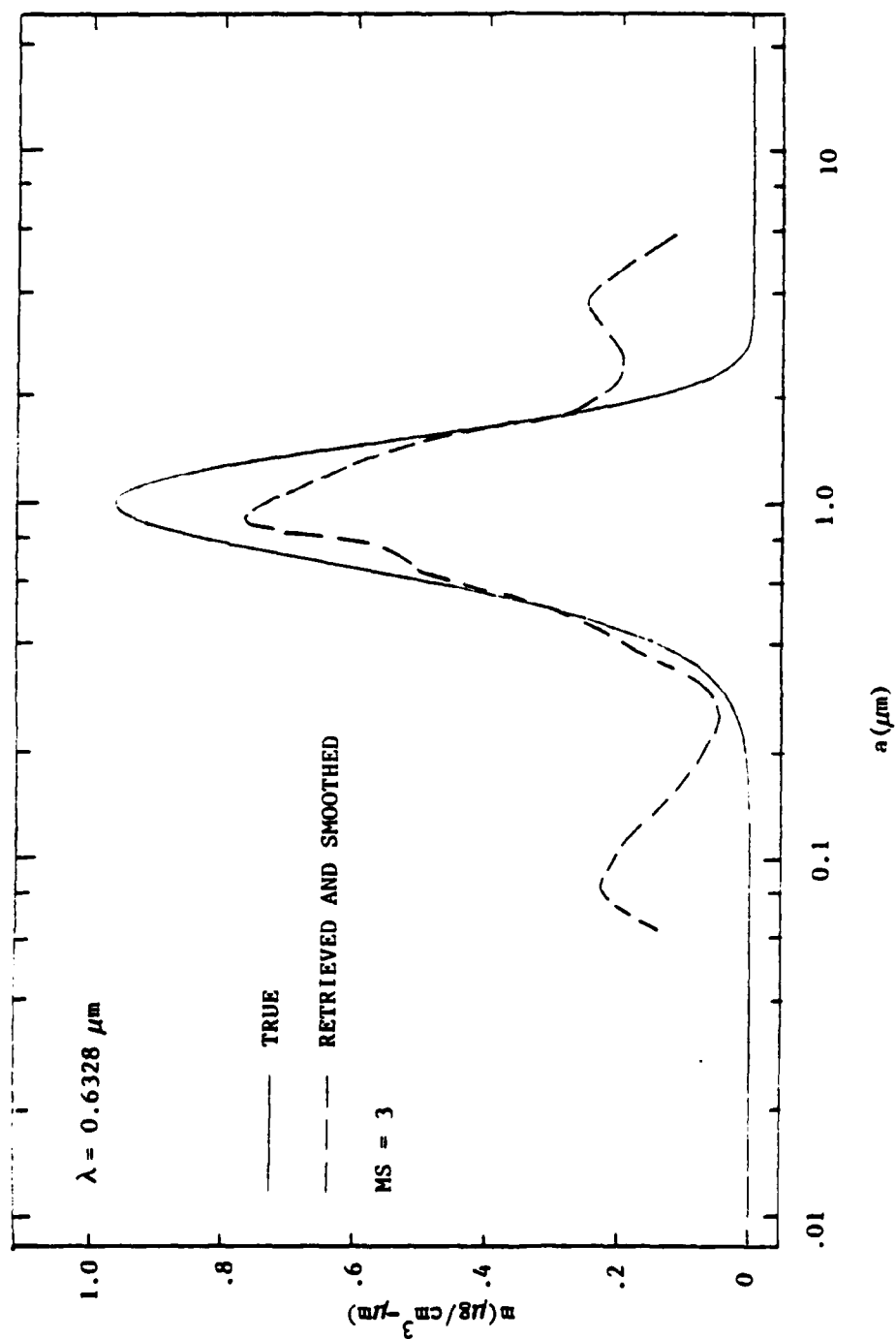


Fig. 7. Smoothed Size Distribution Retrieval Result

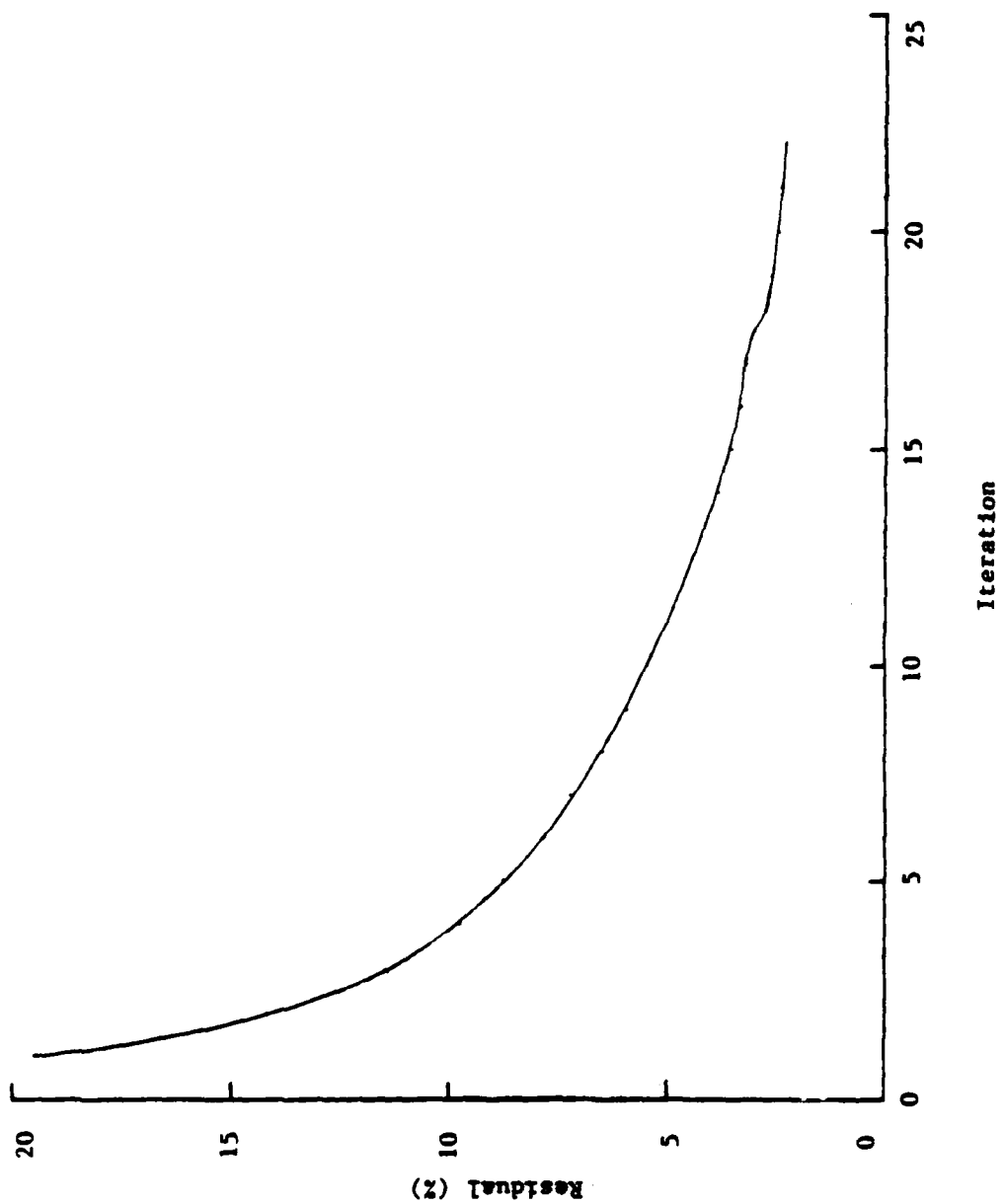


Fig. 8. Convergence Residual

2.7 Modified Inversion Method

The key to improving the accuracy of retrieval is to use an initial, first-guess solution that is closer to the true solution. According to Twomey (Refs. 9 and 12) and Hansen (Ref. 13), the choice of initial guess does not have much influence on retrieval results. Some preliminary work here supports the opposite conclusion. A test case was run with the flat size distribution $m(a) = 1.0 \times 10^{-6} \text{ g/cm}^3$. Synthetic data were generated and inversion runs were made with constant initial guess solutions of $m(a) = 1.0 \times 10^{-6}$, 0.5×10^{-6} , and $0.1 \times 10^{-6} \text{ g/cm}^3$. The retrieved results are shown in Fig. 9. When the initial guess was in fact the true solution, the true solution was retrieved. As the initial guess was reduced in value, the retrieved solution became progressively worse with respect to the magnitude of fluctuations. These results support the conclusion that the better the initial guess, the better the solution.

In synthetic analyses such as performed here, one knows how to construct a "better" first guess solution because one knows the identify of the true solution. In application to experimental results, one may also have some idea from auxiliary observations as to what the distribution is and one should certainly take full advantage of the information. On the other hand, from a purely objective point of view, the solution is completely unknown and the use of some constant initial guess (as is done here) is probably all that is justified. The question then is, how does one construct a better first guess. The answer is, do an inversion using a constant first guess and use the result as the first guess to another inversion. After all, this result obtained in Fig. 6 does look something like the true solution. But, a direct application

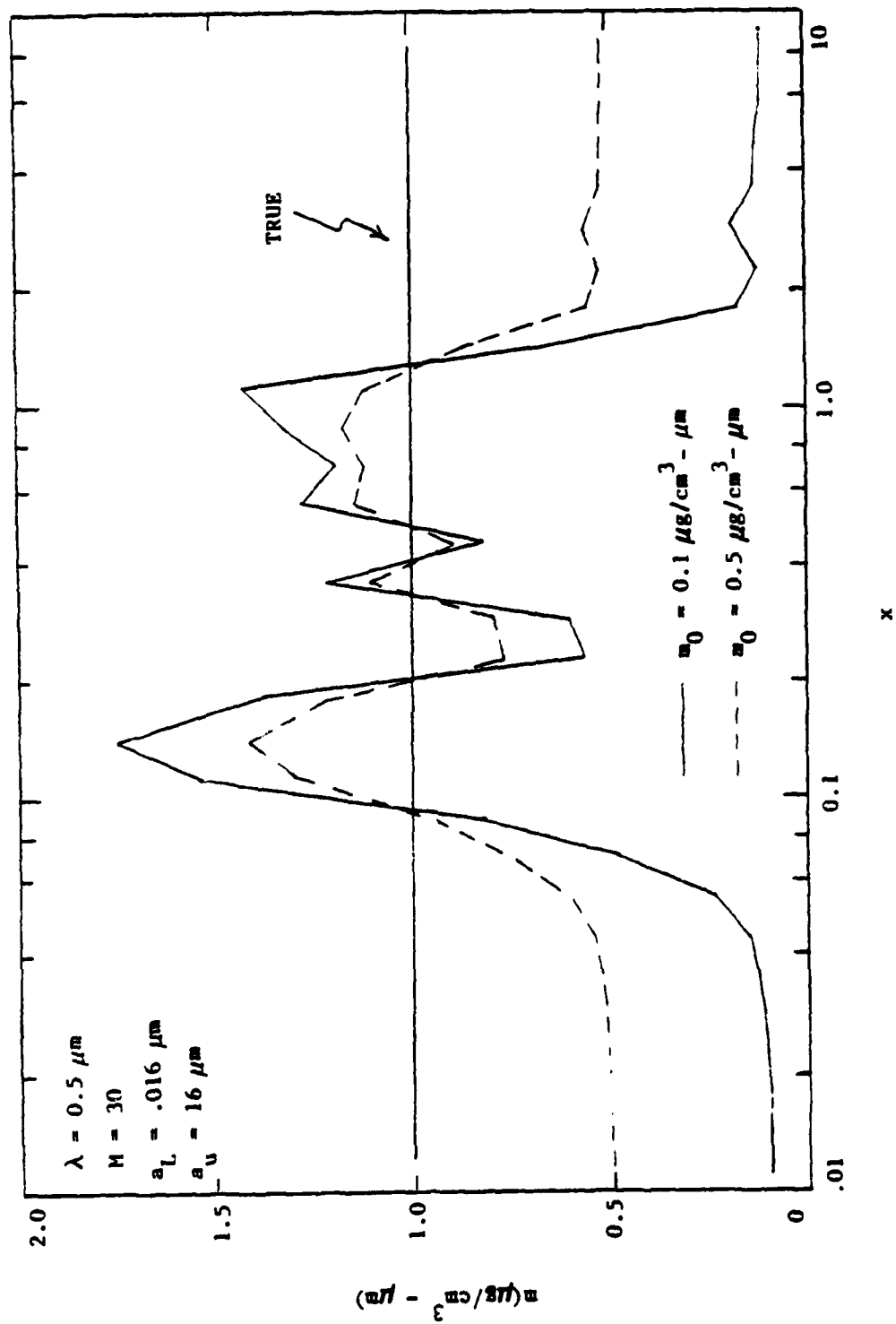


Fig. 9. Variation of Retrieval Results with Initial Guess for Uniform Size Distribution

of this approach cannot work. The solution shown in Fig. 6 is the result of 22 cycles and is less than 1% different from the result obtained at the 21st cycle. If it were used as the first guess solution in a new inversion, the new inversion would only require one cycle for convergence and the solution would be only 1% (probably less) different from the initial guess. In effect, the second inversion would merely perform the 23rd cycle of the first inversion. What is needed as a first guess for the second inversion is something that looks like the solution of Fig. 6 but is not exactly the same. The function used here is the smoothed version of the solution shown in Fig. 7. When this smoothed version of the solution was used in a second inversion, a marked improvement in the quality of the solution was obtained. But why stop here? What happens if this solution is now smoothed and used as the initial guess in a third inversion? The answer is that the solution is even better. In effect, a super-iteration is performed. And the process can be continued indefinitely. The result after five cycles of this process is shown in Figs. 10a and 10b. The improvement in results over a single inversion cycle is substantial. No significant improvement was achieved beyond five cycles.

2.8 Final Results

The preceding inversion at $\lambda = 0.6328 \mu\text{m}$ was able to retrieve the center of the size distribution with significant accuracy. No information was retrieved in the wings, however, because they were not in the retrieval window. In order to effect inversions in the wings, the window was moved by changing the wavelength. In order to retrieve in the small-size wing, $\lambda = 0.308 \mu\text{m}$ was used. This wavelength is achieved with a XeCl excimer pulsed

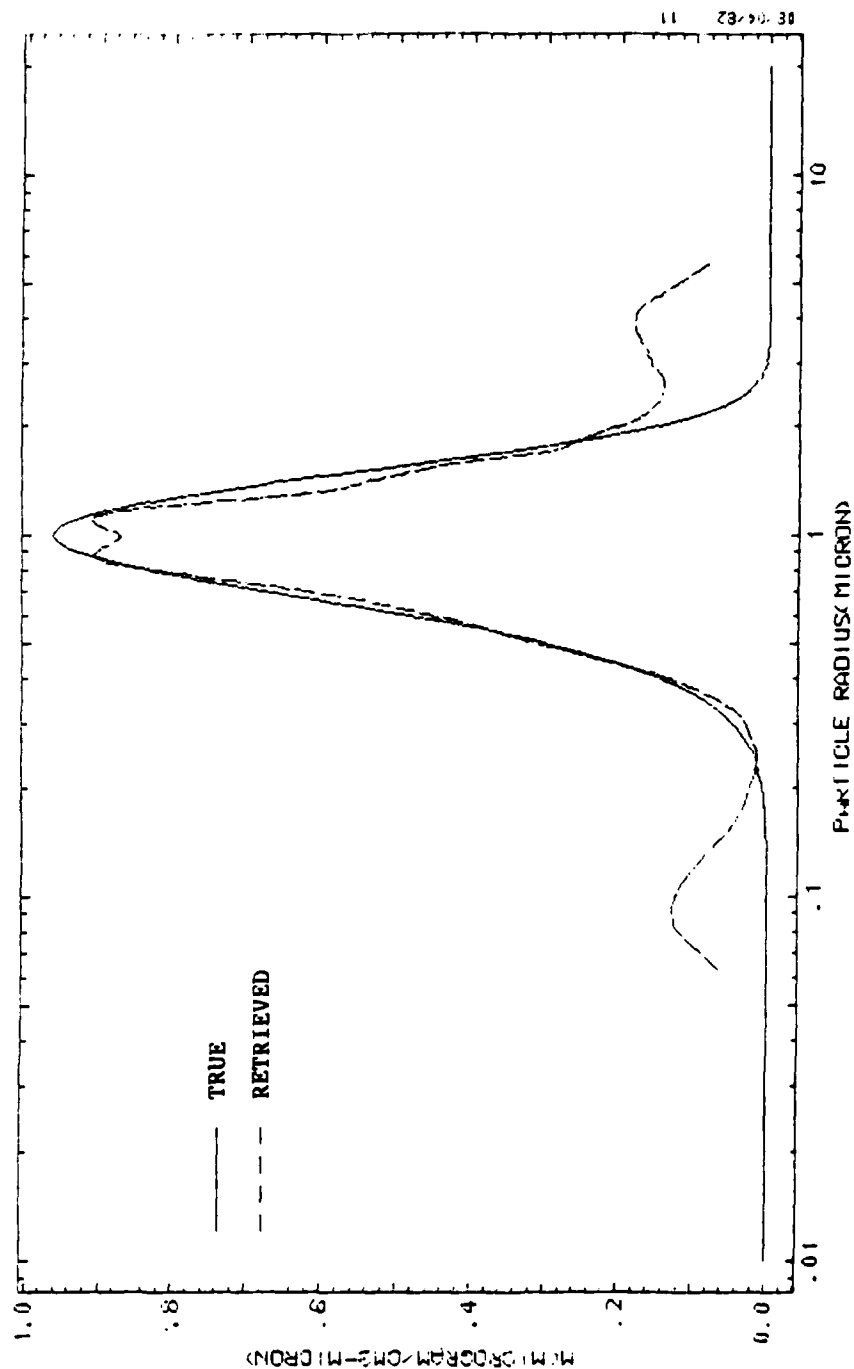


Fig 10a. Size Distribution Retrieval Results at Fifth Reiteration (Linear Plot)

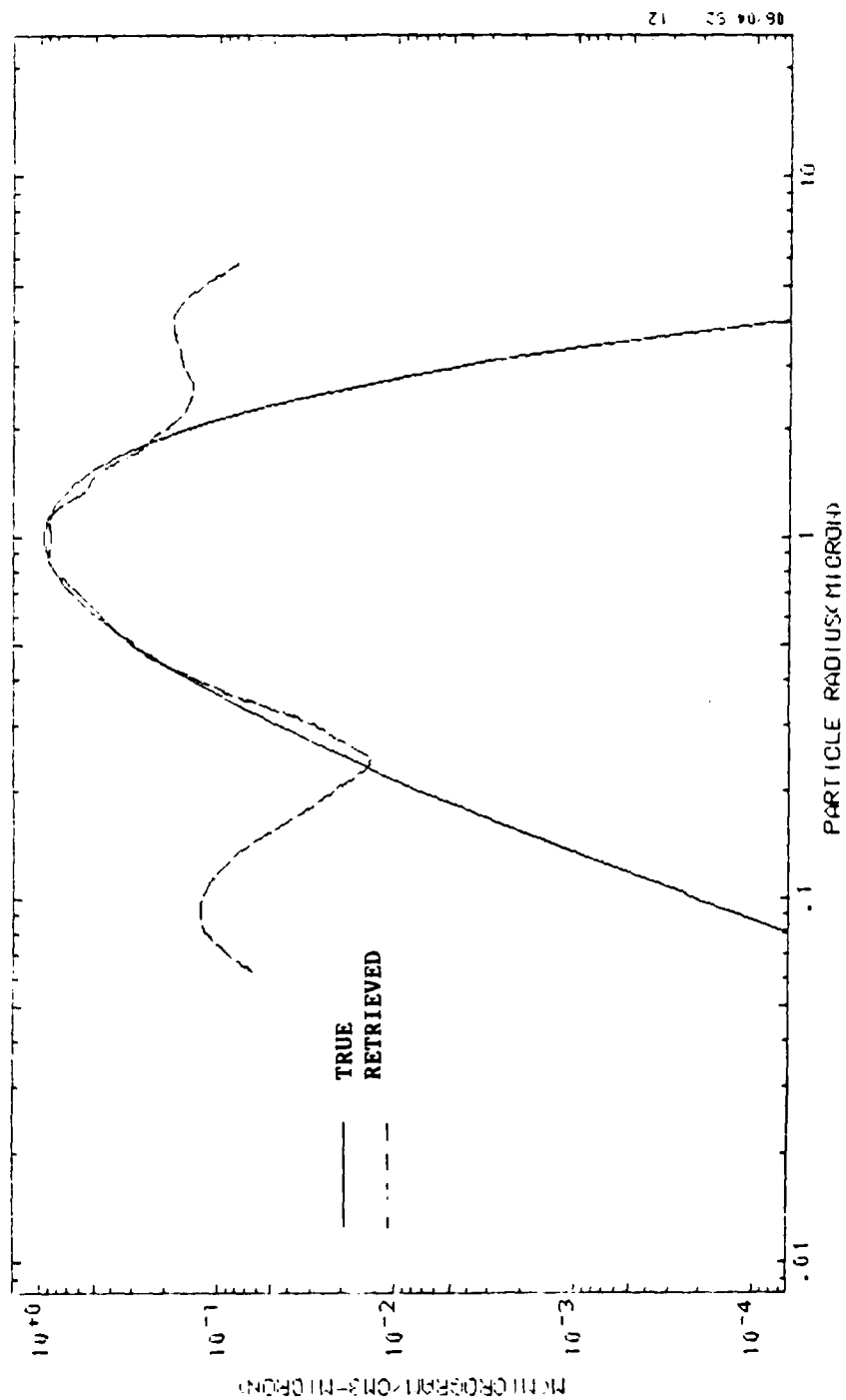


Fig 10b. Size Distribution Retrieval Results at Fifth Reiteration (Log Plot)

laser. A continuous argon ion laser operating in $\lambda = 0.33$ to $0.36 \mu\text{m}$ may be more experimentally practical. For the large-size wing, $\lambda = 1.06 \mu\text{m}$ (NdYAG laser) was chosen. The index of refraction at these two added wavelengths was assumed to be the same as at $\lambda = 0.6328 \mu\text{m}$. Also, it was confirmed that the conditions of single-scattering and negligible absorption within the plume prevailed at the new wavelengths. The results obtained for all three wavelengths at the 10th cycle of the superiteration scheme are shown in Figs. 11 through 13.

The results obtained at $\lambda = 0.308 \mu\text{m}$ are not as good as were obtained at $\lambda = 0.6328 \mu\text{m}$. First, the fluctuations caused by the influence of the kernel functions has not been eliminated as well as before. Second, although the scheme is effective in the small-size region, the retrieved result is significantly below the true result. The results obtained at $\lambda = 1.06 \mu\text{m}$ are also somewhat degraded from the quality of the $0.6328 \mu\text{m}$ results. Here, the scheme is effective in the large-size region, but yields an overprediction of the distribution. Also, retrieval in the center portion of the distribution is underpredicted.

In Fig. 14, the log-plot results for all three inversions are plotted without the true distribution. These curves would represent inversion results from experimental data. Without knowledge of the true distribution, the only thing we know is that the $\lambda = 0.308 \mu\text{m}$ curve is probably the most accurate for small sizes, the $\lambda = 0.6328 \mu\text{m}$ curve is probably most accurate for middle sizes, and the $\lambda = 1.06 \mu\text{m}$ curve is probably most accurate for large sizes. With just this information, the "objective" final distribution of Figs. 15a and 15b was constructed.

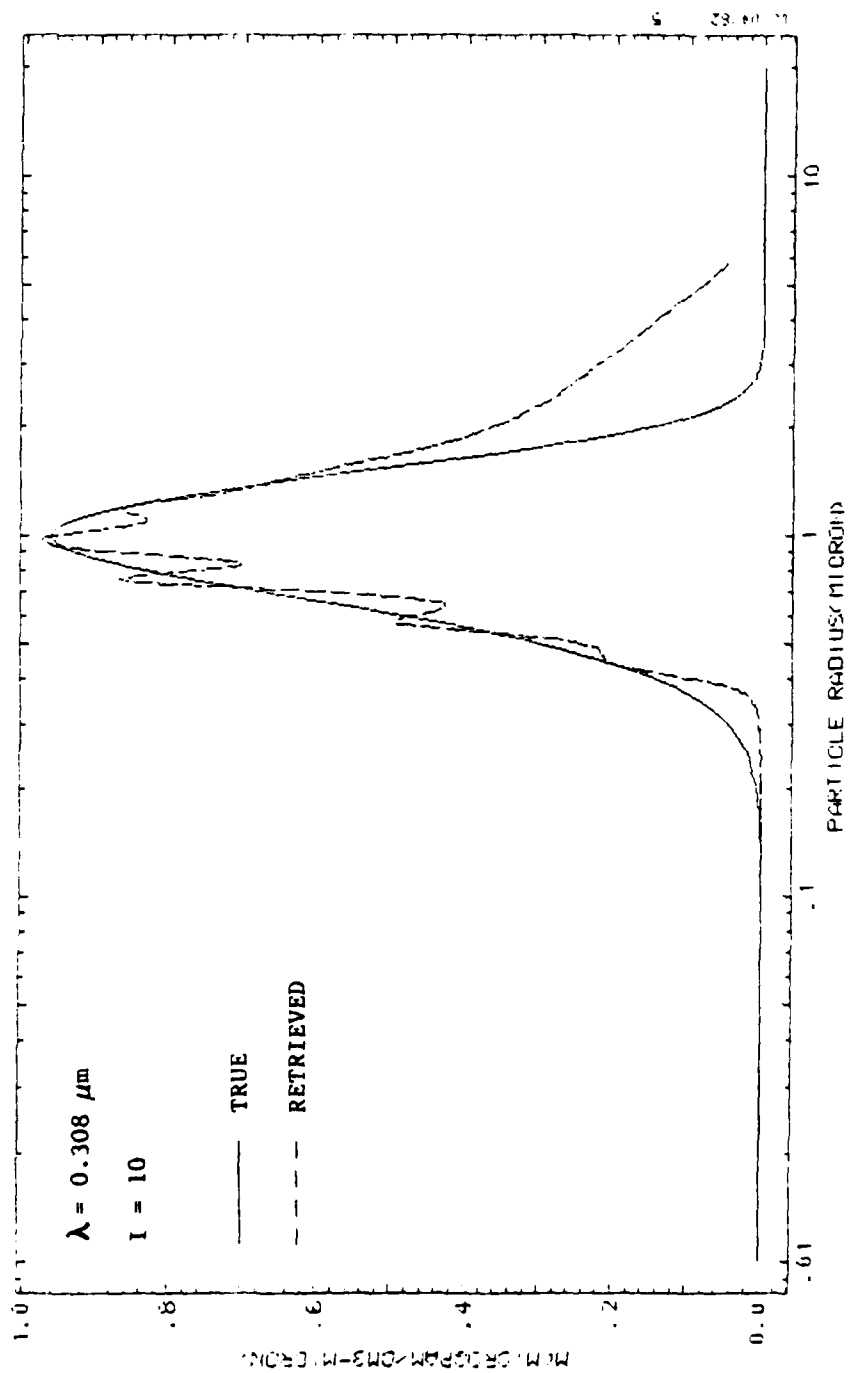


Fig. 11a. Size Distribution Retrieval Results for $\lambda = 0.308 \mu\text{m}$ (Linear Plot)

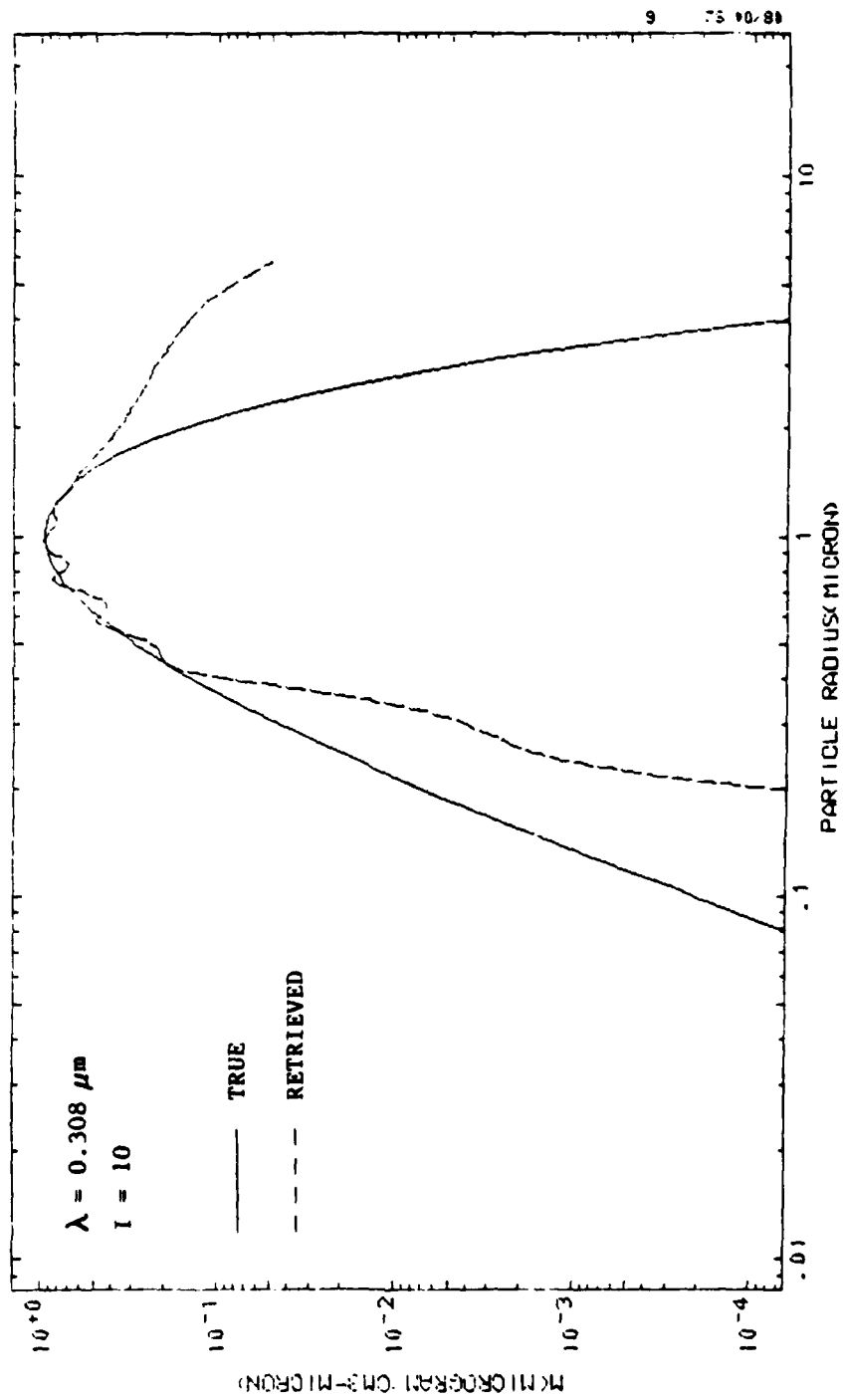


Fig. 11b. Size Distribution Retrieval Results for $\lambda = 0.308 \mu\text{m}$ (Log Plot)

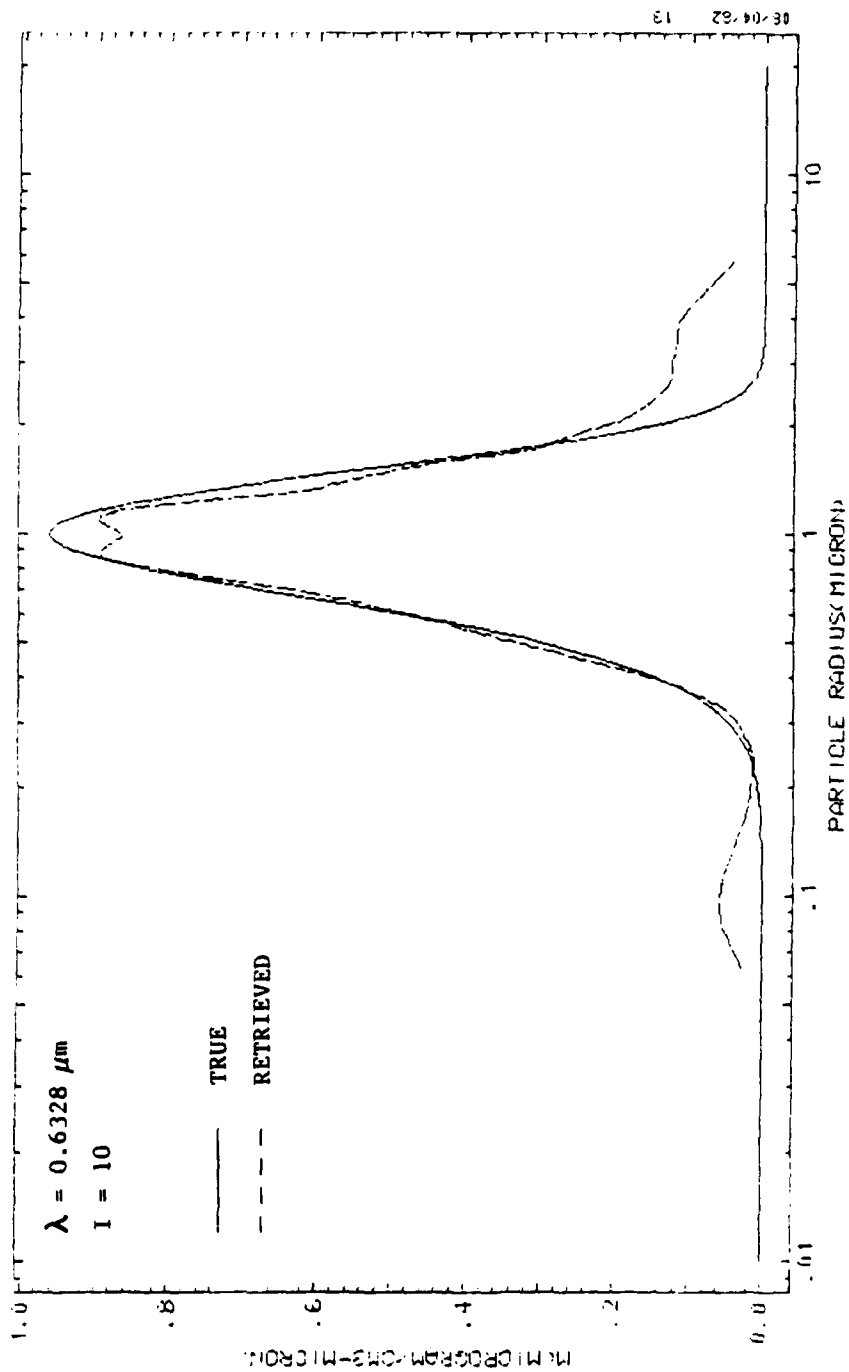


Fig.12a. Size Distribution Retrieval Results for $\lambda = 0.6328 \mu\text{m}$ (Linear Plot)

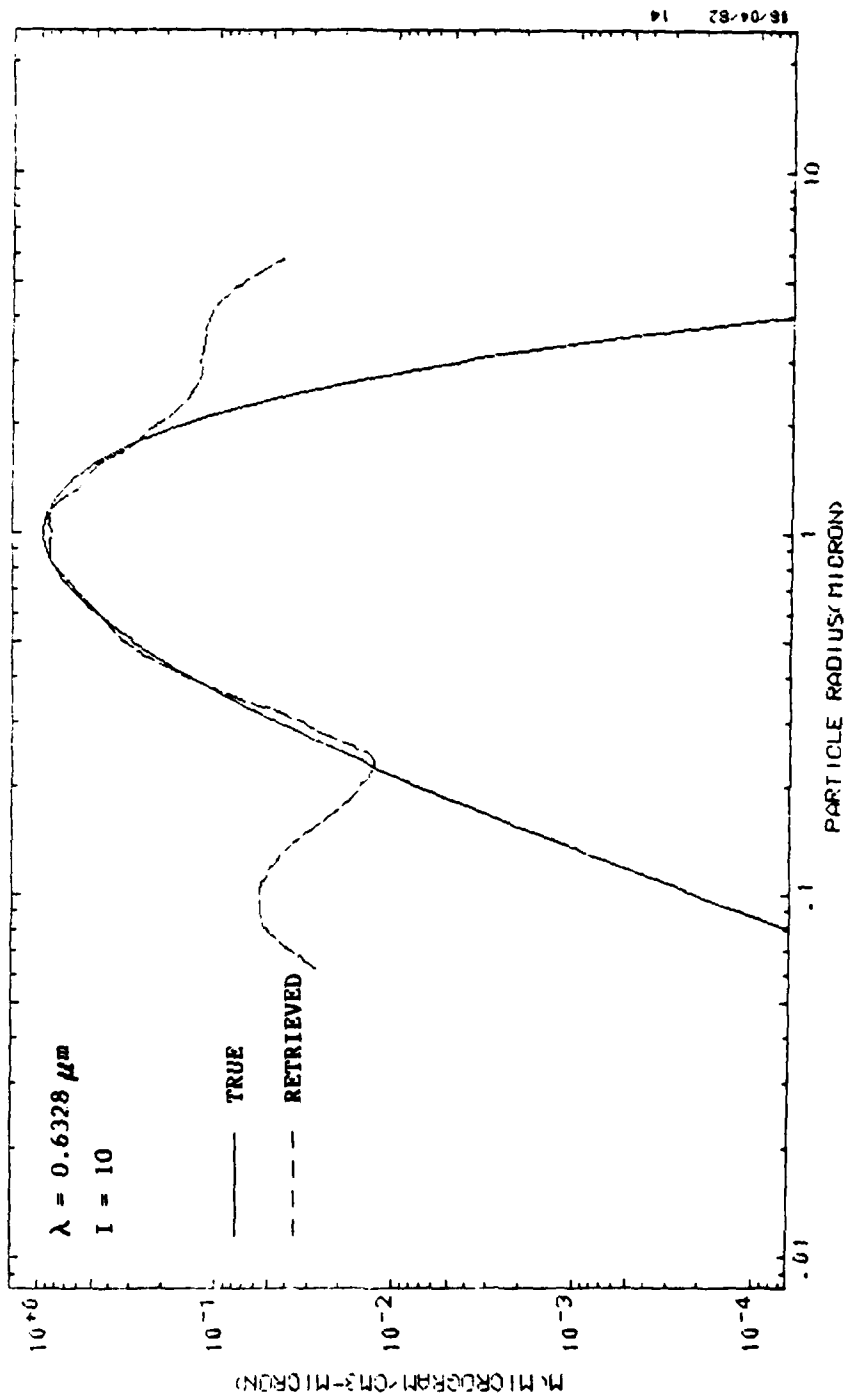


Fig. 12b. Size Distribution Retrieval Results for $\lambda = 0.6328 \mu\text{m}$ (Log Plot)

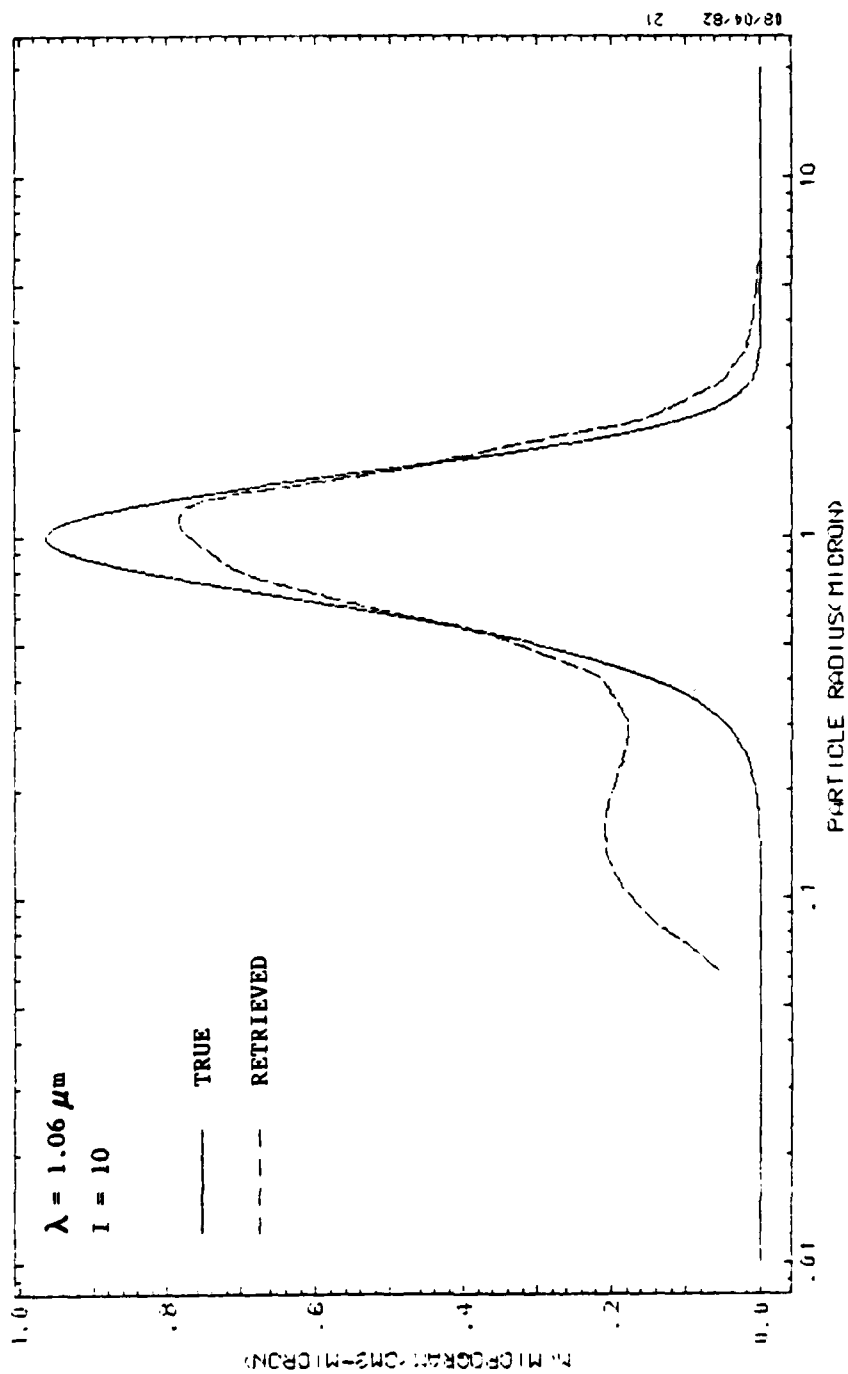


Fig. 13a. Size Distribution Retrieval Results for $\lambda = 1.06 \mu\text{m}$ (Linear Plot)

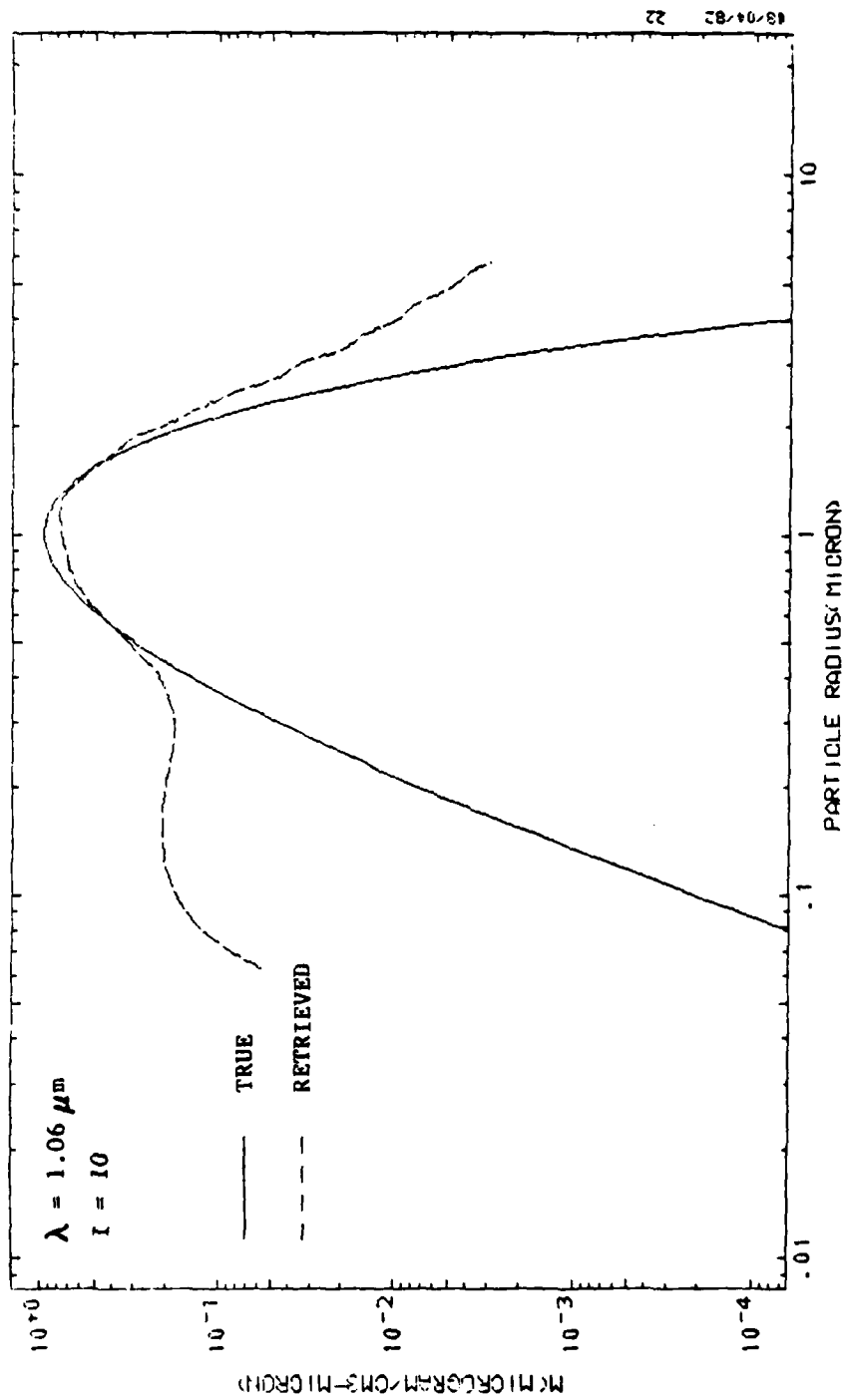


Fig.13b. Size Distribution Retrieval Results for $\lambda = 1.06 \mu\text{m}$ (Log Plot)

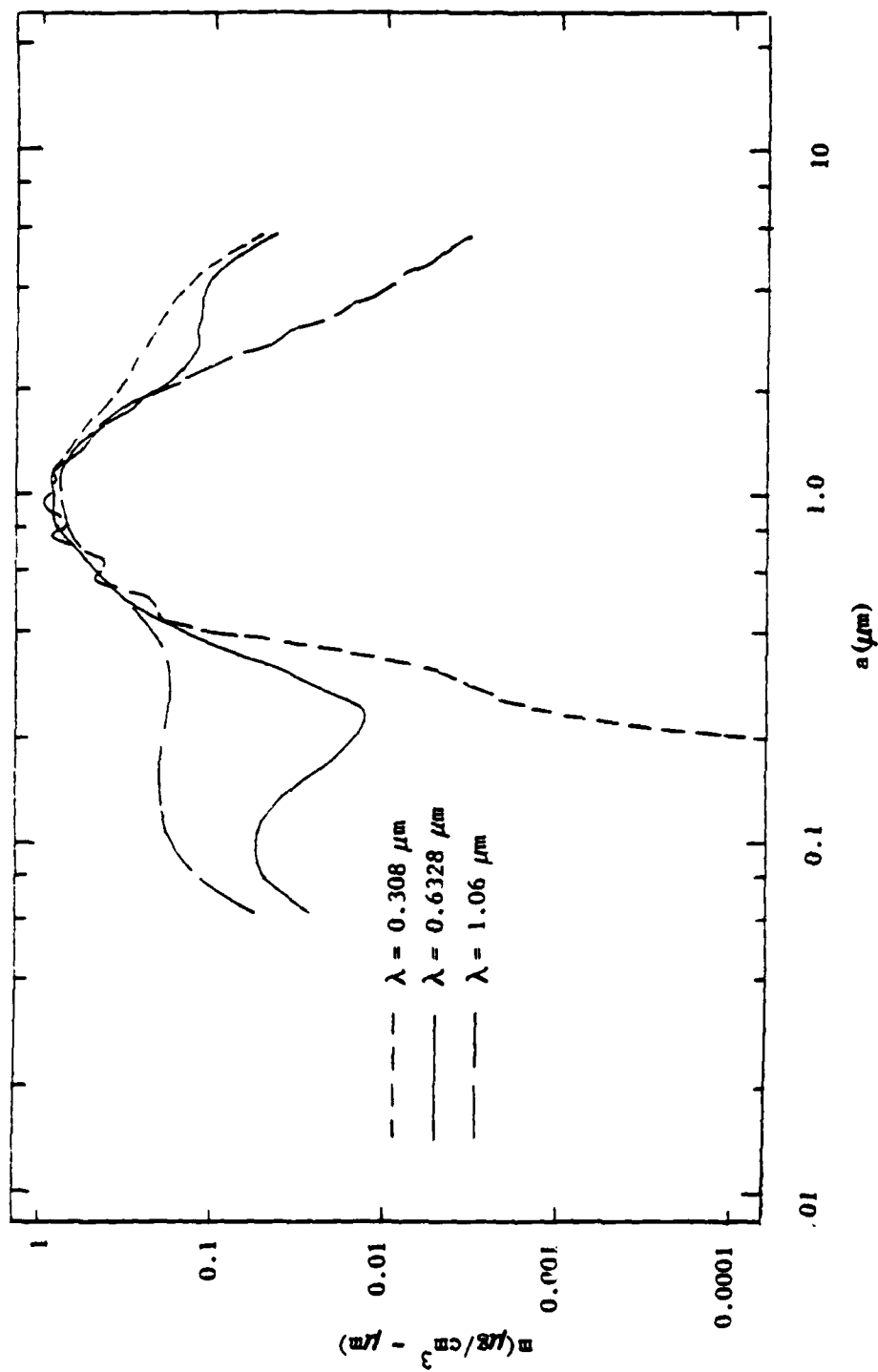


Fig. 14. Composite of Size Distribution Retrieval Results

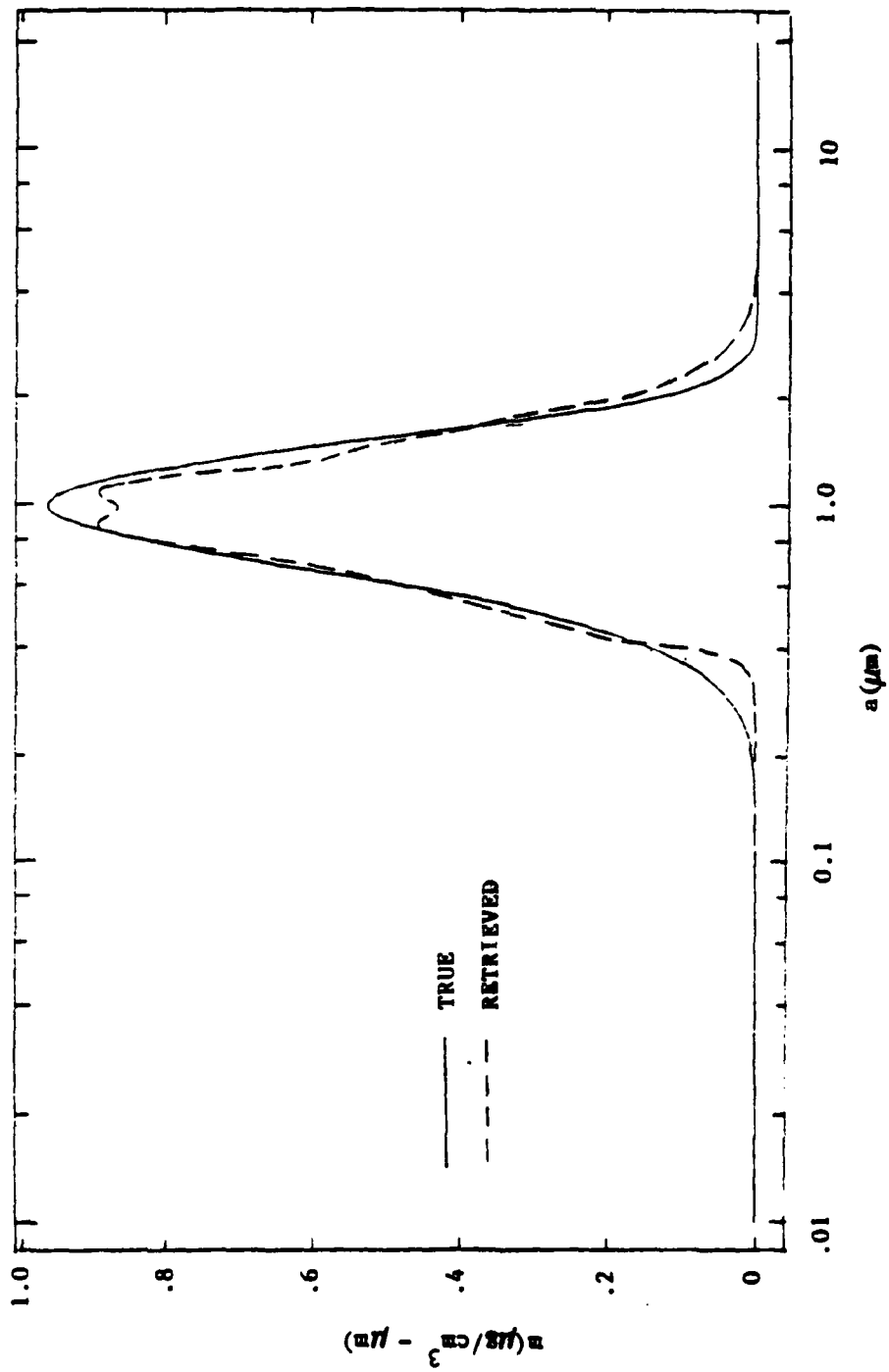


Fig. 15a. Final Size Distribution Retrieval (Linear Plot)

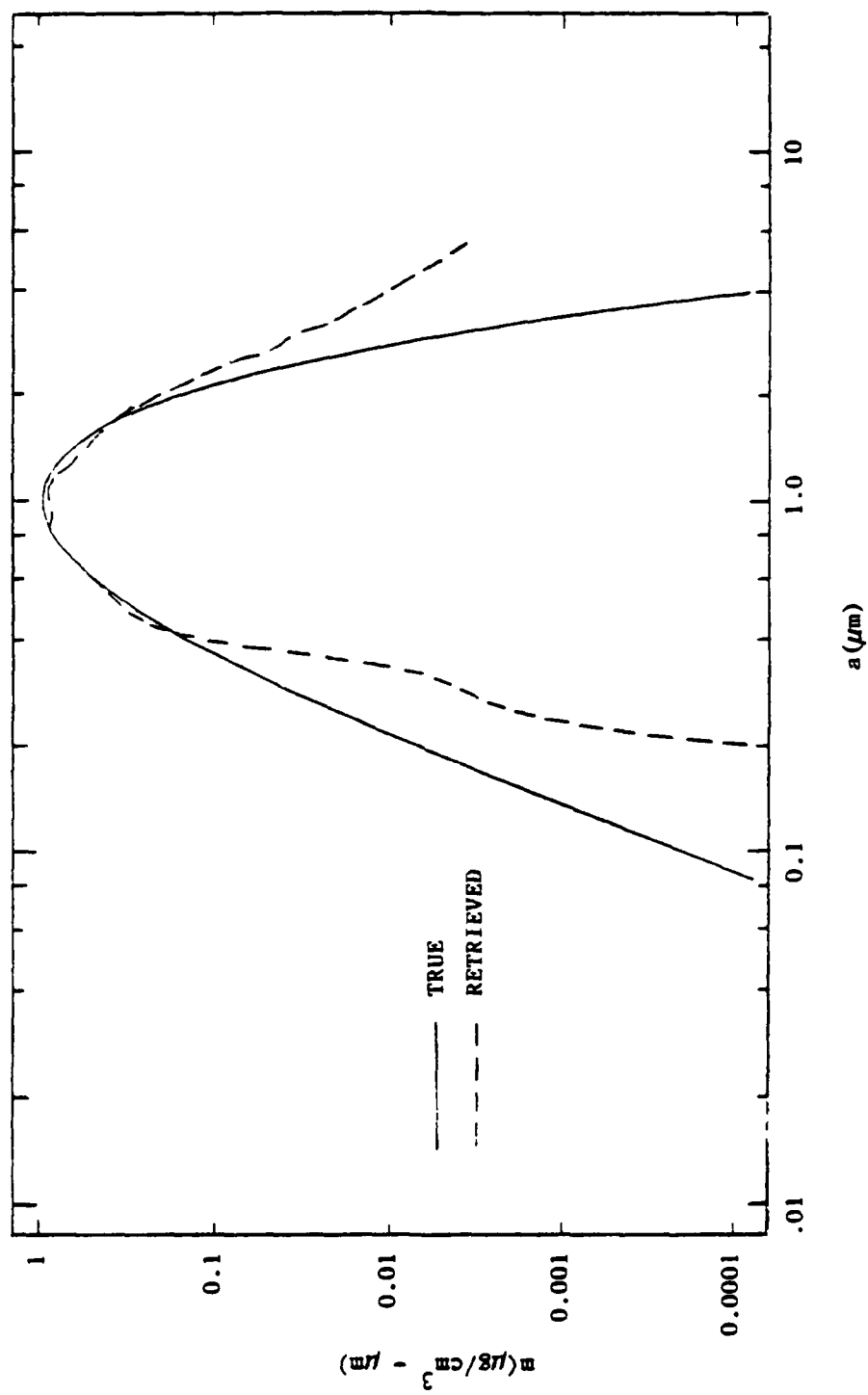


Fig. 15b. Final Size Distribution Retrieval (Log Plot)

Now for the hard part--does the result of Fig. 15 indicate a good retrieval or not? From the log plot of Fig. 15a, objection could be made to the underprediction of the small-size retrieval and the overprediction of the large-size retrieval. It should be noted, however, that truly drastic differences from the true distribution do not set in until the distribution has dropped almost an order of magnitude from its peak value. On the other hand, and from a somewhat less objective point of view, there are probably very few people familiar with size distribution retrieval in hostile environments who would judge the quality of retrieval shown in the linear plot as less than outstanding.

2.9 Error Analysis

In this section, results are reported for three studies made to assess the effects of experimental data error on the quality of retrieval using the modified Twomey nonlinear inversion procedure. The test case described above and the error-free synthetic data and retrieval results for the case are the same as shown in Figs. 5 and 15, respectively.

In the first of these studies, random errors were superimposed onto the synthetic data of Fig. 5 at the seven angles $\theta = 5.0, 7.5, 10.0, 12.5, 15.0, 17.5,$ and 20.0 deg. A computer algorithm for generating random normal numbers was used. The rms value of the superimposed error for each point was set at 5% of the value of the data point (not 5% of the peak measured values as has sometimes been done in the past). These data were then used in the modified Twomey inversion procedure to get the results of Fig. 16. This figure is a composite of results for all three wavelengths ($\lambda = 0.308, 0.6328,$ and

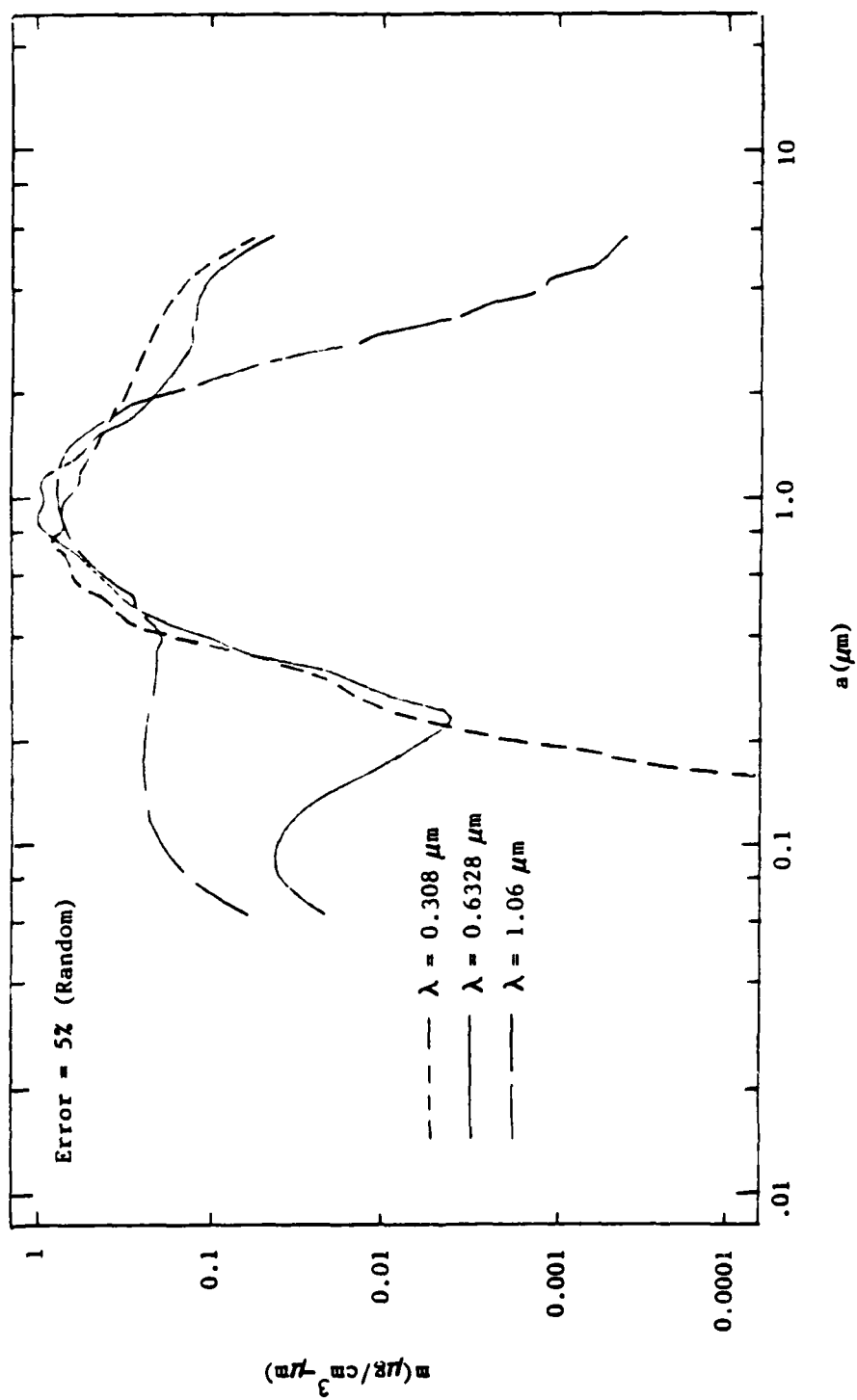


Fig.16. Composite of Size Distribution Retrieval Results for 5% Error Superposition

1.06 μm). Using the "objective" assessment that the 0.308 μm results are probably best for the small sizes, the 0.6328 μm results are best for the middle sizes, and the 1.06 μm results are best for the large sizes, the final retrieval size distribution of Fig. 17 was determined. Comparison of this result with the error-free result of Fig. 15b shows that 5% random errors do not significantly affect the quality of retrieval.

In the second study, the magnitude of errors was increased to 10%. The composite and final retrieval distributions are shown in Figs. 18 and 19, respectively. Here, it is apparent that serious degradation of the quality of retrieval has occurred. While in the error-free and 5% random error cases the error in the peak of the distribution was only a few percent, here the error is nearly a factor of two. Thus, it would appear that successful retrieval can be achieved only with measurement error not much greater than 5%. In a recent publication (Ref. 15), Trakhovsky et al. report this same maximum allowed experimental error in their application of the Twomey inversion method.

The above results were obtained for uncorrelated errors at the measurement angles. If most of the measurement noise is caused by fluctuations within the plume, and the measurements at the scattering angles are made simultaneously (that is, measurements are made at the same time with an array of detectors rather than with one angle-scanning detector), it is likely that there will be a high degree of correlation between the measurement errors.

15. E. Trakhovsky et al., *Applied Optics* 21, 3005 (1982).

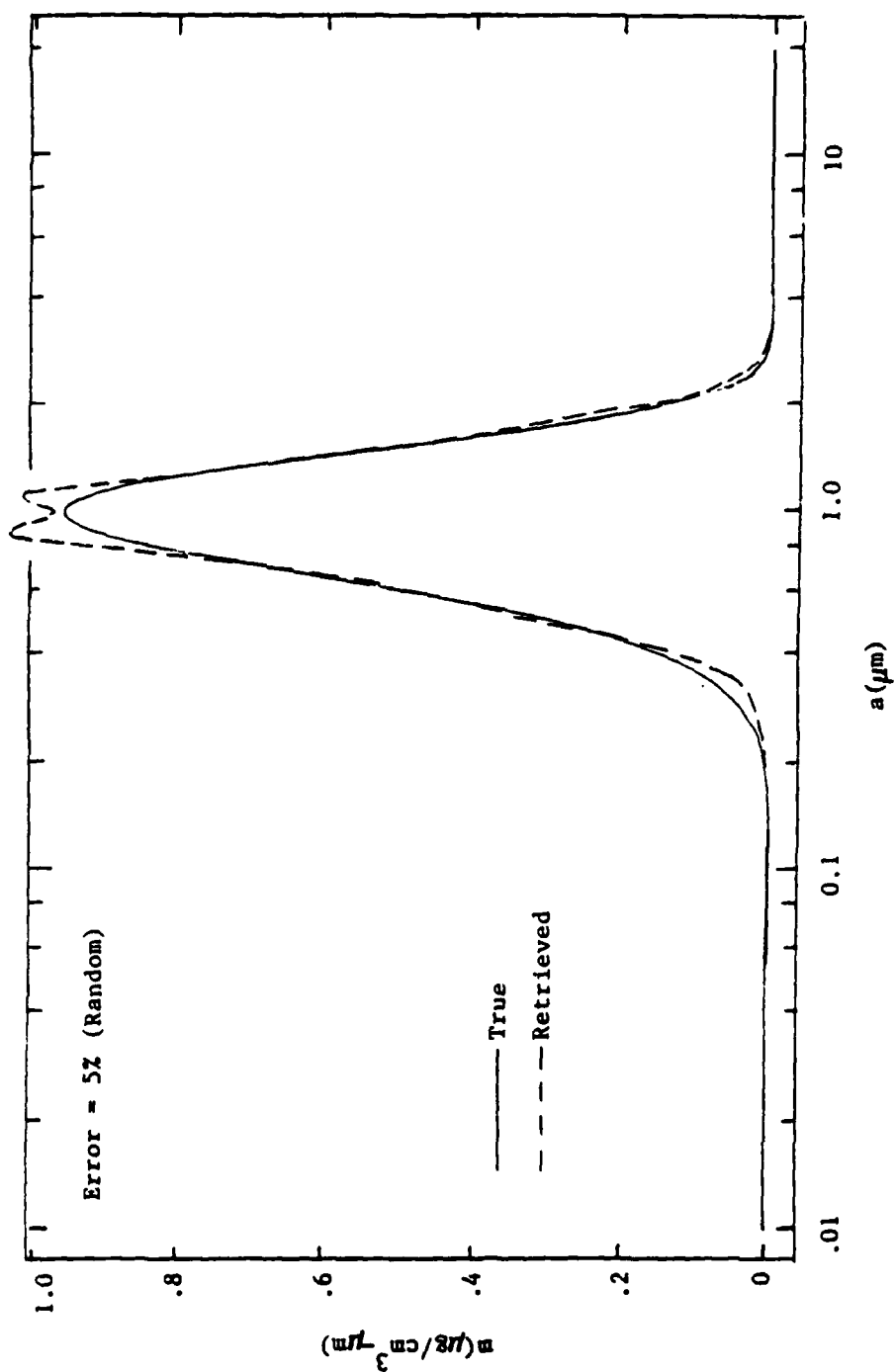


Fig. 17a. Final Size Distribution Retrieval Results for 5% Error Superposition (Linear Plot)

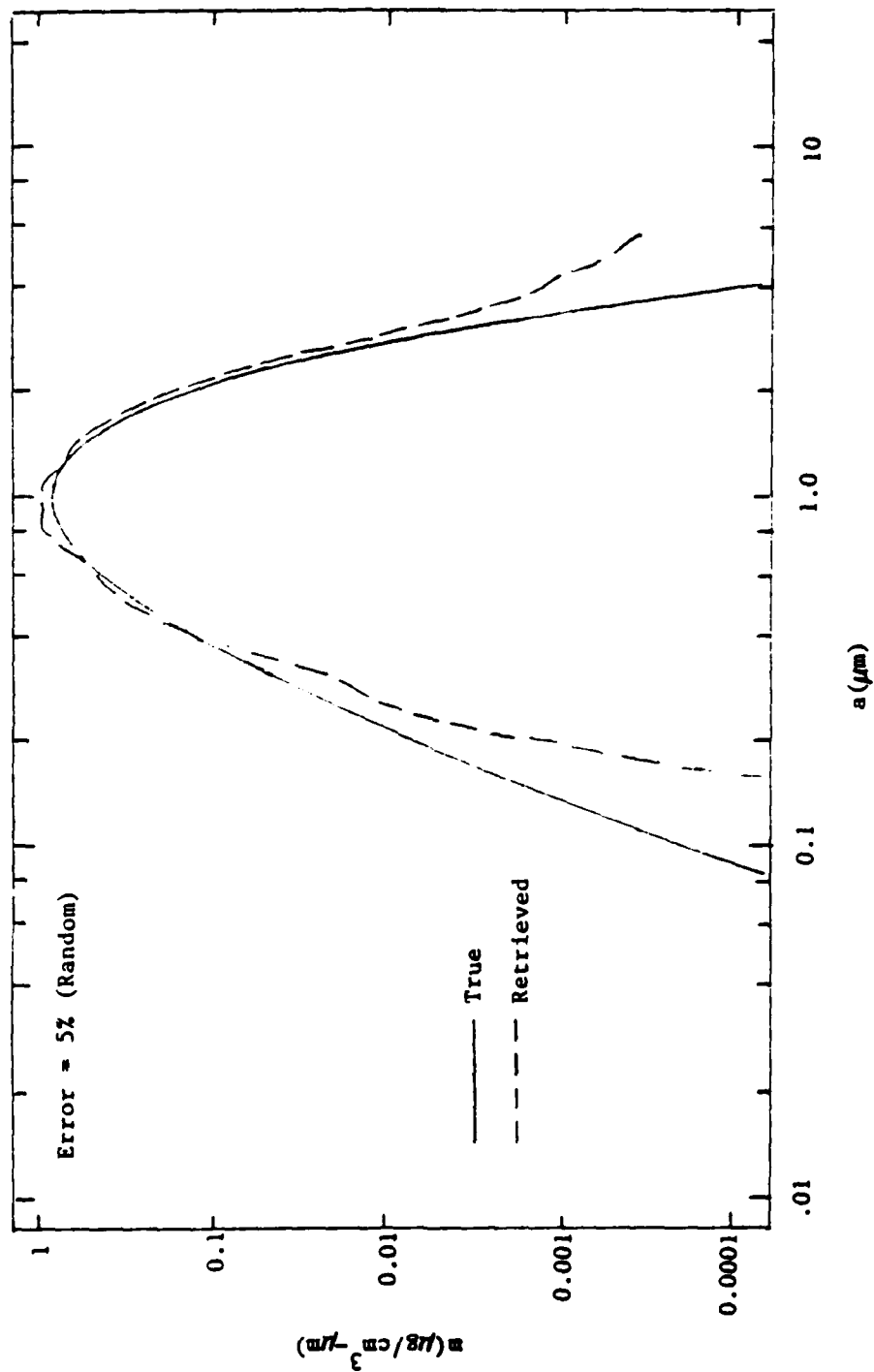


Fig. 17b. Final Size Distribution Retrieval Results for 5% Error Superposition (Log Plot)

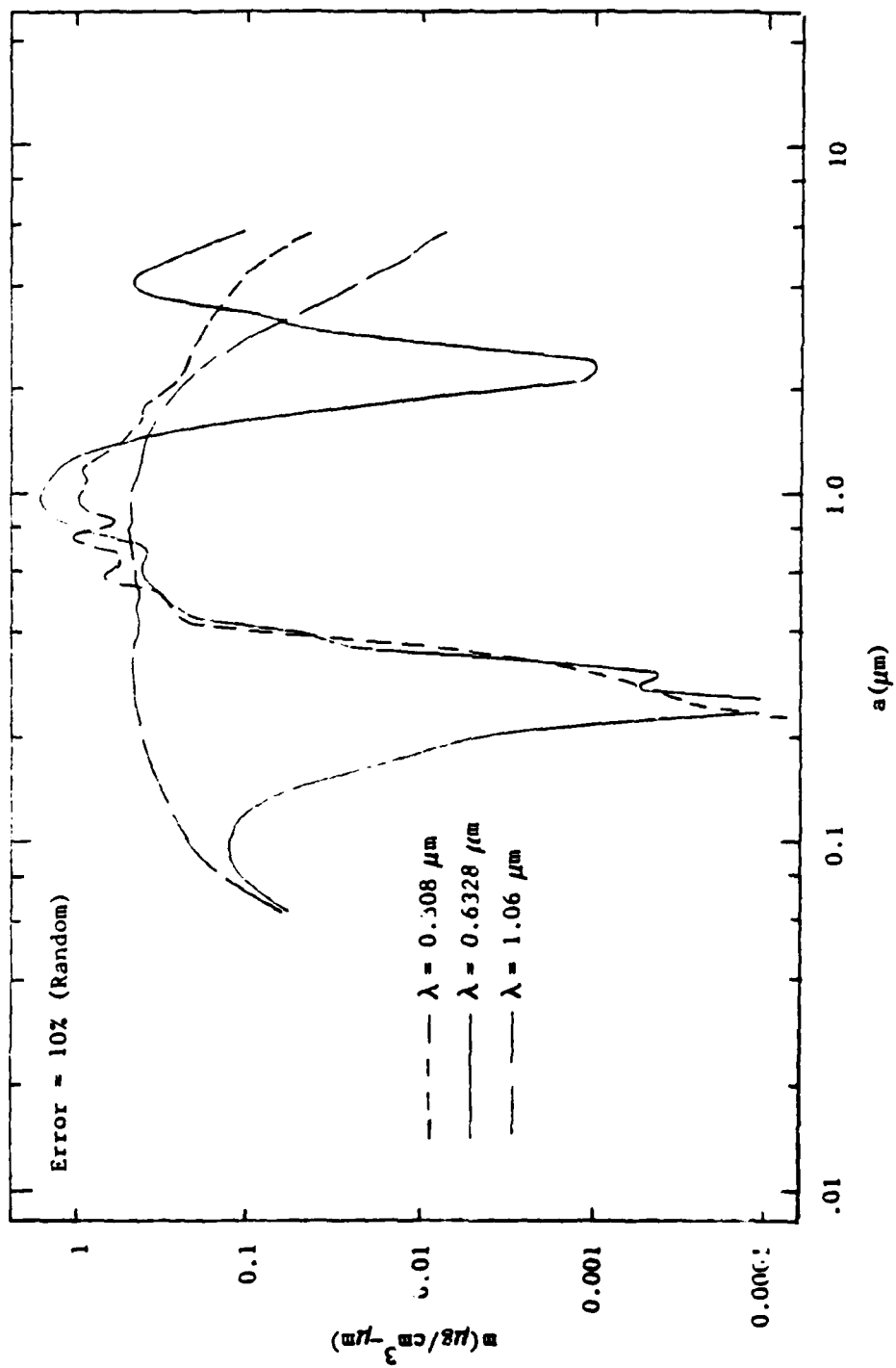


Fig. 18. Composite of Size Distribution Retrieval Results for 10% Error Superposition

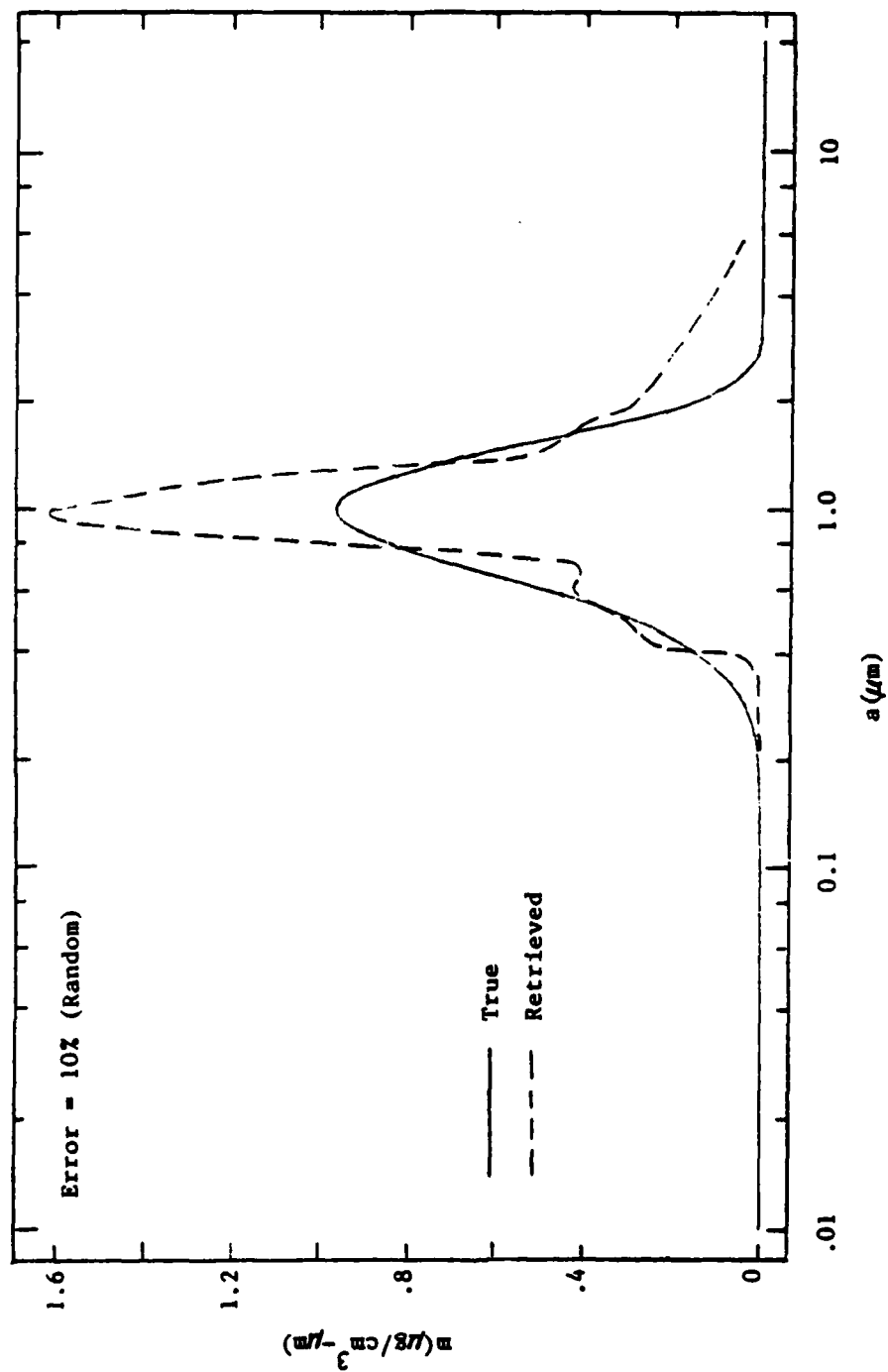


Fig. 19a. Final Size Distribution Retrieval Results for 10% Error Superposition (Linear Plot)

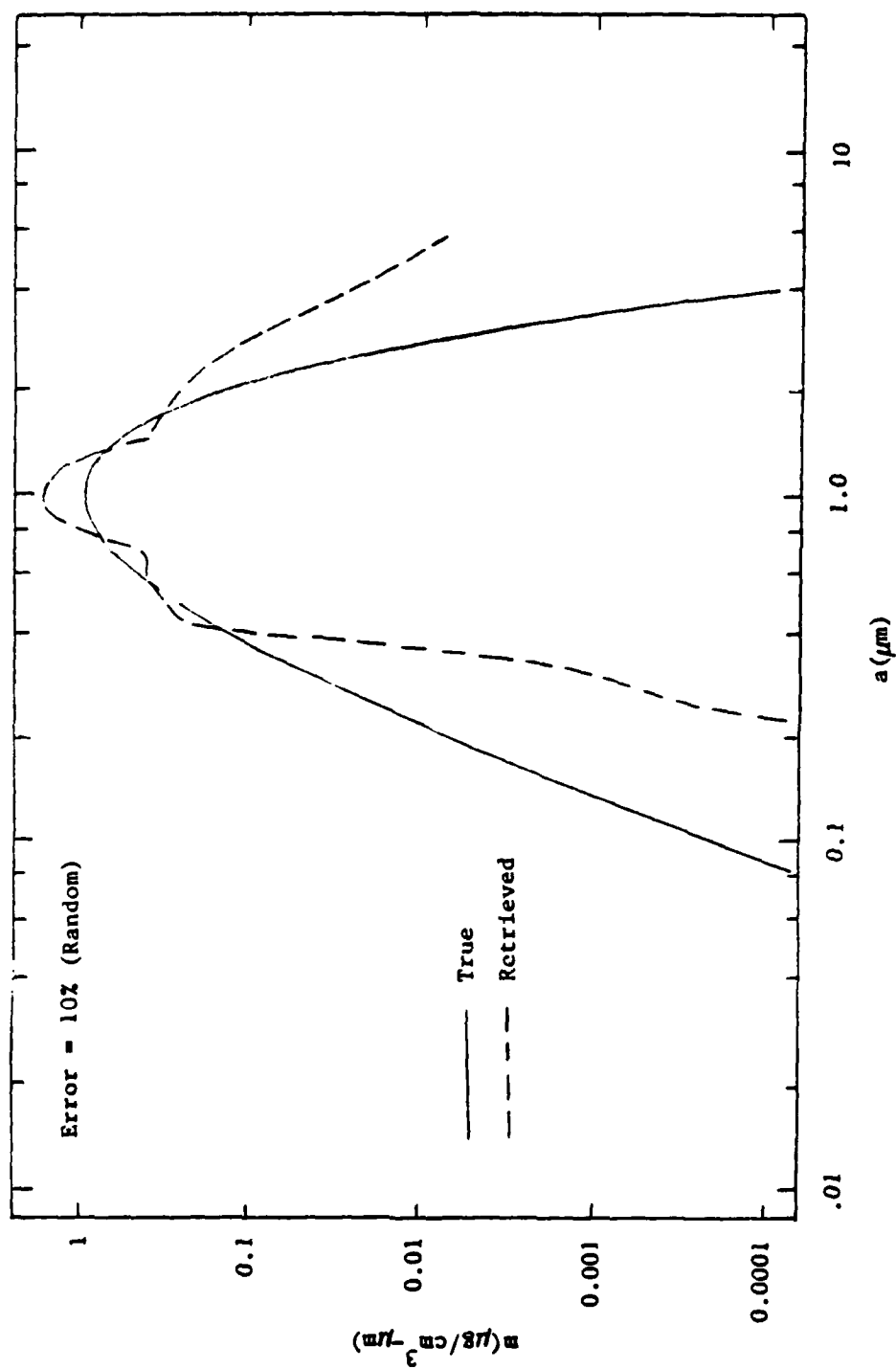


Fig. 19b. Final Size Distribution Retrieval Results for 10% Error Superposition (Log Plot)

That is, if the measured value at $\theta = 5$ deg is higher than the true value, than the measurements at all the other angles will also be high. In the third error study, the effect of this kind of bias error was investigated by performing inversions with sets of data that were uniformly 10% higher and lower than the nominal true data. The results are shown in Fig. 20. The effect is that the error propagates through the inversion to give an error in the size distribution that is the same order of magnitude as the experimental error.

The conclusion of these studies is that measurement errors up to 5% can be accommodated by the inversion routine regardless of the nature of the errors. Much beyond, and certainly before 10%, random errors destroy the usefulness of the method. However, if the measurement errors are highly correlated, experimental errors up to the magnitude of the desired accuracy of the retrieved result can be tolerated.

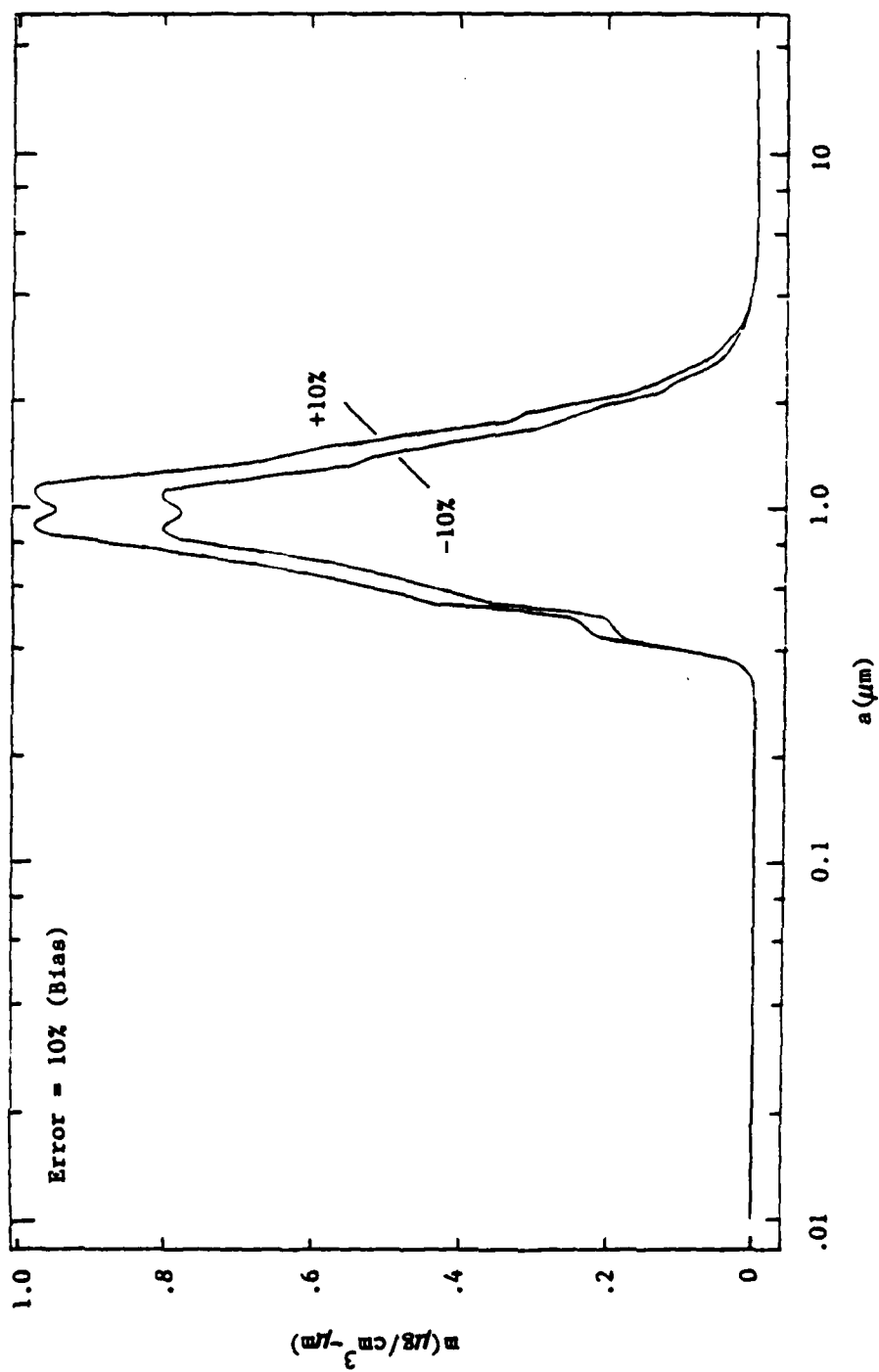


Fig. 20a. Comparison of Retrieval Size Distributions with $\pm 10\%$ Bias Error (Linear Plot)

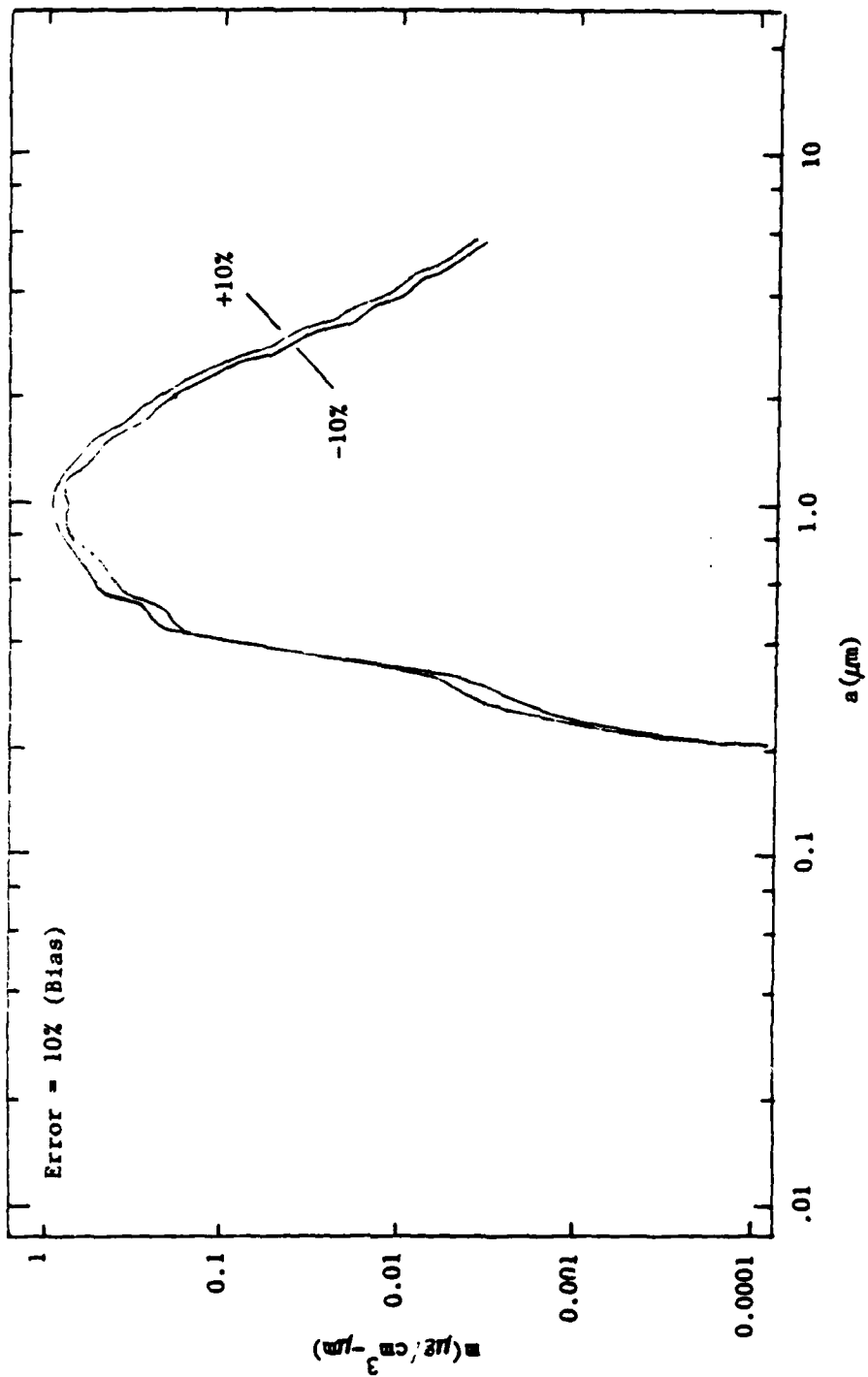


Fig. 20b. Comparison of Retrieval Size Distributions with $\pm 10\%$ Bias Error (Log Plot)

3. SIZE DISTRIBUTION FROM POLARIZATION/SCATTERING DATA

In this section, an analysis is made to determine if the scattering/angle polarization data currently being taken at AFRPL can be used to obtain information on the particle size and distribution function in the plumes of small tactical rocket motors burning low-visibility propellants. In Section 3.1, some relevant definitions are given, and a brief review of data analysis up to the point of this report is made. The possibility of performing inversion on the individual (perpendicular and parallel) component intensities of the scattered radiation is made in Section 3.2. In Section 3.3, considerations are made on inversion of the polarization data proper. These considerations revolve principally around the idea of linearizing the nonlinear equation relating polarization and size distribution. The inversion algorithm used to test the "linearized" inversion idea is discussed in Section 3.4, and results of test inversions are reported in Section 3.5. The principle result of the work is that there is little hope that the polarization data can yield any useful information on particle size characteristics.

3.1 Introduction and Review

The original goal of the scattering-angle/polarization experiment was the retrieval of the particle size distribution from measurements of the polarization of laser light scattered from a well-defined volume of plume through angles from 15 to 150 deg (15, 30, 50, 90, 130 and 150 deg). The polarization axis of the incident linearly polarized light is 45 deg to the scattering plane and thus simulates unpolarized light when the mutually perpendicular

components of the scattered light are taken to be parallel and perpendicular to the scattering plane. The scattered components are related to the unknown size distribution by

$$I_1(\theta) \equiv I_{\perp}(\theta) = C \int_0^{\infty} K_1(\theta, x) m(x) dx \quad (22a)$$

$$I_2(\theta) \equiv I_{\parallel}(\theta) = C \int_0^{\infty} K_2(\theta, x) m(x) dx \quad (22b)$$

where $m(x)$ is the mass loading size distribution, x is the dimensionless size parameter, C is a calibration constant, and $K_{1,2}$ are kernel functions. Explicitly, in terms of the Mie scattering efficiencies for the perpendicular and parallel components Q_1 and Q_2 ,

$$K_1(\theta, x) = \frac{3\pi}{2d\lambda} \frac{Q_1(\theta, x)}{x} \quad (23a)$$

$$K_2(\theta, x) = \frac{3\pi}{2d\lambda} \frac{Q_2(\theta, x)}{x} \quad (23b)$$

where d = particle bulk density and λ = wavelength. In Section 2, polarization was of no concern, and only the total functions $K = K_1 + K_2$ and $Q = Q_1 + Q_2$ were discussed (see Eqs. 16).

The polarization of the scattered radiation is

$$P(\theta) = \frac{I_1(\theta) - I_2(\theta)}{I_1(\theta) + I_2(\theta)} \quad (24)$$

A related variable, and the one which will mostly be used here, is the ratio

$$R(\theta) = \frac{I_1(\theta)}{I_2(\theta)} . \quad (25)$$

The relationship between P and R is $R = (1 + P)/(1 - P)$. Written explicitly,

$$R(\theta) = \frac{\int_0^{\infty} K_1(\theta, x) m(x) dx}{\int_0^{\infty} K_2(\theta, x) m(x) dx} . \quad (26)$$

Equation (26) provides the relationship between the desired particle size distribution function $m(x)$ and the measured data $R(\theta)$.

Apparently, the data were originally to be processed with an inversion code developed at AEDC by Curry et. al (Refs. 16 and 17). A constrained linear inversion (Phillips-Twomey method) was to be applied to Eq. (24) or (25) to retrieve $m(x)$. The problem with this approach (and which the authors recognize) is that neither Eq. (24) nor (25) is a linear integral equation [Eq. (22) is]; thus, a direct application of the method is unsuitable. Their main argument that purports to make the method suitable for linear inversion is that the denominator of Eq. (24) or (25) can be considered constant while a solution for $m(x)$ in the numerator is obtained. The $m(x)$ retrieved is then

-
16. J. W. L. Lewis et al., Determination of the Size Distribution Function for Particle in a Hypersonic Flow Field, AEDC-TR-77-101, ARO Inc., Arnold Engineering Development Center, Arnold Air Force Station, Tennessee, July 1978.
 17. B. P. Curry et al., Development of Mie Scattering Techniques for In-Situ Particle Diagnostics at AEDC, AEDC-TR-80-3, ARO Inc., Arnold Engineering Development Center, Arnold Air Force Station, Tennessee, November 1980.

used to update the denominator, and a new $m(x)$ is obtained. The iteration continues until convergence is achieved. At first glance, this approach seems reasonable, but in fact, the neglect of the variation of the denominator with $m(x)$ is a very serious error. The correct linearization of the problem is treated later in Section 3.3, and it will be shown there that the correct kernels to use are dramatically different from the ones Curry et al., used.

With the failure of the AEDC methods to make sense of the experimental data, the next analysis step seems to have been an attempt to see if the polarization data were at least consistent with mean particle sizes obtained from the one-color transmissometer data and to resolve ambiguities in the transmissometer data. It did appear to be able to this much (Ref. 14).

3.2 Linear Inversion on Polarization Components

An initial idea in the current work on analyzing the APRPL scattering data was to determine if a linear inversion, such as described in Section 2, could be performed on the individual polarization intensity components $I_1(\theta)$ and $I_2(\theta)$ since these quantities are linear in $m(x)$. Before any inversion is attempted, however, it is useful to investigate the kernel functions of the integral equations to see if an inversion is even feasible. The point of comparison for this investigation is the kernel function variations shown in Fig. 2 for the linear inversion analysis of Section 2. As discussed previously, the important feature of these kernels that allows for an inversion is the variation of the width of the functions with θ . As the angle increases from 5 to 20 deg, the width decreases while the peak height at $x \approx 2.5$ remains reasonably constant; the kernels act as a variable-width bandpass filter with the lower cut-off fixed. As θ changes, the proportion of different regions of x that contribute to the integral changes in such a way that a retrieval for

$m(x)$ is nondegenerate.

The kernels for $I_1(\theta)$ at the three smallest angles in the AFRPL array (i.e., 15, 30 and 50 deg) are shown in Fig. 21. Angles greater than 50 deg have not been considered since the signal levels are very low and noisy. The kernels of Fig. 21 have been scaled to unity at their peak value. The corresponding kernels for $I_2(\theta)$ or $I(\theta)$ are virtually the same. Clearly, the angles used in Fig. 21 do not provide for as pretty a variation of width with θ as is displayed in Fig. 2 or for as neat an interpretation.

The only obvious changes with θ in the kernels that might lead to enough differentiation to allow an inversion are the disappearance of the peak near $x = 6.5$ when θ is increased from 15 deg, and the small shifting of the main peak to lower x as θ increases. Without performing an actual inversion, it is difficult to know whether or not these changes are enough.*

Furthermore, the overall width of the kernel functions in Fig. 21 do not provide for as large a retrieval range as those in Fig. 2. In Section 2, it was established that a very good estimate of retrieval range was the region between the points where the widest kernel function achieved half its peak height. For Fig. 2, this region is $2 < x < 20$ and provides a range of about a factor of 10. From Fig. 21, generously using the 50-deg curve for the lower limit and the 15-deg curve for the upper limit, the retrieval range is $1.3 < x < 7.0$, a factor of only ~ 5 . Even with a factor of 10, in the Section 2 work it was necessary to use three wavelengths in order to move the retrieval range over the expected width of the size distribution. With the fixed single

*

It is possible to perform an eigenvalue analysis of kernel functions to determine beforehand whether or not a successful inversion is likely. No such analysis was performed here. Further details of the method can be found in Ref. 9.

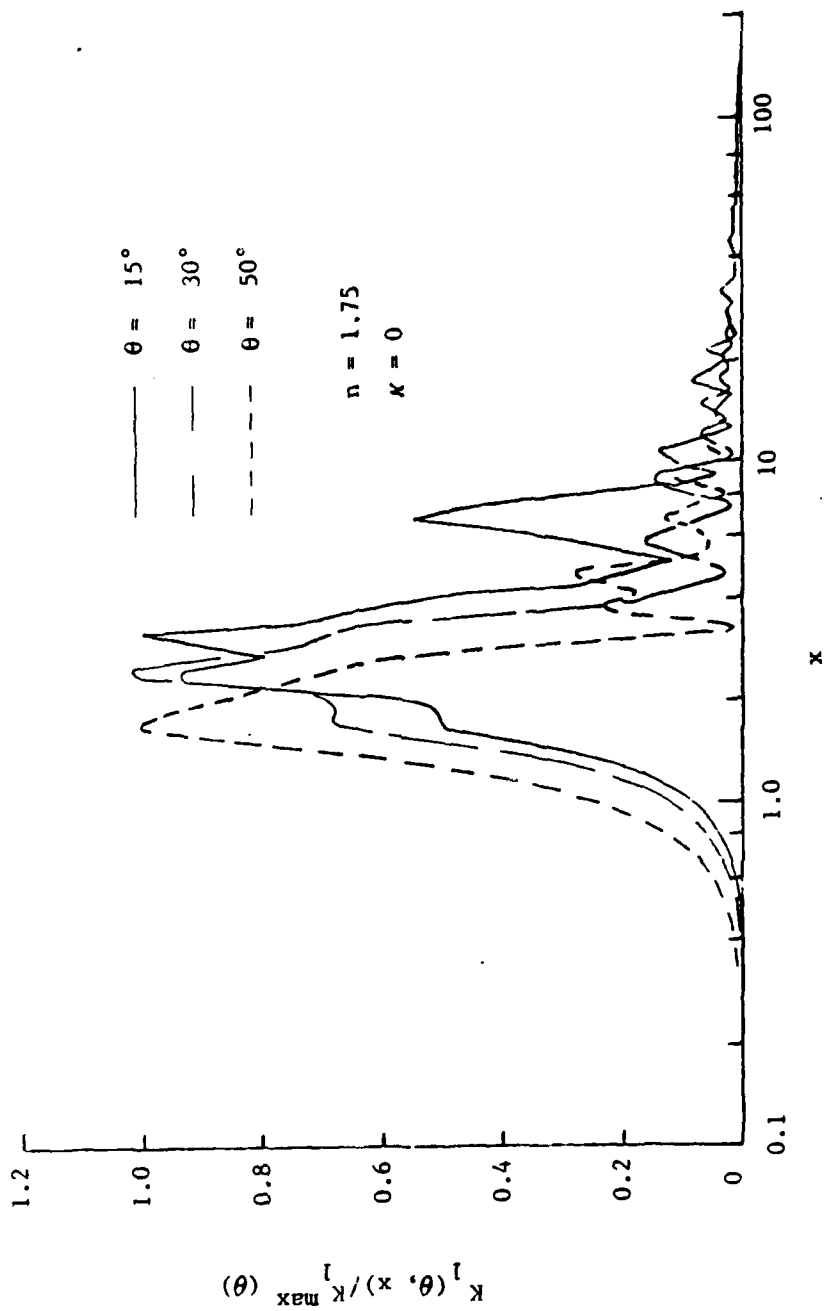


Fig. 21. Scattering Kernel Functions for $I_1(\theta)$

wavelength of $\lambda = 0.5145 \mu\text{m}$ in the AFRPL scattering experiment, retrieval could be achieved only in the radii range $0.1 \leq a \leq 0.6$.

Another problem with performing a linear inversion analysis on I_1 or I_2 or $I_1 + I_2$ is that the calibration constant C is unknown (probably) so that at best, a successful inversion would give only a relative profile for $m(x)$. On the whole this approach did not appear promising, and it was decided not to proceed with it. (In hindsight, it might have been worth doing it, however, since the method that was pursued failed.)

3.3 Linearization of Polarization Equation

Analysis of polarization or ratio data is beset at the beginning with two significant disadvantages. First, an absolute size distribution cannot come from polarization data. If the distribution is $m(a) = Mf(a)$ where $f(a)$ is a relative distribution and M is any constant (say total mass loading) then substitution into Eq. (26) shows that $R(\theta)$ does not depend at all on M because it cancels in the numerator and denominator. Thus, as for uncalibrated scattered intensity data, only a relative distribution can be retrieved. In the following analysis, this restriction must be kept in mind.

The second disadvantage is, of course, that neither $P(\theta)$ nor $R(\theta)$ is linear in $m(x)$, and a method of making an a priori analysis by way of kernel functions is not entirely clear. The analysis here employs a first-order expansion of the nonlinear Eq. (26) in order to get an approximate linear equation. The goal is to obtain an expansion of $R(\theta)$ to first order in $m(x)$ about a size distribution $m_0(x)$. If the integrations in both the numerator and denominator of Eq. (26) are approximated by quadrature summations of the form

$$\int_0^{\infty} K_{1,2}(\theta, x) m(x) dx = \sum_i K_i^{(1,2)}(\theta) m_i \Delta x \quad (27)$$

then the derivative of $R(\theta)$ with respect to the mass concentration in the j th x interval Δx is

$$\frac{\partial R(\theta)}{\partial m_j} = \frac{K_j^{(1)}(\theta)}{\int_0^{\infty} K_2(\theta, x) m(x) dx} \left(1 - \frac{R(\theta)}{R(\theta, x)}\right) \Delta x \quad (28)$$

where

$$R(\theta, x) = \frac{K_1(\theta, x)}{K_2(\theta, x)} \quad (29)$$

The first-order expansion of $R(\theta)$ about $R_0(\theta)$ is then

$$\begin{aligned} R(\theta) &= R_0(\theta) + \sum_j \left. \frac{\partial R(\theta)}{\partial m_j} \right|_0 (m_j - m_j^0) \\ &\approx R_0(\theta) + \int_0^{\infty} K'(\theta, x) m(x) dx \end{aligned} \quad (30)$$

where $R_0(\theta)$ is obtained from Eq. (26) using $m_0(x)$ for $m(x)$, $\partial R(\theta)/\partial m_j|_0$ is obtained from Eq. (28) using $m_0(x)$ for $m(x)$, and $K'(\theta, x)$ is the linear approximation kernel

$$K'(\theta, x) = \frac{K_1(\theta, x)}{\int_0^\infty K_2(\theta, x) m_0(x) dx} \left(1 - \frac{R_0(\theta)}{R(\theta, x)}\right). \quad (31)$$

Figure 22 shows $K'(\theta, x)$ for the AFRPL angle array. $m_0(x)$ has been taken as a uniform distribution of unit mass $m_0(x) = 1 \text{ g/cm}^3$.

These linear approximation kernels are dramatically different from the kernels for the purely linear case in that they are more widely fluctuating and assume negative values. The ability of these kernels to be negative is a direct consequence of not assuming the denominator of Eq. (26) to be constant, as in the Curry method. The corresponding kernel for that method is

$$K'(\theta, x) = \frac{K_1(\theta, x)}{\int_0^\infty K_2(\theta, x) m_0(x) dx}. \quad (32)$$

If a constrained linear inversion were to be carried out, it should be made with Eqs. (30) and (31) by assuming some initial $m_0(x)$, computing $R_0(x)$ from Eq. (26) and treating $R(\theta) - R_0(\theta)$ as the experimental data. The new $m(x)$ obtained by solving Eq. (30) would then be a new initial $m_0(x)$ for the next iteration. Each step of the iteration is a linear inversion, and Eq. (31), not Eq. (32) is the proper inversion kernel to use. Note that unlike a purely linear inversion, the inversion kernel must be updated with the new $m_0(x)$ at each iteration step.

The ability to effect an inversion of $P(\theta)$ or $R(\theta)$ to get $m(x)$ by any method lies in the independence of the kernels shown in Fig. 22. It is difficult to tell just by looking at them whether or not they are; nor is it clear how to accurately judge a retrieval range. At the very best, retrieval can be affected only in the x range where the kernels are significantly different

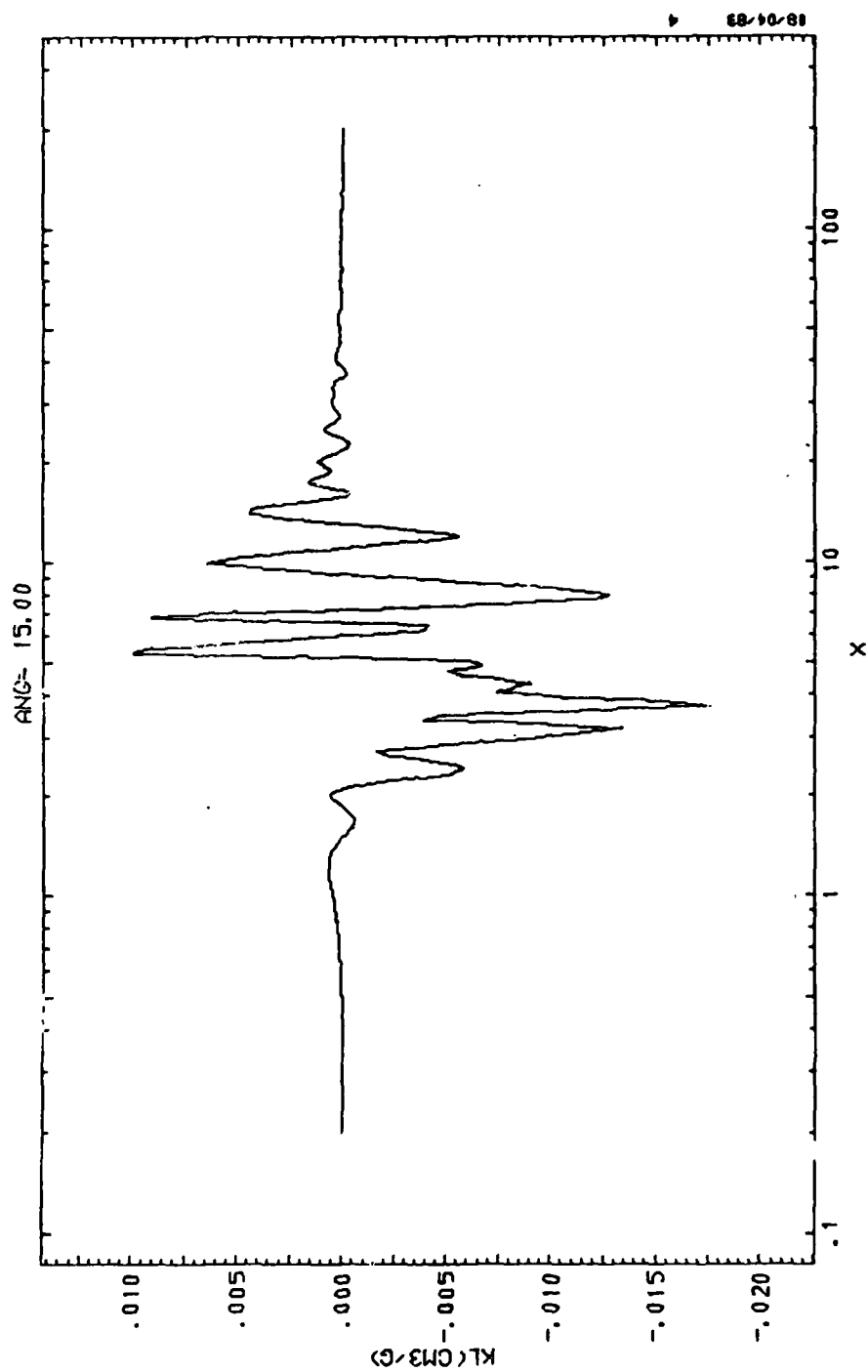


Fig. 22a. Linear Approximation Scattering Kernel ($\theta = 15$ deg)

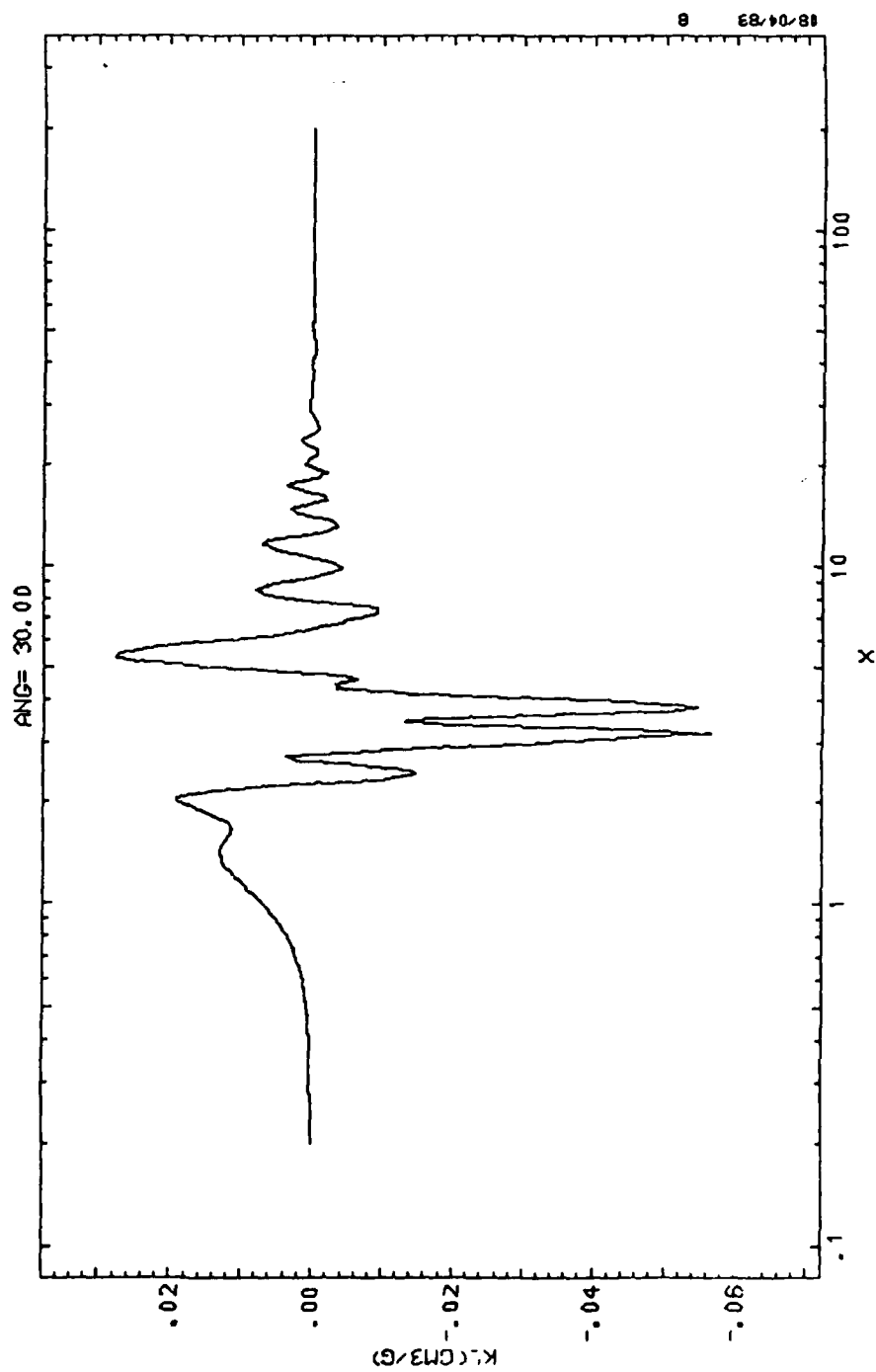


Fig. 22b. Linear Approximation Scattering Kernel ($\theta = 30$ deg)

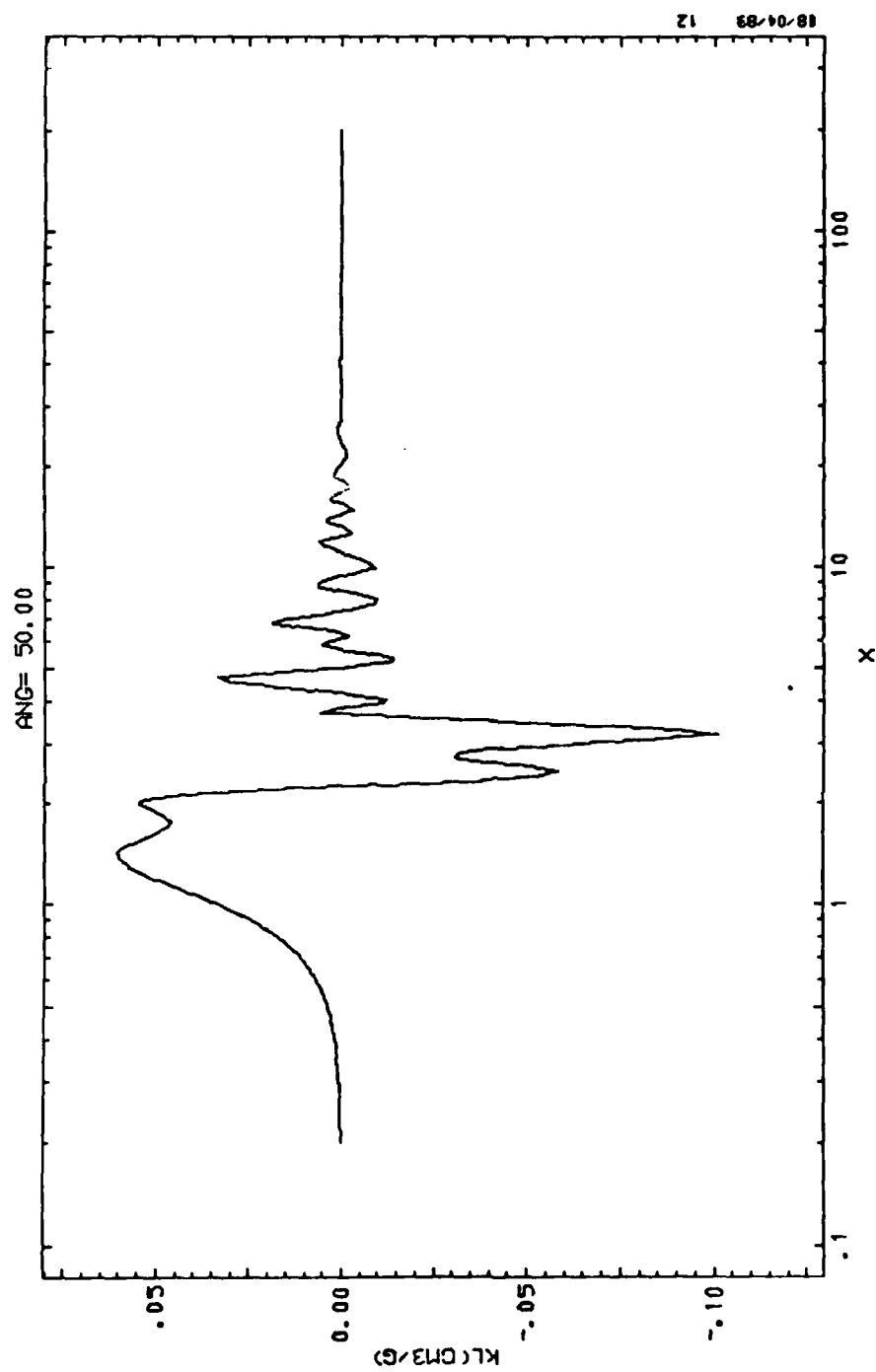


Fig. 22c. Linear Approximation Scattering Kernel ($\theta = 50$ deg)

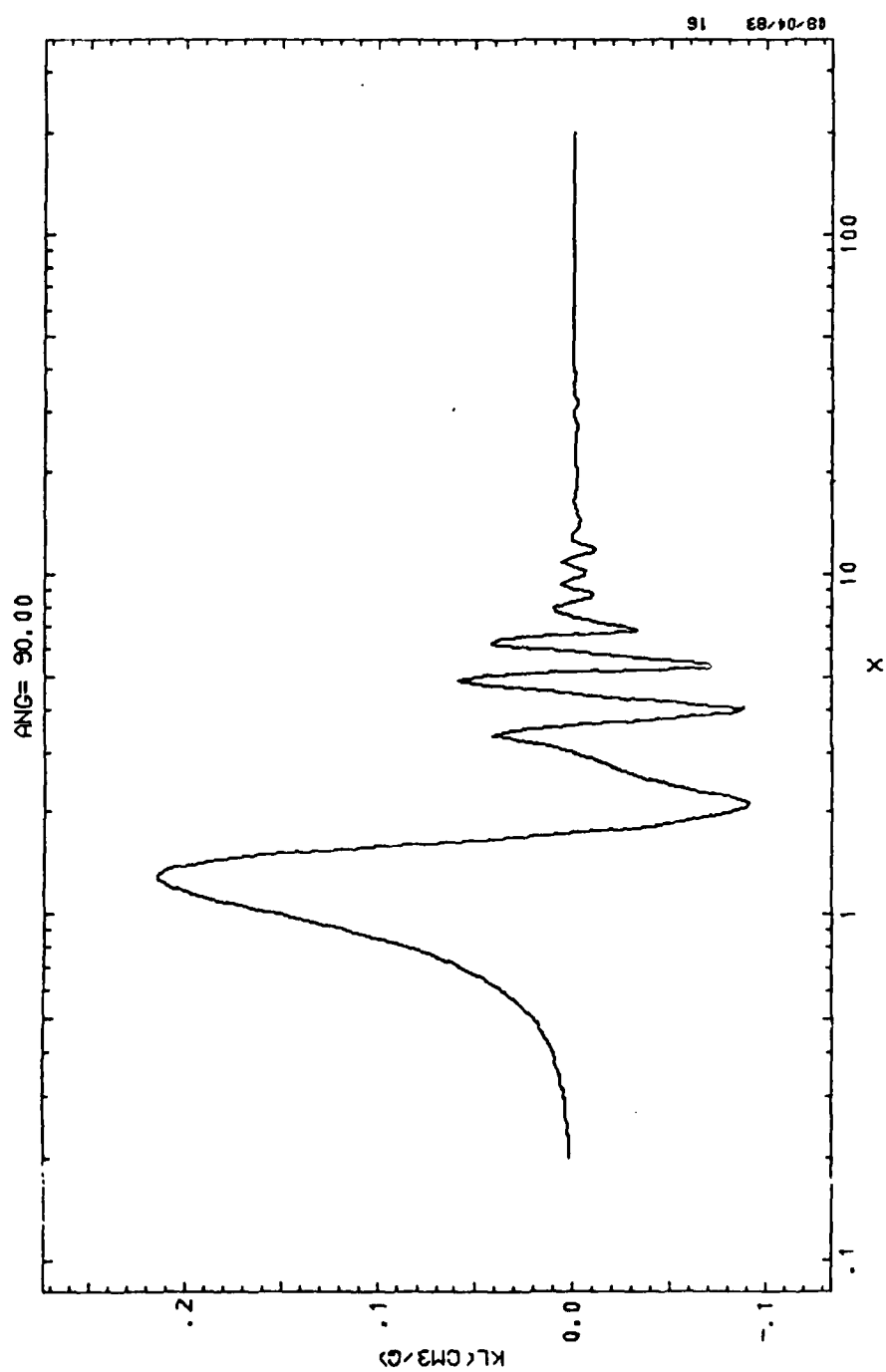


Fig. 22d. Linear Approximation Scattering Kernel ($\theta = 90 \text{ deg}$)

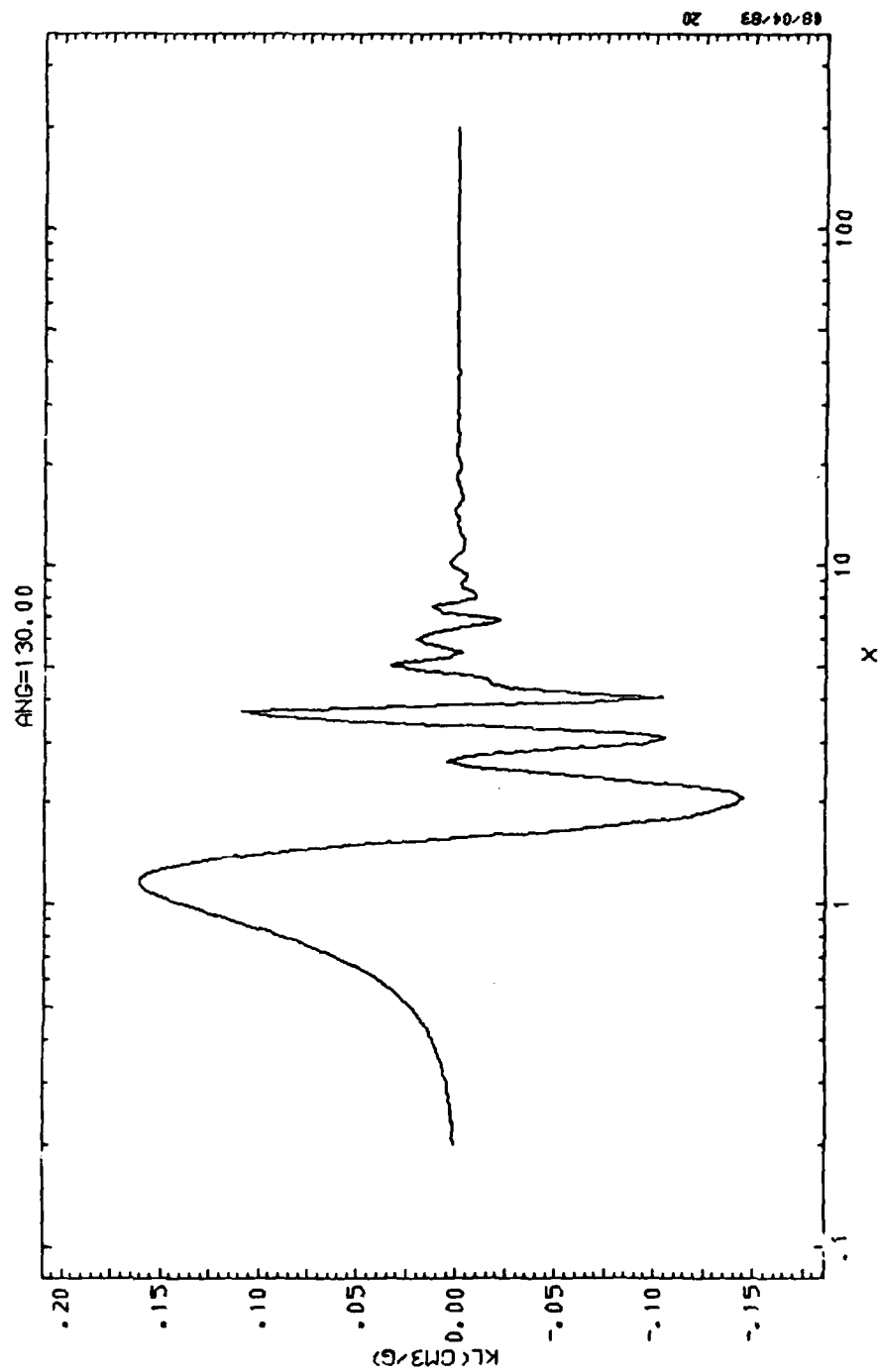


Fig. 22e. Linear Approximation Scattering Kernel ($\theta = 130$ deg)

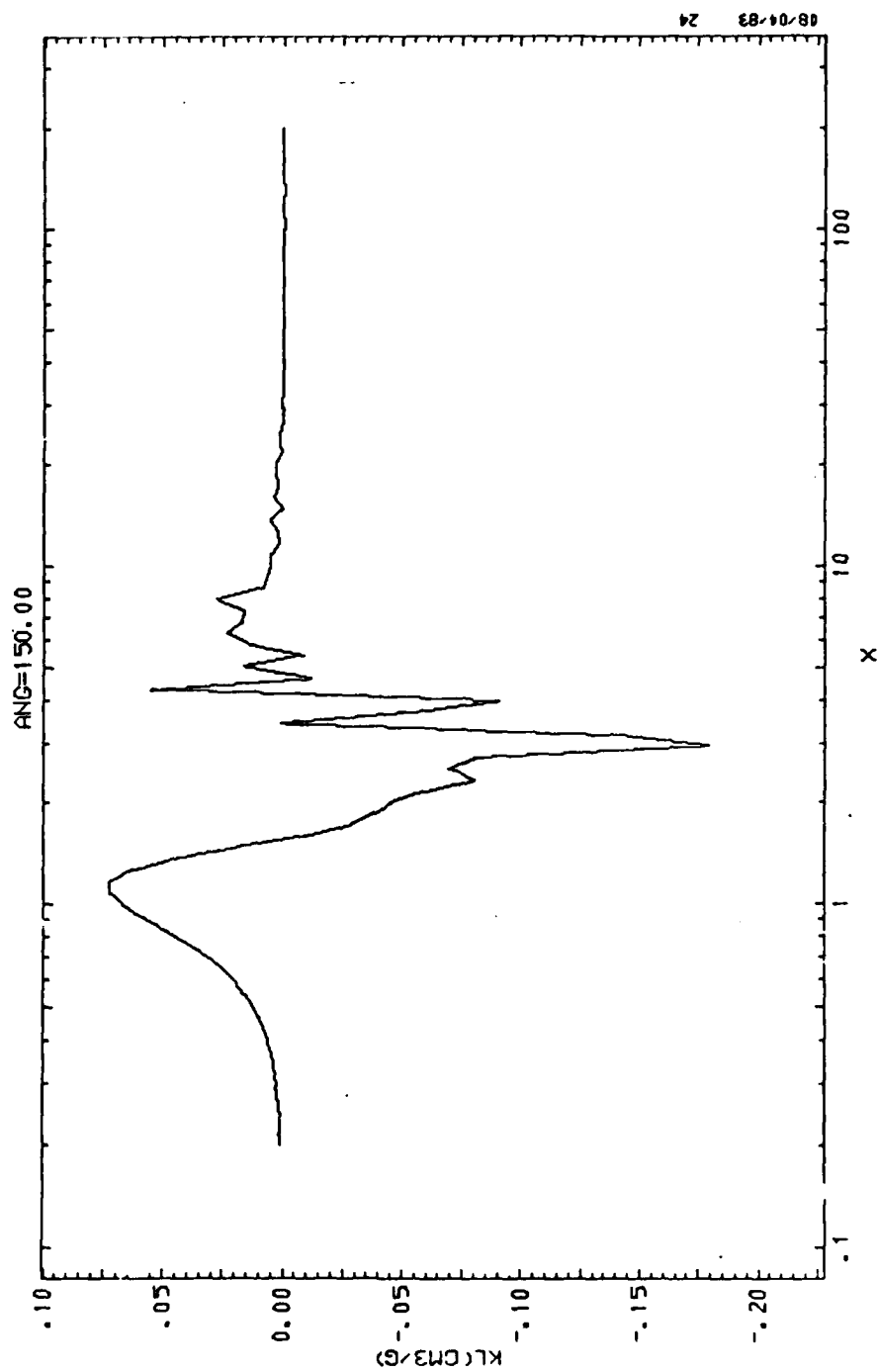


Fig. 22f. Linear Approximation Scattering Kernel ($\theta = 150$ deg)

from zero. With this critereon, it appears that the range is something narrower than $1 < x < 10$. This yields a radii retrieval range of something narrower than $0.1 < a < 1 \mu\text{m}$ at $\lambda = 0.5145 \mu\text{m}$.

3.4 Inversion Algorithm

Despite the lack of a priori knowledge on whether or not the polarization inversion would succeed, it was pursued using a modification of the nonlinear method described in Section 2. To review this method for the purely linear case, assume we have an estimate of $m(x)$, compute the left-hand side of the linear Eq. (8) at angle θ , and find the computed value $g'(\theta)$ to be larger than the measured value $g(\theta)$. Then, Twomey argues, we want to decrease $m(x)$ in those regions of x where $K(\theta, x)$ is largest [this decreases $g'(\theta)$ the most with the least change in $m(x)$]. He suggests the correction (see Fig. 3)

$$m(x) = m(x) \left(1 + \xi \frac{K(\theta, x)}{K^{\max}(\theta)} \right) \quad (33)$$

where $K^{\max}(\theta)$ is the peak of $K(\theta, x)$ and

$$\xi = \frac{g(\theta)}{g'(\theta)} - 1.$$

The correction is applied cumulatively (in a multiplicative sense) for all θ in the angle array. The rational for this procedure follows directly from the (symbolic) derivative

$$\frac{\partial g(\theta)}{\partial m(x)} = K(\theta, x) \Delta x. \quad (34)$$

The corresponding symbolic derivative for the polarization problem follows from Eq. (28) and is

$$\frac{\partial R(\theta)}{\partial m(x)} = \frac{K_1(\theta, x)}{\int_0^\infty K_2(\theta, x) m(x) dx} \left(1 - \frac{R(\theta)}{R(\theta, x)}\right) \Delta x. \quad (35)$$

For the nonlinear problem, then, following Twomey's reasoning, if we have an estimate of $m(x)$, compute the left-hand side of Eq. (26) at angle θ and find the computed value $R'(\theta)$ to be larger than the measured value $R(\theta)$, we should decrease $m(x)$ in those regions of x where $K_1(\theta, x)$ is largest provided $R(\theta, x) > R'(\theta, x)$ in the region; otherwise, $m(x)$ should be increased. An algorithm which accomplishes this for the linear approximation method and takes into consideration the fact the $K'(\theta, x)$ may be negative is

$$m(x) = \begin{cases} m(x) \left(1 + \xi \frac{K'(\theta, x)}{K^{\max}(\theta)}\right) & K'(\theta, x) > 0 \\ m(x) & K'(\theta, x) = 0 \\ m(x) \left(1 - \frac{\xi}{1+\xi} \frac{K'(\theta, x)}{K^{\min}(\theta)}\right) & K'(\theta, x) < 0 \end{cases} \quad (36)$$

where K' is the linear approximation kernel, K^{\max} and K^{\min} are the maximum and minimum values of K' over x (note that K^{\min} is negative), and

$$\xi = \frac{R_e(\theta)}{R_o(\theta)} - 1 \quad (37)$$

where R_e is the experimentally measured ratio and R_0 is the ratio predicted using the guessed-at solution for $m(x)$.

3.5 Test Inversion and Results

A test case was run in order to estimate the retrieval range for a . A constant mass distribution in $0.01 < a < 20 \mu\text{m}$ was assumed and the ratios I_1/I_2 computed for the AFRPL angle array. The results are given in Table 2. These values were then used as input data to the inversion algorithm. The first-guess solution

$$m(a) = C a$$

was used, and iteration was continued until 1% convergence in $m(a)$ was achieved. The results are shown in Fig. 23.

What is sought is the range over which the retrieval algorithm can force the solution to have a flat plateau (see dotted curve of figure). The retrieved distribution does display this feature in the range $0.1 < a < 0.6 \mu\text{m}$ but with large fluctuations superimposed. This range is consistent with the range of x over which the linear kernels are nonzero (see Fig. 22 and $\lambda = 0.5145 \mu\text{m}$). The fact that the level of the plateau is not the same as the true level is a consequence of the inversion not being able to obtain the absolute magnitude of the distribution.

As a further test, an inversion was made for the test conditions used in Section 2. The true distribution is the solid curve of Fig. 24. The simulated ratio data is given in Table 3. A first-guess solution of $m(a) = 1.5 \times 10^{-7} \text{ g/cm}^3\text{-}\mu\text{m}$ was used, and iteration was continued until 1% convergence was achieved. The retrieved distribution is the dashed curve of Fig. 24. Keeping

Table 2. Synthetic Polarization Data Using
Constant Size Distribution.

| $\theta(\text{deg})$ | R |
|----------------------|--------|
| 15 | 1.026 |
| 30 | 1.011 |
| 50 | 0.9536 |
| 90 | 0.7458 |
| 130 | 0.6121 |
| 150 | 0.6909 |

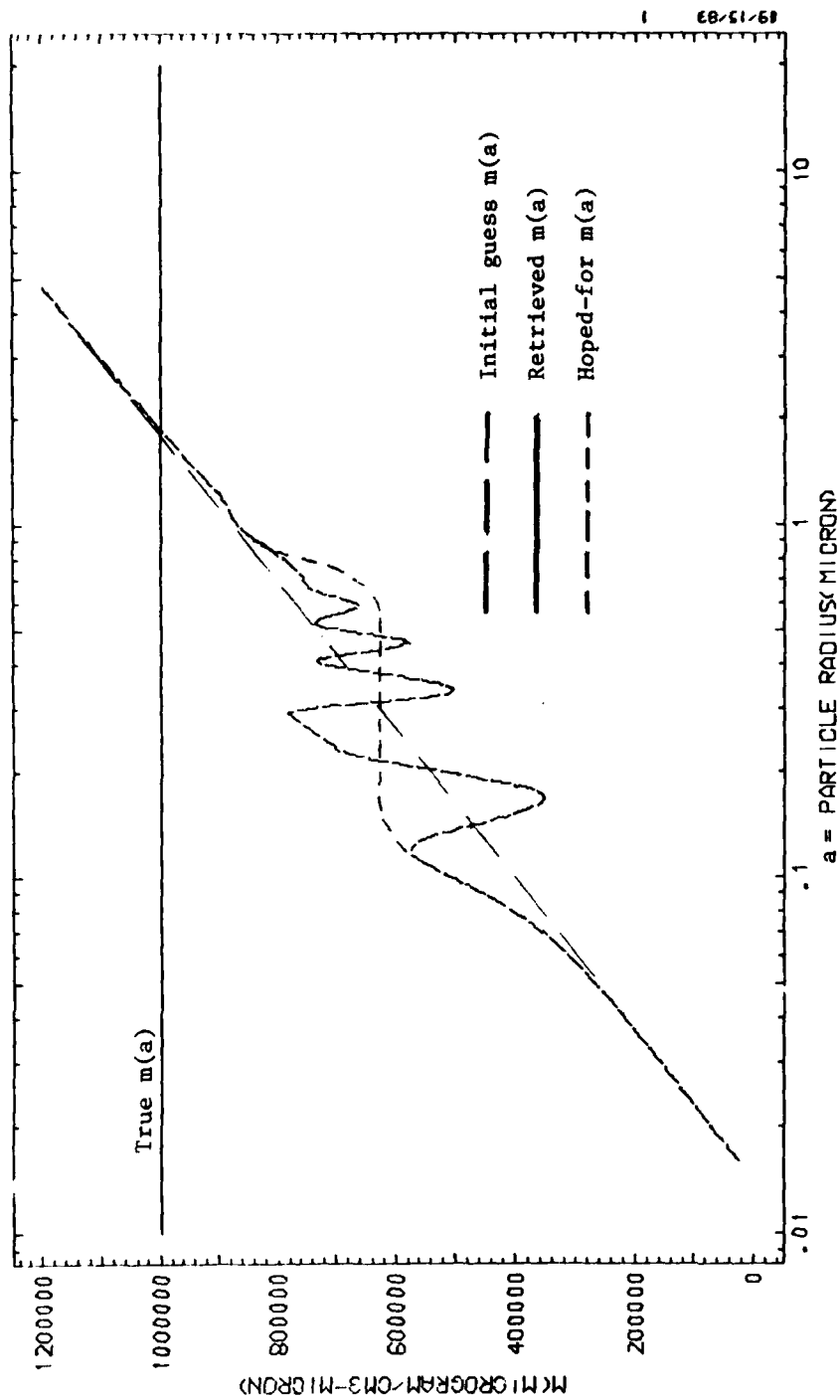


Fig. 23. Size Distribution Retrieval for Uniform Size Distribution

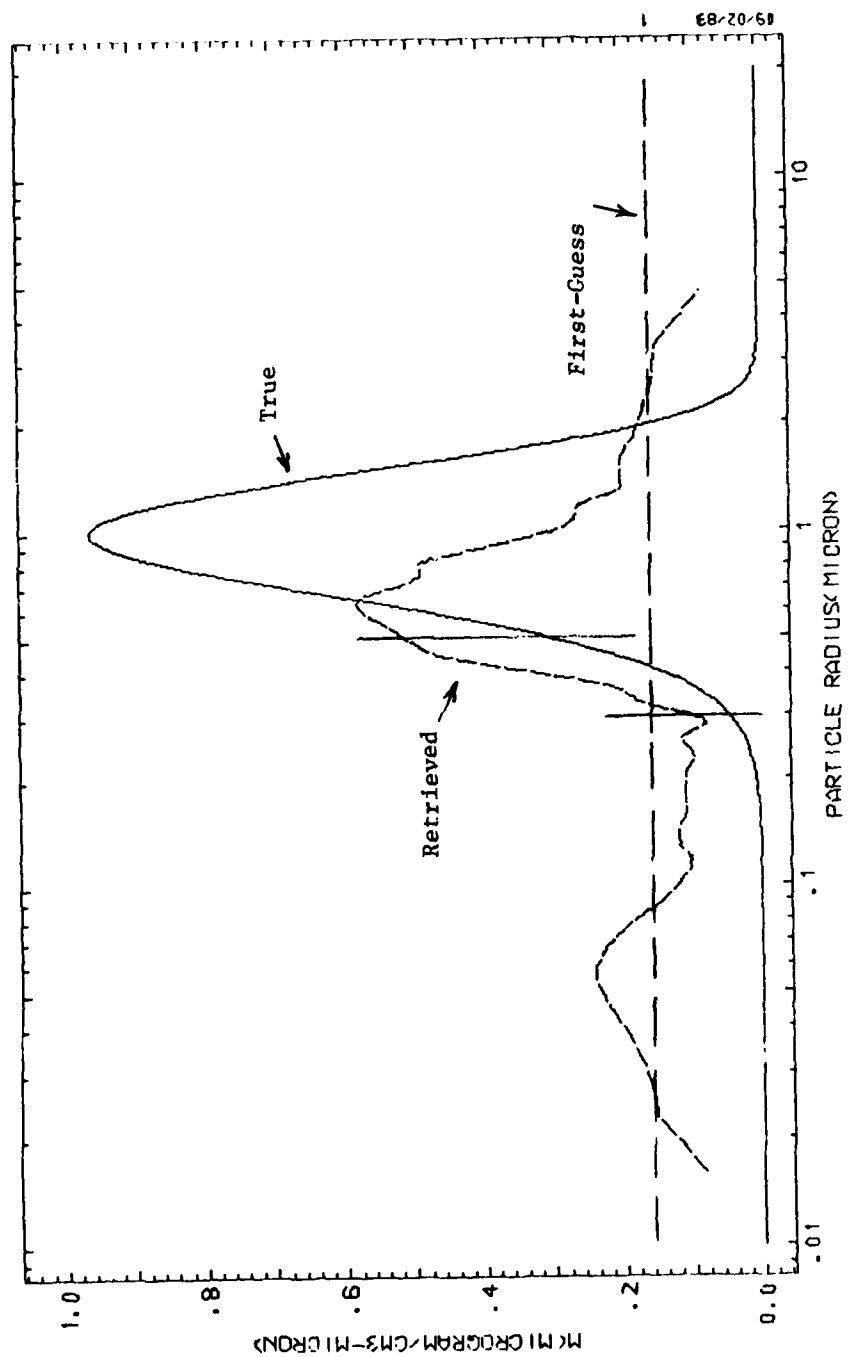


Fig. 24a. Size Distribution Retrieval for Size Distribution of Fig. 4 (Linear Plot)

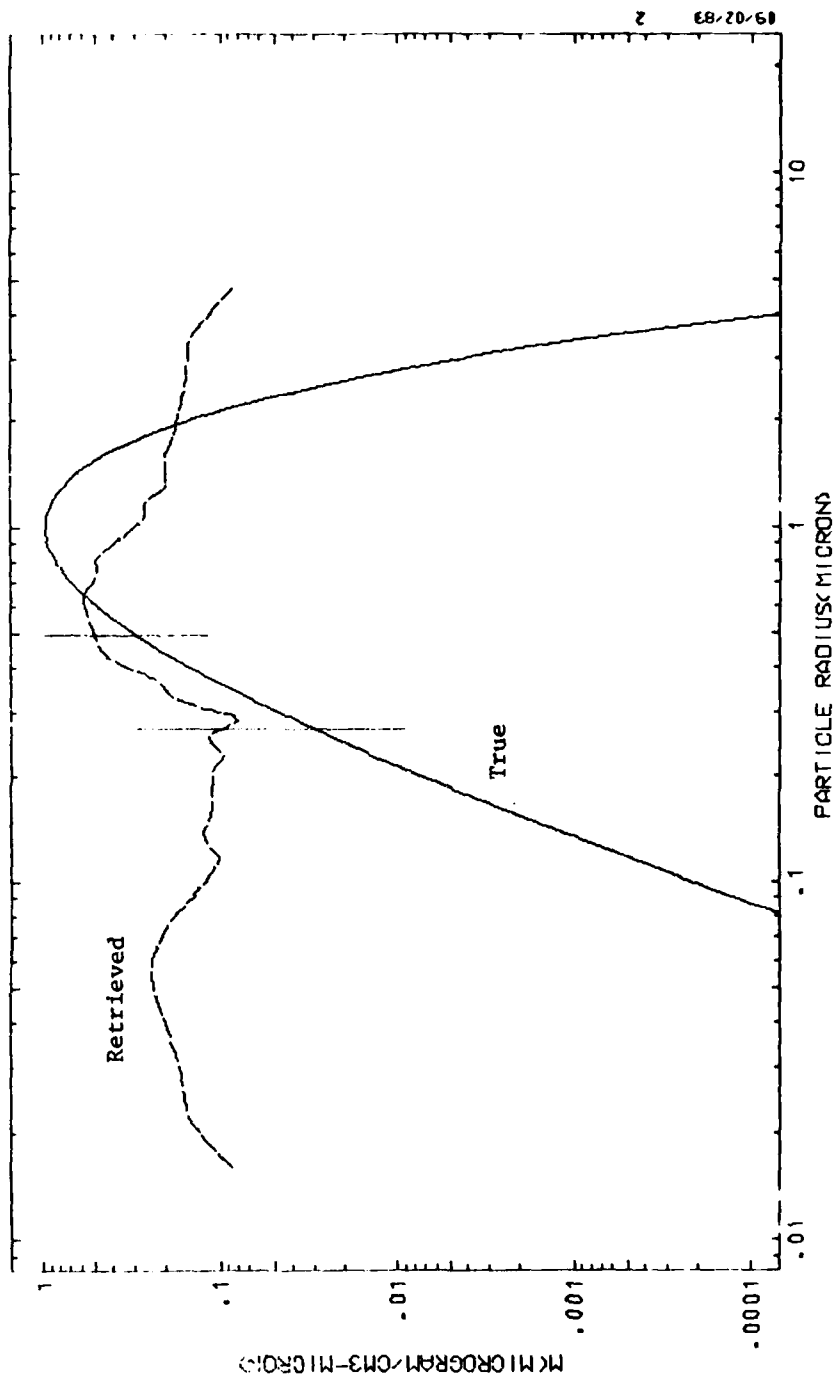


Fig. 24b. Size Distribution Retrieval for Size Distribution of Fig. 4 (Log Plot)

Table 3. Synthetic Polarization Data Using
Size Distribution of Fig. 4.

| $\theta(\text{deg})$ | R |
|----------------------|--------|
| 15 | 1.027 |
| 30 | 1.085 |
| 50 | 0.9690 |
| 90 | 0.6043 |
| 130 | 0.5580 |
| 150 | 1.091 |

in mind that we are looking for regions where the retrieved distribution has the same shape as the true distribution and not necessarily the same value, we find that the only region in which any reasonable retrieval is obtained is in $0.3 \leq a \leq 0.5 \mu\text{m}$, a pitifully small range.

In summary, the most information on particle size distribution that can be obtained from the AFRPL polarization/scattering data is the shape of the distribution in the size range $0.3 \leq a \leq 0.5 \mu\text{m}$, and this assumes the availability of perfectly accurate data. Although the appropriate calculations have not been done it can reasonably be predicted on the basis of much past experience, that if the experimental errors of the AFRPL data are propagated through the inversion, no information on the size distribution can be obtained.

4. TRANSMISSOMETER DIAGNOSTIC FOR MEAN RADIUS

4.1 Introduction

Ariessohn, Self, and Eustis (Ref. 18) describe a two-color transmission measurement technique for determining a particular mean size (the volume-to-surface mean radius) and total mass loading of particles in a two-phase combustion flow. Their method is essentially an extension to absorbing particles of a method devised by Dobbins and Jizmagian (Refs. 19 and 20) for nonabsorbing particles. The use of transmission measurements at two wavelengths in this method allows for the simultaneous determination of the volume-to-surface mean radius and the total mass loading. If the total mass loading is known, the method can be simplified to a one-color diagnostic for obtaining just the volume-to-surface mean diameter. The significant feature of these one- or two-color diagnostics is that ignorance of the actual size distribution of the particles or their complex index of refraction (within limits) causes only a relatively small error in the value of the retrieved results.

In this section, an assessment is made of the applicability of these methods to the retrieval of the volume-to-surface mean particle size and total mass loading in two-phase, low-visibility propellant, solid tactical rocket motor plumes. Only the single-color diagnostic was considered to the point of actually developing a working diagnostic for analysis of AFRPL data. This

18. Ariessohn et al., *Applied Optics* 19, 3775 (1980).

19. Dobbins and Jizmagian, *J. Opt. Soc. Amer.* 56 1345 (1966).

20. Dobbins and Jizmagian, *J. Opt. Soc. Amer.* 56, 1351 (1966).

diagnostic is treated in Section 4.3. An outline of a procedure for developing a two-color diagnostic is present in Section 4.3. Both of these diagnostics are applicable only to the case where transmission data are obtained for a single line of sight through a full diameter of the plume. As such, the retrieval particle radius reflects some average of the particle radius over the cross sectional area of the plume at the axial station where the measurements are made. In principle, these diagnostics could be extended to transmission measurements made in a lateral scan across the plume so that, in conjunction with an Abel inversion, the radial profile of mean particle radius could be retrieved.

4.2 Single-Color Diagnostic

In this section, a review of the single-color method for a fixed line of sight is given, and the retrieval error in the volume-to-surface mean ratio for Al_2O_3 particles caused by ignorance of the actual size distribution and index of refraction is determined. The basic one-color transmission method is described in Section 4.2.1. Error introduced by ignorance of the size distribution is considered in Sections 4.2.2 and 4.2.3 and by ignorance of the complex index of refraction in Section 4.2.4. The final retrieval and error results are presented in Section 4.2.5.

4.2.1 Basic Retrieval Method

The extinction of a well-collimated beam of light traversing a uniform region of suspended particles is governed by the equation

$$- \ln \tau = L \int_0^{\infty} \pi a^2 Q_e(\lambda, a) n(a) da \quad (38)$$

where τ is the transmittance, L is the path length, a is a measure of particle size, $n(a)$ is the particle size distribution function, $Q_e(\lambda, a)$ is the total extinction efficiency (scattering plus absorption), and λ is the wavelength of the radiation. In the present application, the particles are assumed to be homogeneous and spherical with a complex index of refraction $m(\lambda) = n(\lambda) - i \kappa(\lambda)$. The medium in which the particles are suspended is assumed to have an index $m_0 = 1 - i(0)$. The size parameter a is taken as the particle radius.

Define the mean extinction efficiency $\bar{Q}(\lambda)$, the total mass loading C_m and the volume-to-surface mean radius a_{32} , respectively, by

$$\bar{Q}(\lambda) = \frac{\int_0^{\infty} a^2 Q_e(\lambda, a) n(a) da}{\int_0^{\infty} a^2 n(a) da} \quad (39)$$

$$C_m = \int_0^{\infty} \left(d \frac{4}{3} \pi a^3 \right) n(a) da \quad (40)$$

and

$$a_{32} = \frac{\int_0^{\infty} a^3 n(a) da}{\int_0^{\infty} a^2 n(a) da} = \frac{\overline{a^3}}{\overline{a^2}} \quad (41)$$

where d is the bulk density of the particle material. Then, the transmission equation may be written as

$$-\ln \tau = \frac{3L}{4d} C_m \frac{\bar{Q}(\lambda)}{a_{32}} \quad (42)$$

Equation (42) provides a means for obtaining a first-order estimate of particle size if C_m is assumed to be known. If the size distribution is assumed to be monodisperse at particle radius a_{32} then $\bar{Q}(\lambda) = Q_e(\lambda, a_{32})$ and $\bar{Q}(\lambda)/a_{32}$ can be readily calculated using standard Mie scattering algorithms as a function of a_{32} . An example plot is shown in Fig. 25 for $n = 1.75$ and $\kappa = 0$. Rather than a_{32} , the result has been prepared using the independent variable

$$\rho_{32} = 2(n-1) x_{32} \quad (43)$$

where

$$x_{32} = \frac{2\pi a_{32}}{\lambda} \quad (44)$$

is the so-called dimensionless size parameter. The reason for using ρ_{32} as the independent variable is discussed later.

From a measurement of τ and knowledge of C_m (and L), Eq. (42) can be used to obtain an experimental value of \bar{Q}/ρ_{32} which in turn can be used with Fig. (25) to infer two values of ρ_{32} (assuming the measured value of \bar{Q}/ρ_{32} falls below the peak of Fig. (25)). The ambiguity of the result can be removed by several methods. One method is simply by having prior knowledge of the range of particle sizes in the plume. The currently employed AFKPL method is to use the polarization results at 90 deg obtained in the multiangle polarization experiment to show that the lower inferred particle size can be deleted (Ref. 14). In the second of the Dobbins and Jizmagian papers (Ref. 20), a means for removing the ambiguity by making transmission measurements at a second wavelength is discussed.

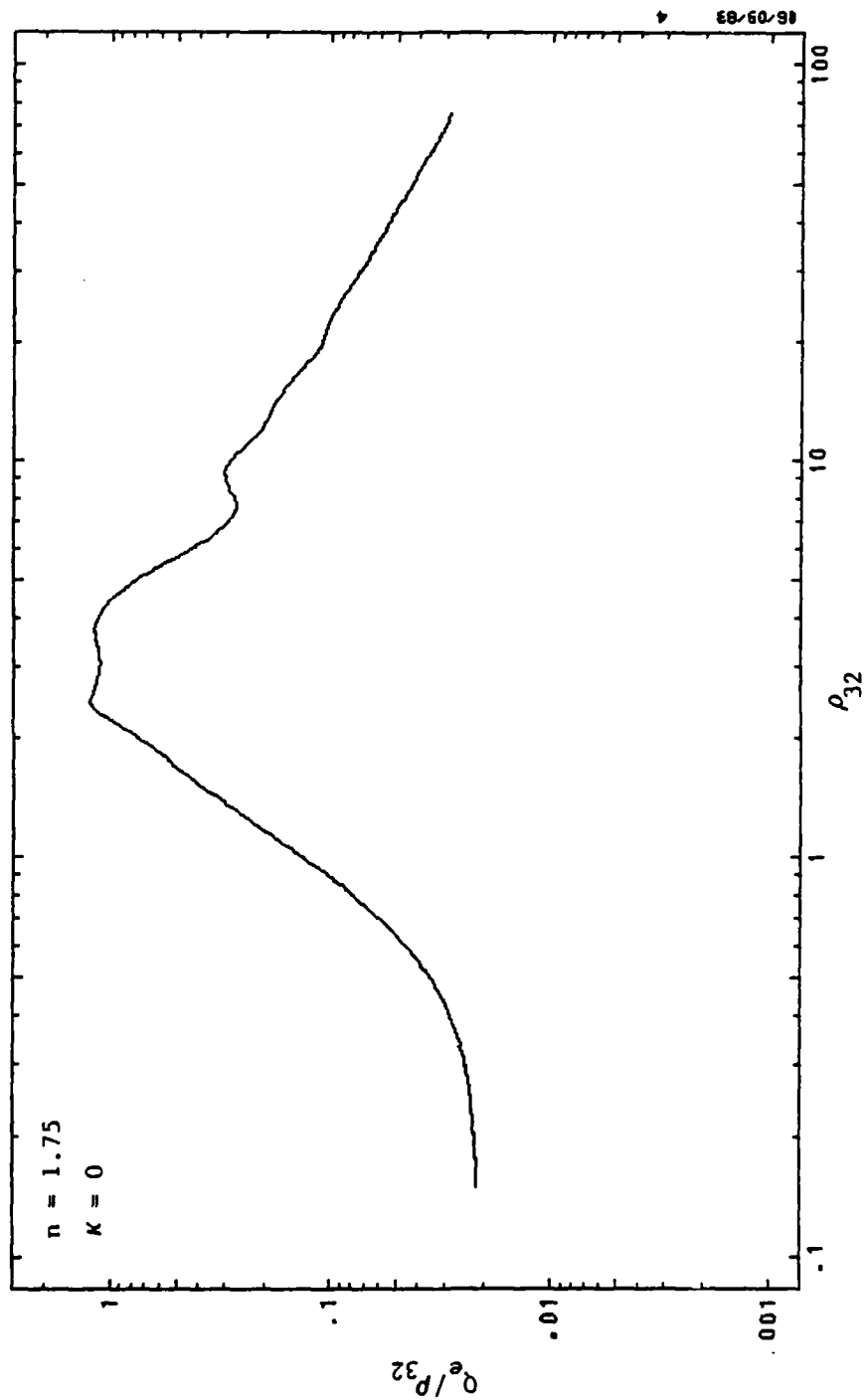


Fig. 25. Extinction Efficiency for Monodispersion at $\bar{a} = \bar{a}_{32}$

As an example application, consider the two measurements made on Al_2O_3 by McCay et al. (Ref. 14). From their Table I

$$\tau = 0.88 \quad C_m = 5.5 \times 10^{-7} \text{ g/cm}^3$$

$$\tau = 0.87 \quad C_m = 1.0 \times 10^{-6} \text{ g/cm}^3$$

$$L = 10 \text{ cm} \quad \lambda = 0.5145 \text{ } \mu\text{m}$$

From these data, one infers (using $d = 3.7 \text{ g/cm}^3$)

$$Q/a_{32} = \begin{cases} 11.5 \text{ } \mu\text{m}^{-1} \\ 6.9 \text{ } \mu\text{m}^{-1} \end{cases}$$

and, using Fig. 25 and Eqs. (43) and (44)

$$a_{32} = \begin{cases} 0.11 \text{ or } 0.30 \text{ } \mu\text{m} \\ 0.09 \text{ or } 0.34 \text{ } \mu\text{m} \end{cases}$$

The higher of the retrieved radii reproduce the values reported in Ref. 14. As a preview to section 4.2.4, it should be noted that these values reproduce the results of Ref. 14 even though different values of the index of refraction were used. Here, $n = 1.75 - (0.1)i$ was employed while in Ref. 14, $n = 1.8 - 0.1(i)$ was used.

4.2.2 Sensitivity to Size Distribution

The usefulness of the preceding approach for other than monodispersions follows from the observation by Dobbins and Jizmagian (Ref. 20) that, for a fixed value of a_{32} , the function $\bar{Q}(\lambda)/a_{32}$ is very insensitive to the size

distribution of particles. Thus, if a measurement of τ is made, and if the total mass loading is known, a determination of $\bar{Q}(\lambda)/a_{32}$ can be made, and from this result, a valid determination of a_{32} follows regardless of the size distribution of the particles.

The accuracy of retrieval using this method was investigated by computing $Q(\lambda)/a_{32}$ for the range of all possible unimodal and bimodal rectangular size distributions possessing a fixed value of a_{32} . Although these distributions are not realistic in shape, they provide the degree of variation required and allow easier mathematical manipulation than the more usually employed "realistic" distributions. The unimodal distribution is

$$n(a) = N f(a) \quad (45)$$

where $f(a)$ is the normalized function

$$f(a) = \begin{cases} 0 & a < a_L \\ 1/(a_u - a_L) & a_L \leq a \leq a_u \\ 0 & a > a_u \end{cases} \quad (46)$$

a_L and a_u are, respectively, the lower and upper bounds of the distribution. The moments of the distribution are

$$\overline{a^n} = \int_{a_L}^{a_u} a^n f(a) da = \frac{1}{n+1} \frac{a_u^{n+1} - a_L^{n+1}}{a_u - a_L} \quad (47)$$

The mean radius and mean volume-to-surface radius are thus

$$\bar{a} = \frac{1}{2} \frac{a_u^2 - a_L^2}{a_u - a_L} = \frac{1}{2} (a_u + a_L) \quad (48)$$

AD-A145 353

CONSIDERATIONS ON THE RETRIEVAL OF PLUME PARTICLE
PROPERTIES FROM THE AFR..(U) AEROSPACE CORP EL SEGUNDO
CA S J YOUNG AUG 84 TR-0084(4623-02)-2 AFRPL-TR-84-047
F04701-83-C-0084 F/G 20/8

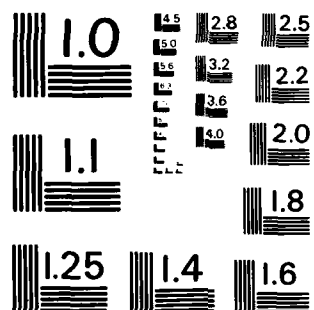
2/2

UNCLASSIFIED

NL

| | | | | | | | | | | | | | | |
|--|--|--|--|--|--|--|--|--|--|--|--|--|--|--|
| | | | | | | | | | | | | | | |
| | | | | | | | | | | | | | | |
| | | | | | | | | | | | | | | |

END
DATE
FILMED
10-84
DTIC



MICROCOPY RESOLUTION TEST CHART
NATIONAL BUREAU OF STANDARDS-1963-A

$$a_{32} = \frac{3}{4} \frac{a_u^4 - a_L^4}{a_u^3 - a_L^3} = \frac{3}{4} \frac{a_u^3 + a_u^2 a_L + a_u a_L^2 + a_L^3}{a_u^2 + a_u a_L + a_L^2} . \quad (49)$$

The use of Eqs. (43) and (47), along with the definitions

$$\eta = a/a_{32}$$

$$\eta_L = a_L/a_{32} \quad (50)$$

$$\eta_u = a_u/a_{32}$$

for scaled radial variables, and

$$x = \frac{2\pi a}{\lambda} \quad (51)$$

$$x_{32} = \frac{2\pi a_{32}}{\lambda}$$

for dimensionless size parameters, transforms Eq. (39) into

$$\bar{Q}(m, x_{32}) = \frac{3}{\eta_u^3 - \eta_L^3} \int_{\eta_L}^{\eta_u} \eta^2 Q_e(m, x_{32}\eta) d\eta . \quad (52)$$

The argument lists of \bar{Q} and Q_e have been changed to reflect the dependence on $m = n - 1/\kappa$ and x_{32} .

The integral in Eq. (52) was evaluated by trapezoidal quadrature to an accuracy of 0.1%. Variation over all possible size distributions with a fixed a_{32} was accomplished by varying the lower bound parameter η_L in steps of 0.1 from 0 to 1. The corresponding upper bound for each lower bound was determined as the solution of the cubic equation [obtained from Eq. (49)]

$$\eta_u^3 + \left(\frac{4}{3} - \eta_L\right) \eta_u^2 + \eta_L \left(\frac{4}{3} - \eta_L\right) \eta_u + \eta_L^2 \left(\frac{4}{3} - \eta_L\right) = 0. \quad (53)$$

As η_L varies from 0 to 1, η_u varies from 4/3 to 1. Thus, the narrowest distribution in the variation is the monodispersion $\eta_L = \eta_u = 1$, and the widest is $\eta_L = 0$, $\eta_u = 4/3$. The evaluation of the integrals in Eq. (52) is somewhat time-consuming. Therefore, the calculations were done once and saved on a computer permanent file. Beside the variation over the 11 values of η_L , calculations were performed for the 41 values of x_{32}

$$x_{32}(i) = (10)^{1/10} x(i-1); i=2, 41; x(1) = 0.1 \quad (54)$$

and the 18 values of index of refraction implied by

$$n = 1.70, 1.75, 1.80$$

$$\kappa = 0, 0.0002, 0.002, 0.02, 0.2, 0.5. \quad (55)$$

A discussion of these index values is given later.

A typical result for the variation of \bar{Q}/a_{32} with size distribution is shown in Fig. 26. Again, the parameter ρ_{32} is used as the independent variable. The middle curve of Fig. 26 is the value of \bar{Q}/ρ_{32} averaged over the 11 size distributions for a fixed $n = 1.75$, $\kappa = 0$. The other two curves are the mean curve plus or minus one standard deviation, σ . The maximum error in \bar{Q}/ρ_{32} occurs at $\rho_{32} \approx 4$ and is of the order 9%.

If the example application made in the last section is reanalyzed with Fig. 26, the inferred radii (upper values) for the two transmission cases are now

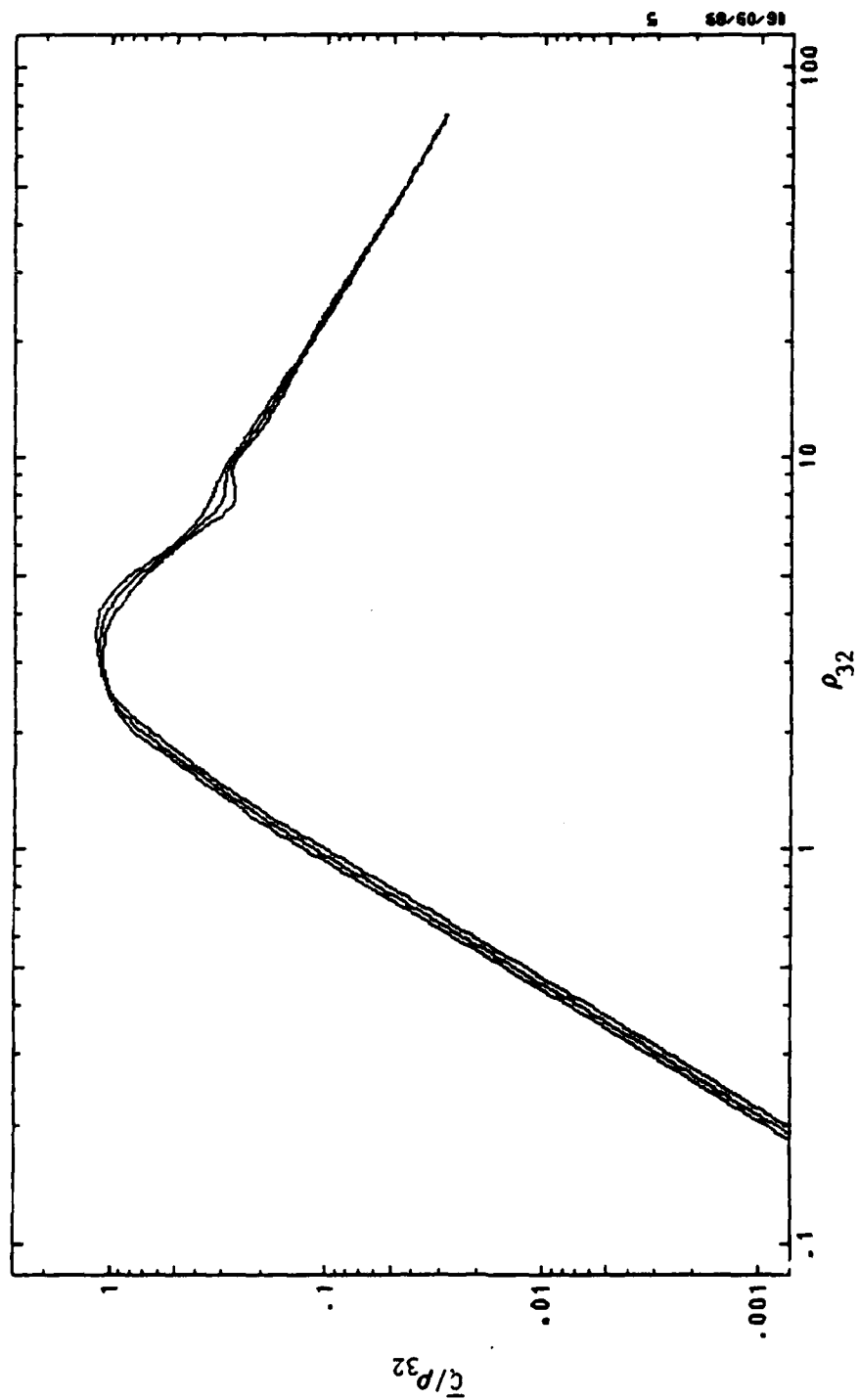


Fig. 26. Retrieval Error Band Caused by Ignorance of Unimodal Size Distribution Function

$$a_{32} = 0.30 \pm .01 \quad \text{for } \tau = 0.88$$

and

$$a_{32} = 0.37 \pm 0.02 \quad \text{for } \tau = 0.87$$

Thus, ignorance of the size distribution has introduced an error of only 3 to 6% in the retrieved radii.

4.2.3 Extension to Bimodal Size Distribution

The preceding analysis was also carried out for a bimodal particle size distribution consisting of two nonoverlapping rectangular size distributions (Fig. 27). The distribution is specified by six parameters (the upper and lower bound and relative concentration of each component). Two constraints of the distribution are normalization

$$C_1 (a_u - a_L) + C_2 (A_u - A_L) = 1 \quad (56)$$

and fixed a_{32} radius

$$a_{32} = \frac{3}{4} \frac{C_1 (a_u^4 - a_L^4) + C_2 (A_u^4 - A_L^4)}{C_1 (a_u^3 - a_L^3) + C_2 (A_u^3 - A_L^3)} \quad (57)$$

These constraints serve to fix two of the size parameters. In order to effect a variation over all possible size distributions, it is necessary to vary only four remaining parameters. Three of these were taken as radial bound ratios

$$0 < R = \frac{A_L}{A_u} < 1 \quad (58)$$

$$0 < \rho = \frac{a_u}{A_u} < R \quad (59)$$

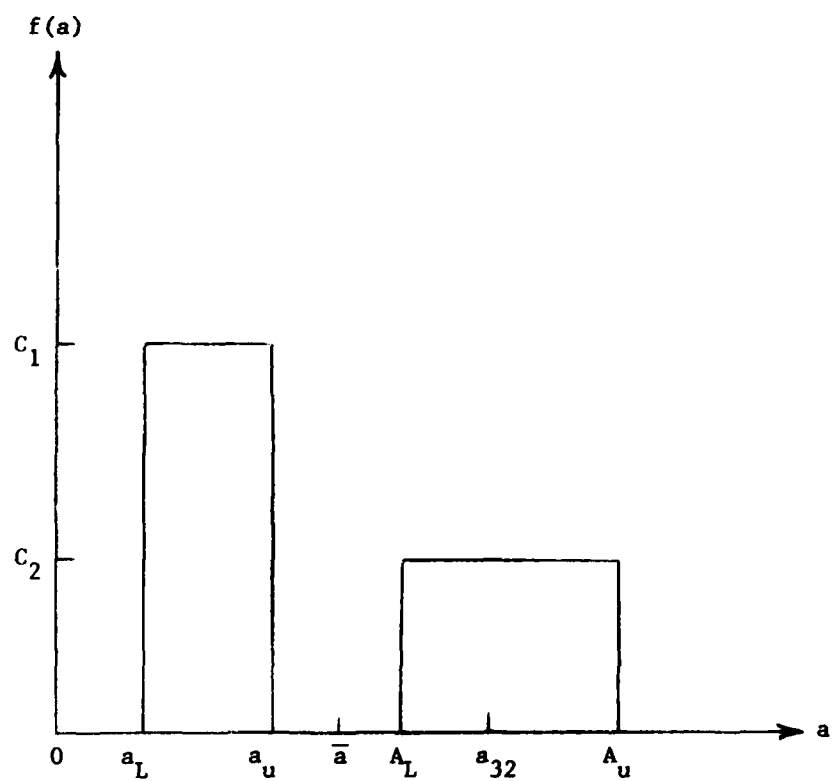


Fig. 27. Bimodal Rectangular Size Distribution

$$0 < r = \frac{a_L}{A_u} < \rho. \quad (60)$$

The fourth variation is the relative concentration in the two modes and is effected by varying C_2 from 0 to its maximum value

$$C_2^{\max} = \frac{1-R^4}{\frac{4}{3} a_{32} (1-R) (1-R^3)}. \quad (61)$$

With C_2 specified, C_1 is given by

$$\frac{C_1}{C_2^{\max}} = \frac{1}{2A} ([B^2 - 4AC]^{1/2} - B) \quad (62)$$

where

$$A = \frac{(\rho^3 - r^3)(\rho - r)}{(1 - R)(1 - R^3)} \quad (63)$$

$$B = \frac{C_2}{C_2^{\max}} \frac{1}{(1-R)(1-R^3)} [(\rho^3 - r^3)(1-R) + (1-R^3)(\rho - r)] - \frac{\rho^4 - r^4}{1-R^4} \quad (64)$$

$$C = \frac{C_2}{C_2^{\max}} \left(\frac{C_2}{C_2^{\max}} - 1 \right). \quad (65)$$

In application, R , ρ and r were varied on the grid $a/A_u = 0, 0.2, 0.4, 0.6, 0.8, 1.0$ and C_2/C_2^{\max} on the grid $0, 0.2, 0.4, 0.6, 0.8, 1.0$. Given the constraints of Eqs. (58) through (60), this amounts to 336 different distributions.

The computation of \bar{Q}/ρ_{32} for 336 size distributions, 18 combinations of n and κ and 41 values of x_{32} would be prohibitively expensive. Fortunately, the desired results can be obtained in terms of \bar{Q} functions computed for the unimodal rectangular size distributions and which are already computed and saved. For the bimodal size distribution, we have

$$\bar{Q} = \frac{1}{\bar{a}^2} \int_0^{\infty} a^2 Q_e [x(a)] f(a) da$$

$$= \frac{C_1 (a_u^3 - a_L^3)}{3 \bar{a}^2} \frac{3}{a_u^3 - a_L^3} \int_{a_L}^{a_u} a^2 Q_e [x(a)] da + \frac{C_2 (A_u^3 - A_L^3)}{3 \bar{a}^2} \frac{3}{A_u^3 - A_L^3} \int_{A_L}^{A_u} a^2 Q_e [x(a)] da \quad (66)$$

where \bar{a}^2 is the mean square radius

$$\bar{a}^2 = \frac{1}{3} [C_1 (a_u^3 - a_L^3) + C_2 (A_u^3 - A_L^3)]. \quad (67)$$

In the first integral, define

$$\eta = \frac{a}{a_{32}^l}, \quad x_{32}^l = \frac{2\pi a_{32}^l}{\lambda}, \quad \eta_u^l = \frac{a_u}{a_{32}^l}, \quad \eta_L^l = \frac{a_L}{a_{32}^l}, \quad (68)$$

$$a_{32}^l = \frac{3}{4} \frac{a_u^4 - a_L^4}{a_u^3 - a_L^3}$$

and in the second, define

$$\eta = \frac{a}{a_{32}^u}, \quad x_{32}^u = \frac{2\pi a_{32}^u}{\lambda}, \quad \eta_u^u = \frac{a_u}{a_{32}^u}, \quad \eta_L^u = \frac{a_L}{a_{32}^u}, \quad (69)$$

$$a_{32}^u = \frac{3}{4} \frac{A_u^4 - A_L^4}{A_u^3 - A_L^3}.$$

Then, Eq. (66) is transformed into

$$\begin{aligned} \bar{Q} = (1 - w) & \frac{3}{(\eta_u^l)^3 - (\eta_L^l)^3} \int_{\eta_L^l}^{\eta_u^l} \eta^2 Q_e(x_{32}^l, \eta) d\eta \\ & + w \frac{3}{(\eta_u^u)^3 - (\eta_L^u)^3} \int_{\eta_L^u}^{\eta_u^u} \eta^2 Q_e(x_{32}^u, \eta) d\eta \end{aligned} \quad (70)$$

where

$$w = \frac{1}{1 + \frac{C_1}{C_2} \frac{(\rho^3 - r^3)}{(1 - R^3)}} \quad (71)$$

From Eq. (52), we see that the quantities in brackets are just the \bar{Q} 's for the unimodal rectangular size distributions. Thus

$$\begin{aligned} \bar{Q}(x_{32}) = (1 - w) & \bar{Q}_r(x_{32}^l, \eta_u^l, \eta_L^l) \\ & + w \bar{Q}_r(x_{32}^u, \eta_u^u, \eta_L^u) \end{aligned} \quad (72)$$

where the subscript r implies unimodal rectangular.

The computation of \bar{Q} in the bimodal size distribution problem consists in calculation $x_{32}^l, \eta_u^l, \eta_L^l, x_{32}^u, \eta_u^u$ and η_L^u and appropriately interpolating on the saved \bar{Q}_r files. The two interpolated \bar{Q}_r values are then weighted as indicated in Eq. (72) and added.

Example results for \bar{Q}/ρ_{32} averaged over the 336 bimodal size distributions are shown in Fig. 28. The middle solid curve is \bar{Q}/ρ_{32} ; the upper and lower solid curves are $\bar{Q}/\rho_{32} \pm \sigma$. The variation over the bimodal size distributions results in a significantly greater σ than did the averaging over the

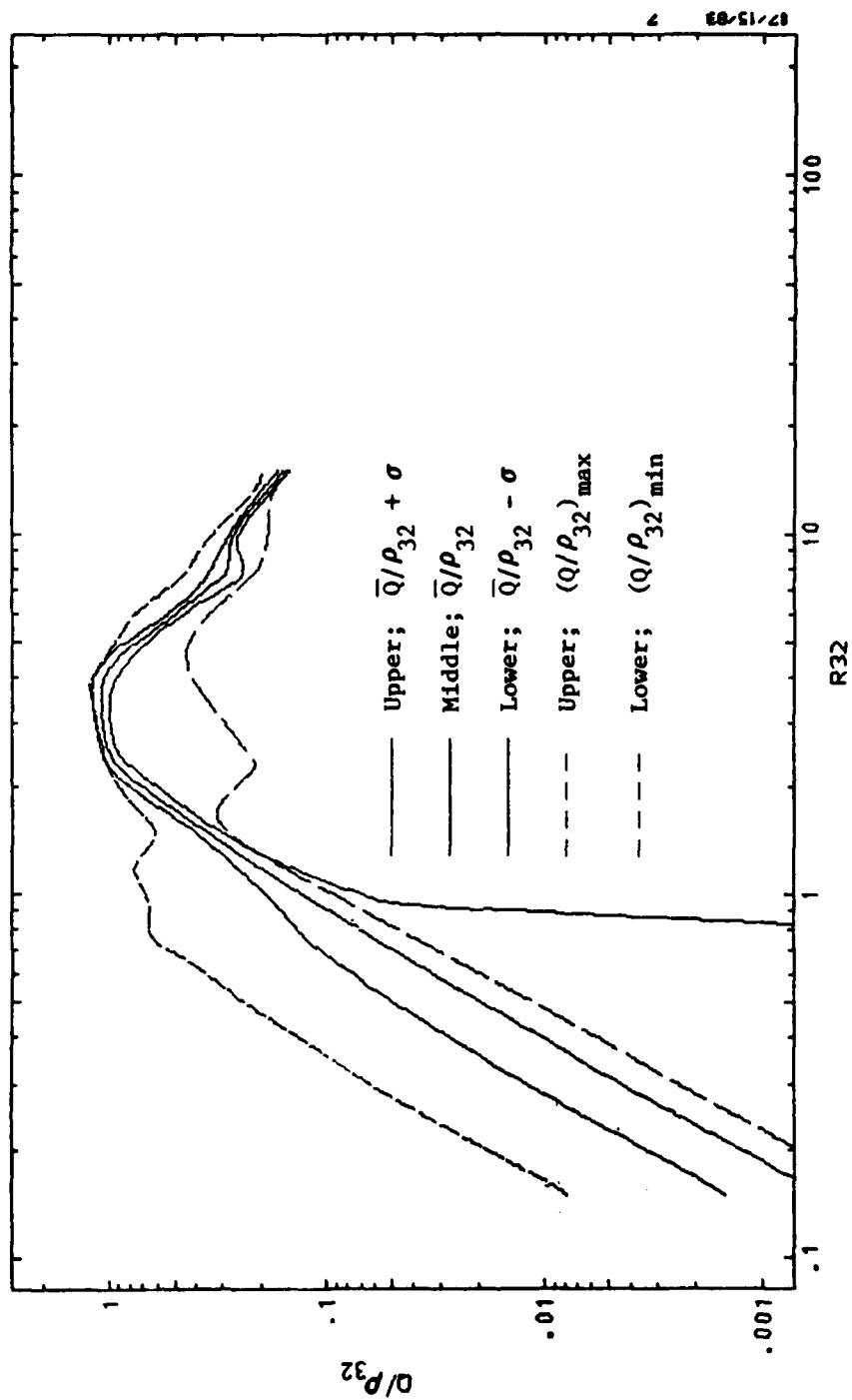
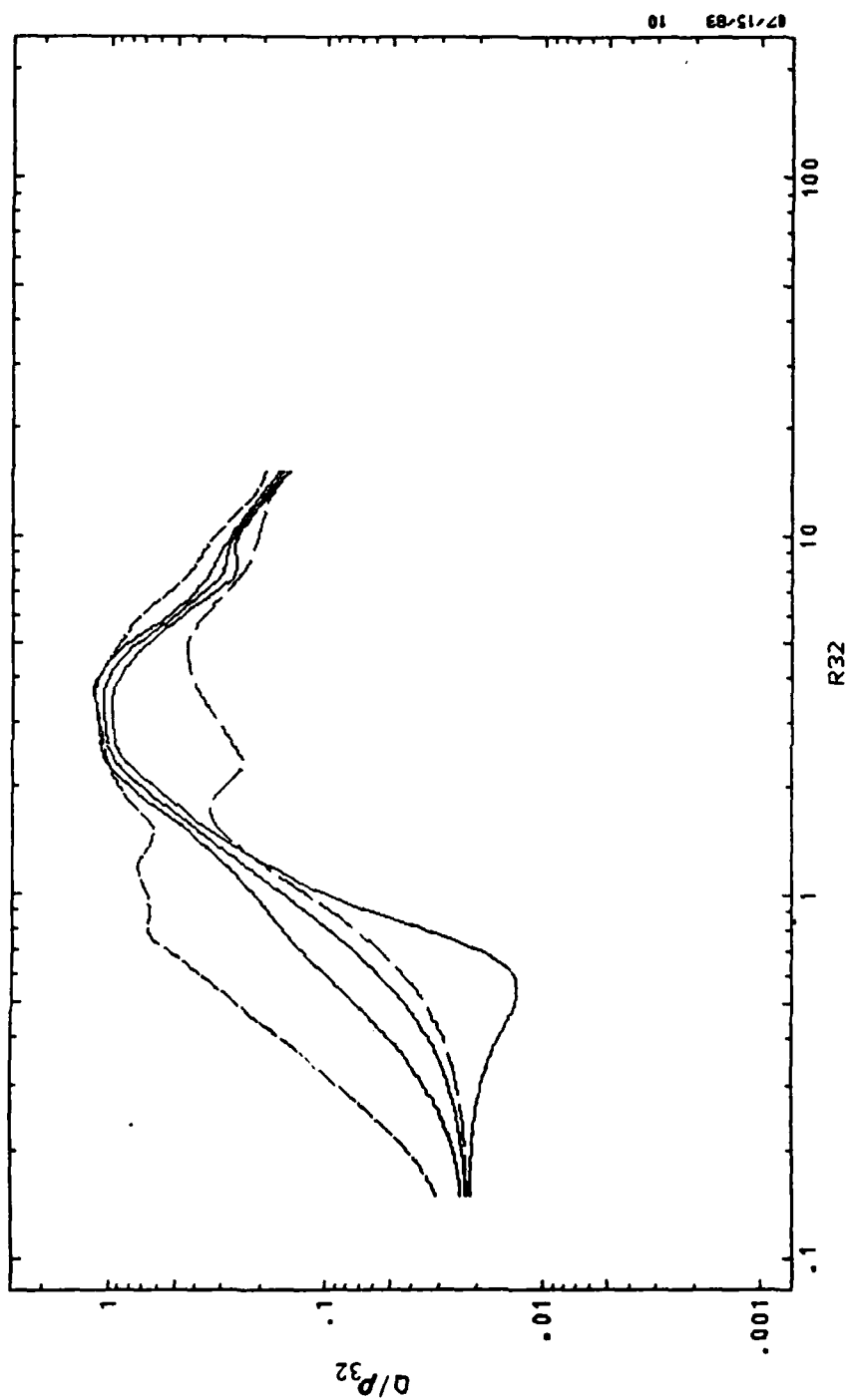
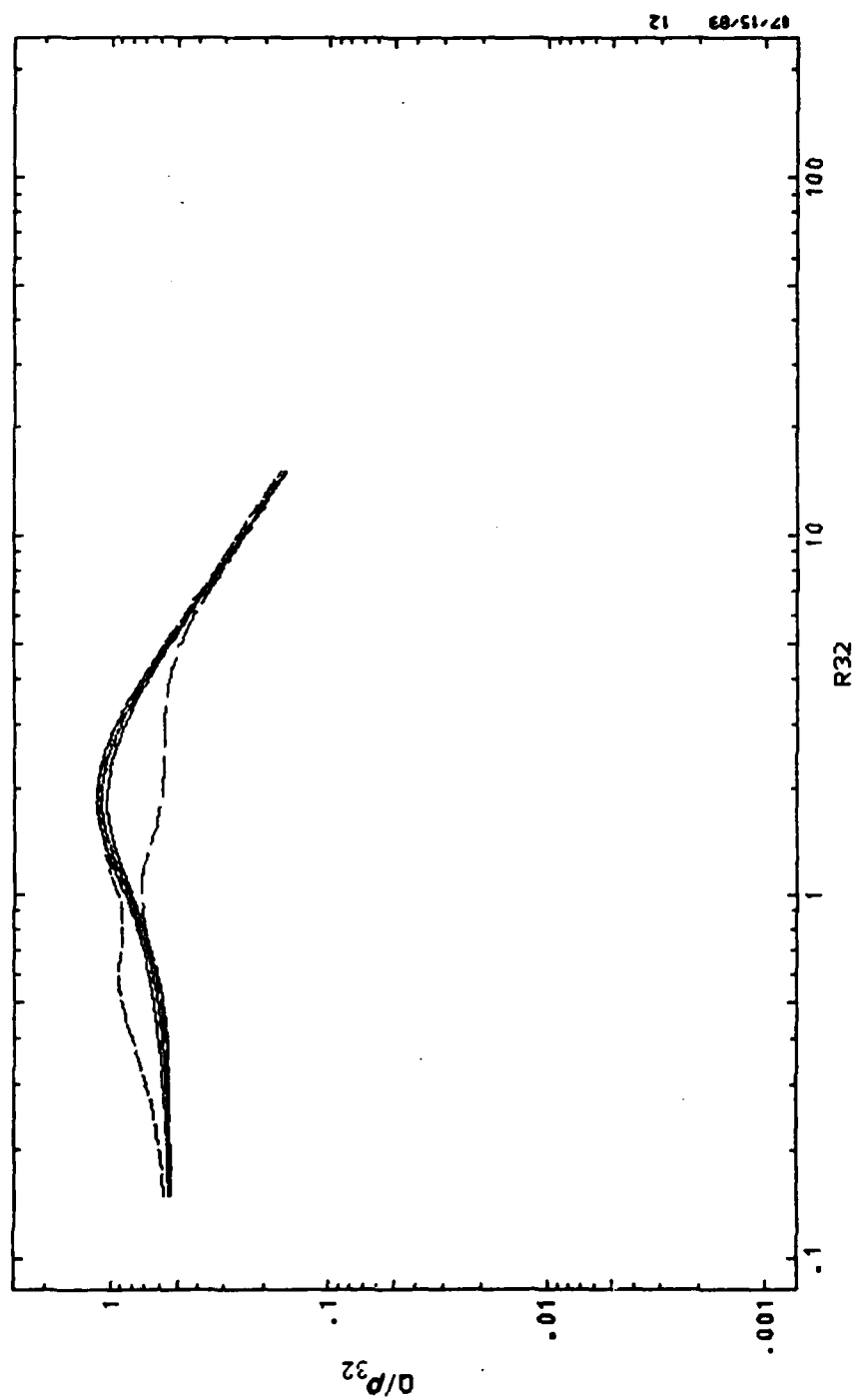


Fig. 28a. Mean Scattering Efficiency Results for Bimodal Distribution



$N = 1.750$ $K = 2.00E-02$

Fig. 28b. Mean Scattering Efficiency Results for Bimodal Distribution



$N = 1.750$ $K = 5.00E-01$

Fig. 28c. Mean Scattering Efficiency Results for Bimodal Distribution

unimodal distribution. In fact, for $\rho_{32} < 0.8$ and small κ , σ is larger than the computed \bar{Q}/ρ_{32} , which results in a negative lower bound. In such cases, the lower bound is better taken as the actual minimum \bar{Q}/ρ_{32} that occurs in the variation. This is shown in the figures by the lower dashed curve. The upper dashed curve is the maximum \bar{Q}/ρ_{32} occurring in the variation.

For fixed n and κ , the results presented so far indicated the degree of error to be expected given complete ignorance of the particle size distribution (except to the extent that it is assumed to be a unimodal or bimodal rectangular distribution). Note that the standard deviation σ has been used to measure the uncertainty in \bar{Q}/ρ_{32} . This is the "reasonable" choice. If desired, the analysis could be carried out for the "pessimistic" worst case condition of using the minimum and maximum values of Q/ρ_{32} that occur in the variation with r (and they do not necessarily occur at $r = 0$ and 1).

4.2.4 Sensitivity to Index of Refraction

In order to assess the sensitivity of the retrieval diagnostic to uncertainty in the complex index of refraction, it is necessary to set some bounds on the real and imaginary parts of the index. From the data compilation of the SIRRIM report (Ref. 10) and IR Handbook (Ref. 21), the range $n = 1.70$ to 1.80 been selected as representative of the real part of the index for Al_2O_3 for all of the visible and near IR spectral regions and temperatures up to the melting point of Al_2O_3 . The range of the imaginary part was selected

-
21. The Infrared Handbook, Wolf and Zissis, editors, Office of Naval Research, Department of the Navy, Washington D.C., 1978.
 22. W. L. Konopka et al., Infrared Optical Properties of Al_2O_3 Rocket Particles, preprint, Grumman Aerospace Corporation Bethpage, New York, 1983.

primarily from the data presented by Konopka et al. (Ref. 22) on their recent investigations of shock-tube heated rocket plume Al_2O_3 . Although $\kappa \sim 10^{-4}$ to 10^{-7} for pure Al_2O_3 , their findings indicate that κ may be as high as 0.01 for Al_2O_3 actually occurring in plumes. The work here uses values up to $\kappa = 0.5$ although $\kappa = 0.02$ is suggested as a more realistic upper bound on the parameter.

The variation with n in \bar{Q}/ρ_{32} for a monodisperse distribution is shown in Fig. 29 for $\kappa = 0$. The variation appears much smaller than similar variations shown by Ariessohn et al. (Ref. 18) because the scaled variable ρ_{32} has been used rather than a_{32} . The effect of using ρ_{32} in place of x_{32} is that most of the variation in the dependent variable \bar{Q}/ρ with n has been transferred into the independent variable. The variation with κ for $n = 1.75$ is shown in Fig. 30. Significant variations introduced by ignorance in both n and κ are limited to the lower branch of the \bar{Q}/ρ curves below $\rho_{32} = 3$. Of the two, ignorance in κ causes the most variation, particularly for $\rho_{32} < 1.0$.

In order to arrive at a retrieval error estimate that reflects ignorance of index of refraction as well as ignorance of size distribution, the calculations of Section 4.2.3 were repeated for all 18 combinations of $n = 1.70, 1.75, 1.80$ and $\kappa = 0, 2 \times 10^{-4}, 2 \times 10^{-3}, 2 \times 10^{-2}, 0.2$ and 0.5 . As mentioned before, the latter two values of κ are probably excessively high for Al_2O_3 . Even with carbon contamination, the value 0.02 is a reasonable upper bound. The following analysis was carried out using both $\kappa_{\text{max}} = 0.02$ and 0.50 . The 36 resulting functions $\bar{Q}/\rho_{32} + \sigma$ and $\bar{Q}/\rho_{32} - \sigma$ were plotted on a common ρ axis, and the upper and lower envelope of the curves used to define the final bounds for \bar{Q}/ρ_{32} . The results obtained using the unimodal distribution are shown in Fig. 31a and the results using the bimodal distribution in Fig. 31b.

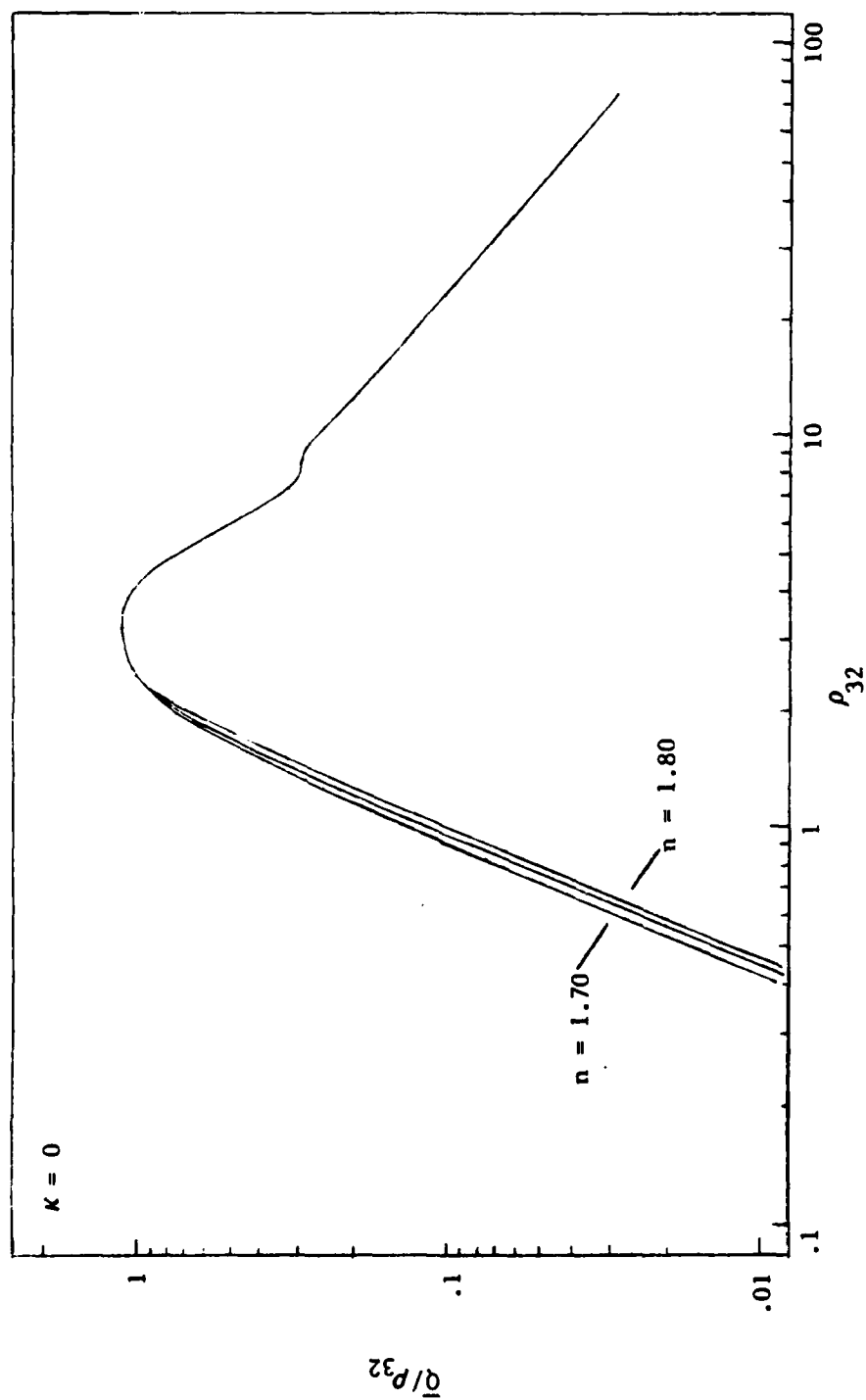


Fig. 29. Variation of Extinction Efficiency with n

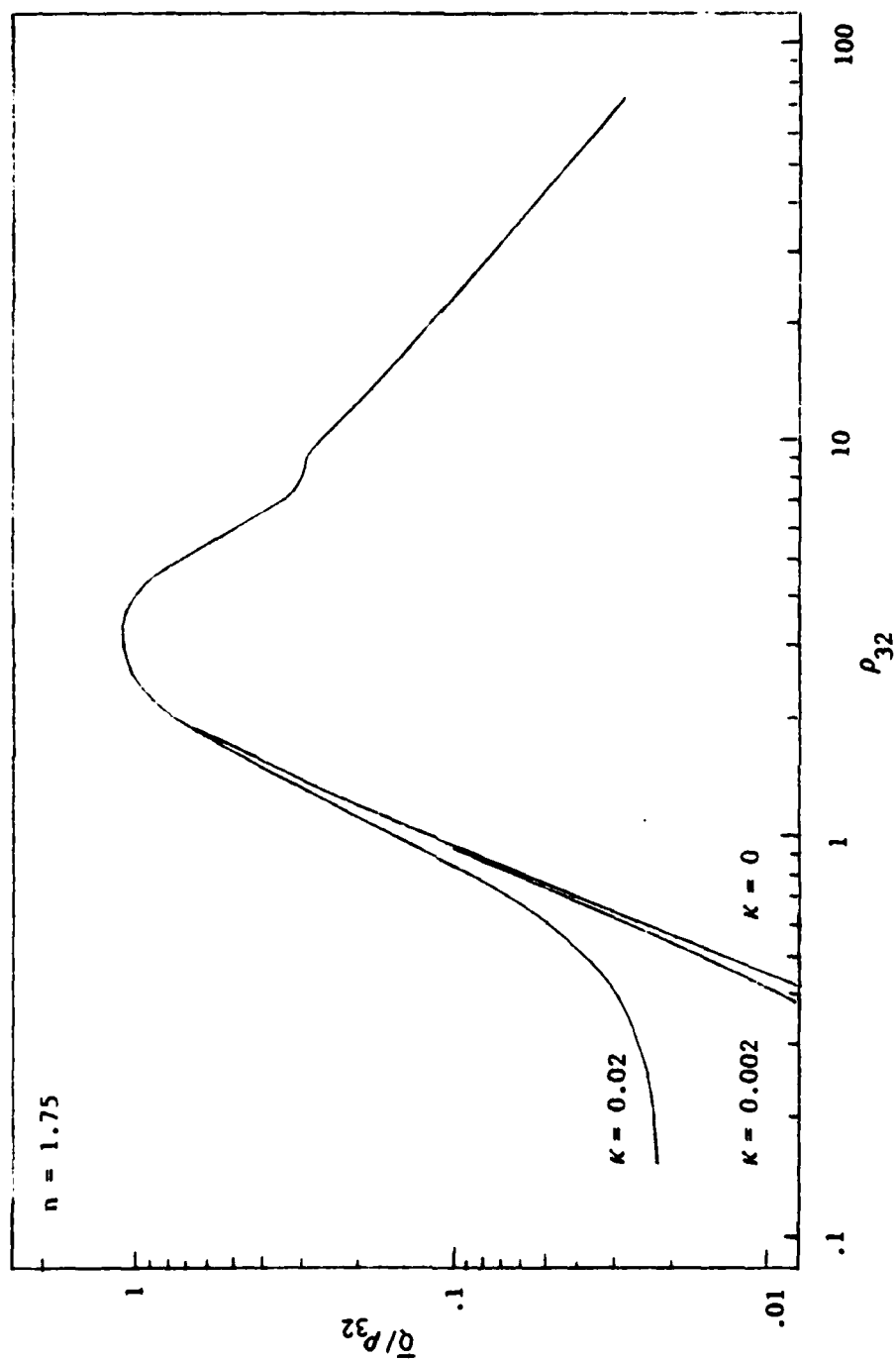


Fig. 30. Variation of Extinction Efficiency with K

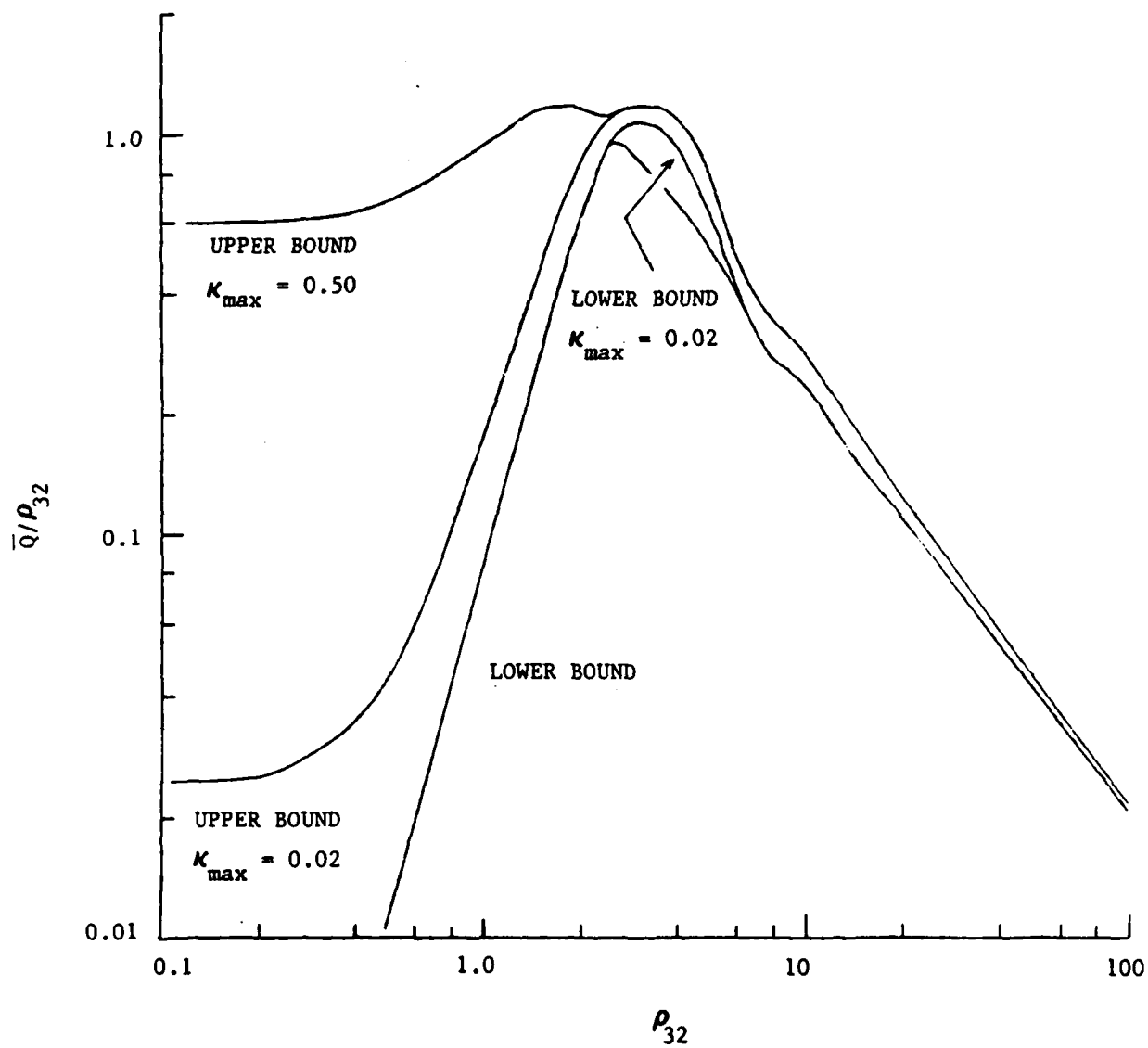


Fig. 31a. Retrieval Error Bound Caused by Ignorance of Size Distribution Function and Index of Refraction (Unimodal)

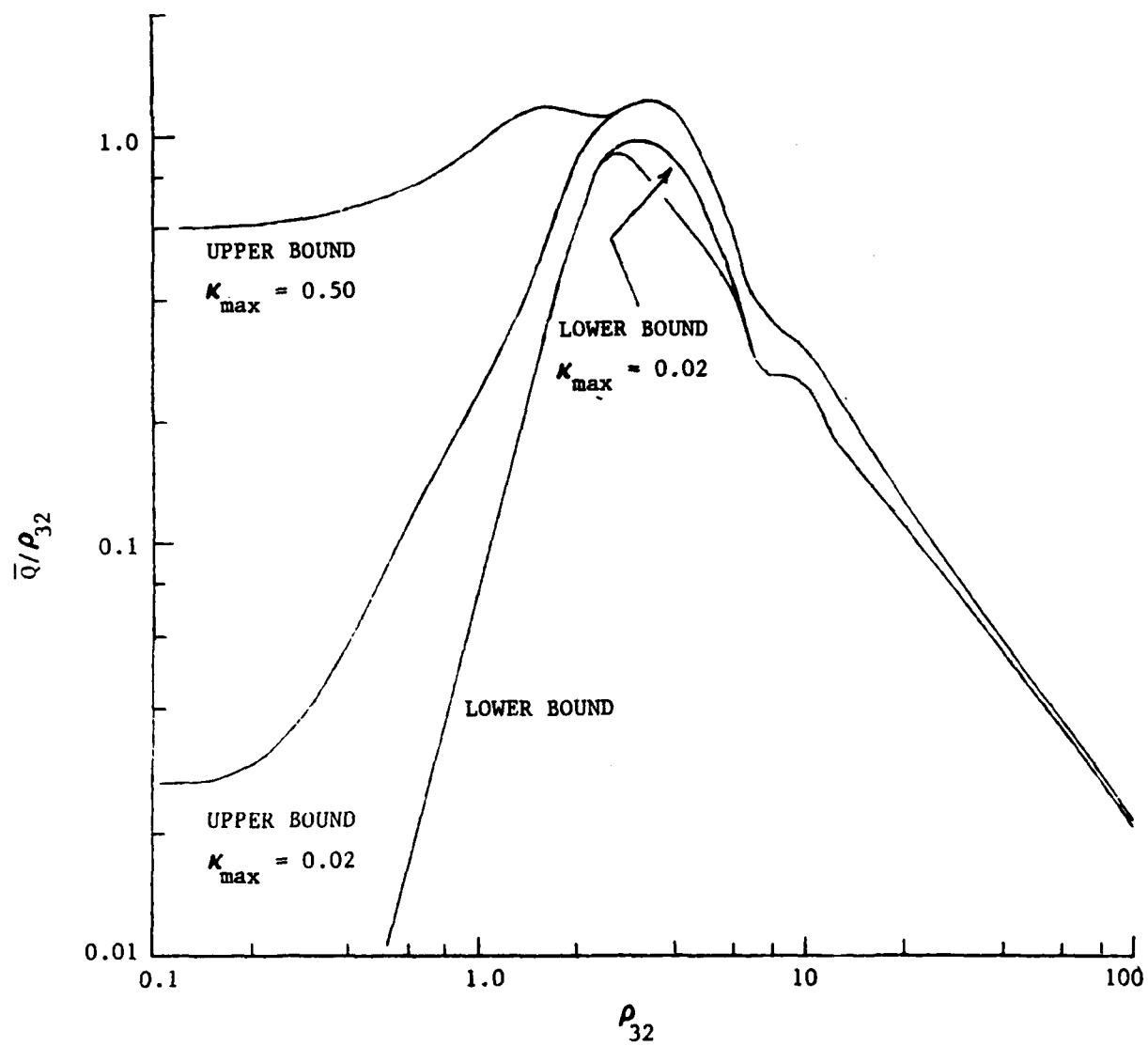


Fig. 31b. Retrieval Error Bound Caused by Ignorance of Size Distribution Function and Index of Refraction (Bimodal)

A significant feature of these results (regardless of size distribution used) is that above $\rho_{32} \approx 2.5$, the error in \bar{Q}/ρ_{32} does not depend on κ_{\max} . Below this value, the upper bound depends strongly on κ_{\max} . At $\rho_{32} \approx 0.2$, \bar{Q}/ρ_{32} approaches a constant value that depends on κ_{\max} ($\bar{Q}/\rho_{32} \approx 0.6$ for $\kappa_{\max} = 0.5$ and $\bar{Q}/\rho_{32} \approx 0.025$ for $\kappa_{\max} = 0.02$). For the cases considered here, the ratio between the two asymptotes is more than 20.

Comparing the results for the two size distributions (Fig. 31), two differences can be noted. First, for intermediates ρ_{32} , the bimodal curve displays a somewhat wider error bound than for the unimodal case. A more significant difference between the results for the unimodal and bimodal distributions occurs on the lower branch between $\rho_{32} = 0.2$ and 0.8 for the case where $\kappa_{\max} = 0.02$. The lower bound for the bimodal distribution is higher than the bound for the unimodal distribution. The difference is caused by the use of \bar{Q}_{\min} rather than $\bar{Q} - \sigma$ to define the lower bound when $\bar{Q} - \sigma$ is negative.

4.2.5 Retrieval and Error Results

Using the unimodal results of Fig. 31, the retrieval results shown in Figs. 32 through 35 were constructed. (Almost exactly the same results were obtained using the bimodal distribution.) Figures 32 and 34 show ρ_{32} as a function of the experimentally determined value of \bar{Q}/ρ_{32} . The solid curves in these two figures are the appropriate ones to use if it is known on which of the two branches of the \bar{Q}/ρ_{32} versus ρ_{32} plot one is operating (The AFRPL experiment operates on the upper branch $\rho_{32} > 3$). For $\bar{Q}/\rho_{32} > 1.7$ (Fig. 32) or 0.95 (Fig. 34) there is no distinction between branches, and the appropriate curve to use is the dashed curve. The extension of the dashed curve below these limits is the appropriate result to use if it is not known at all on

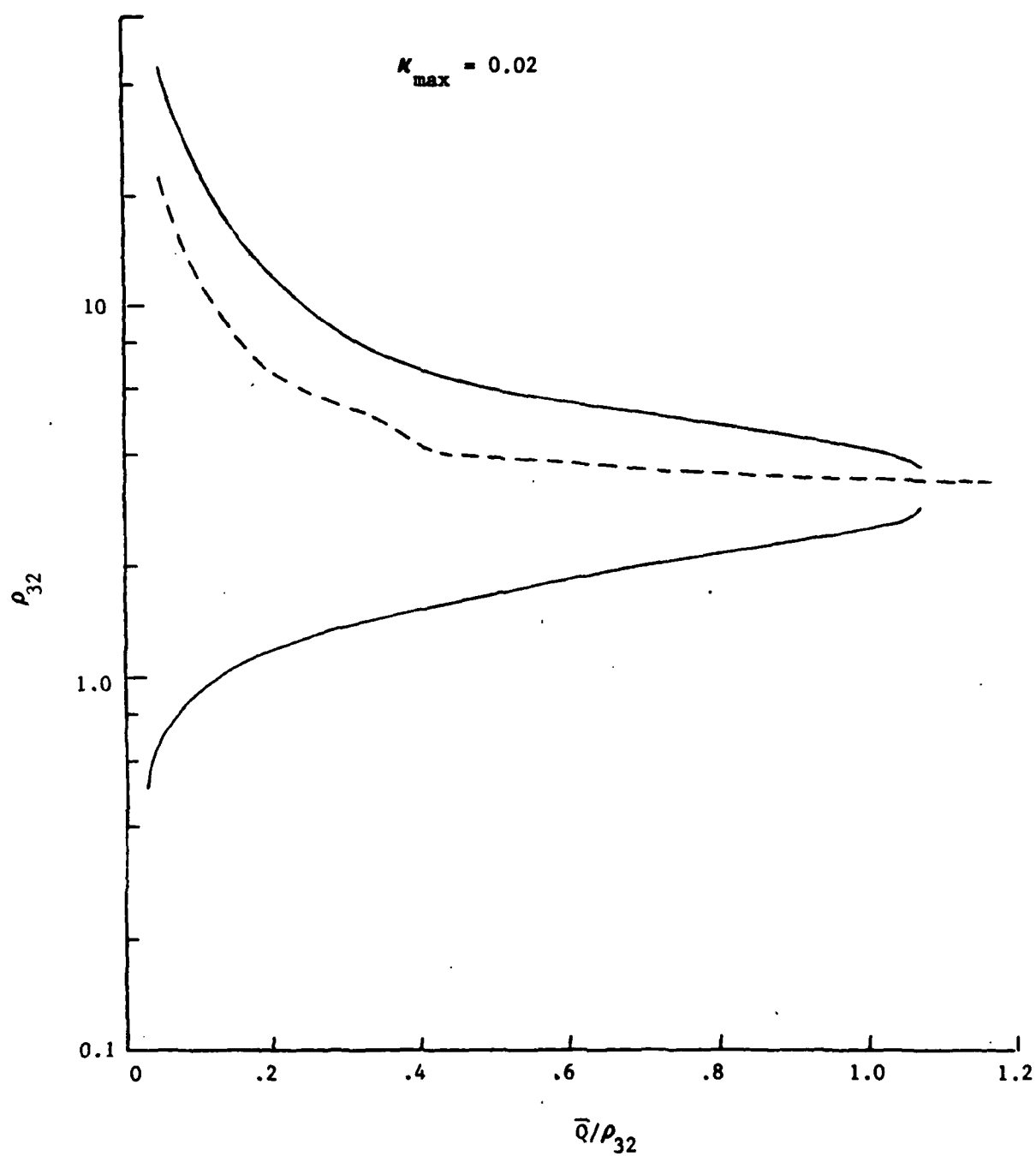


Fig. 32. ρ_{32} Retrieval Results ($\kappa_{\max} = 0.02$)

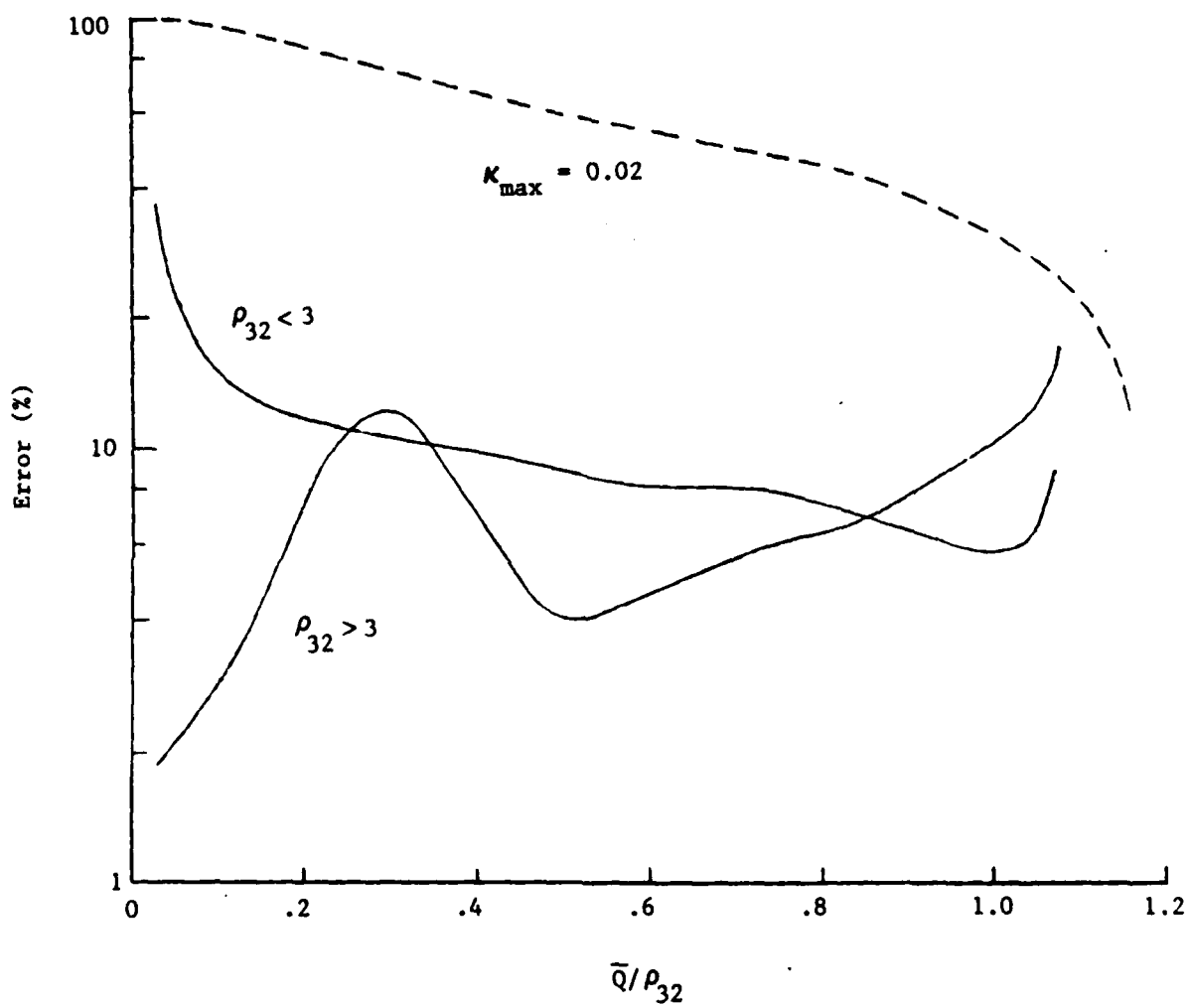


Fig. 33. ρ_{32} Error Results ($\kappa_{\max} = 0.02$)

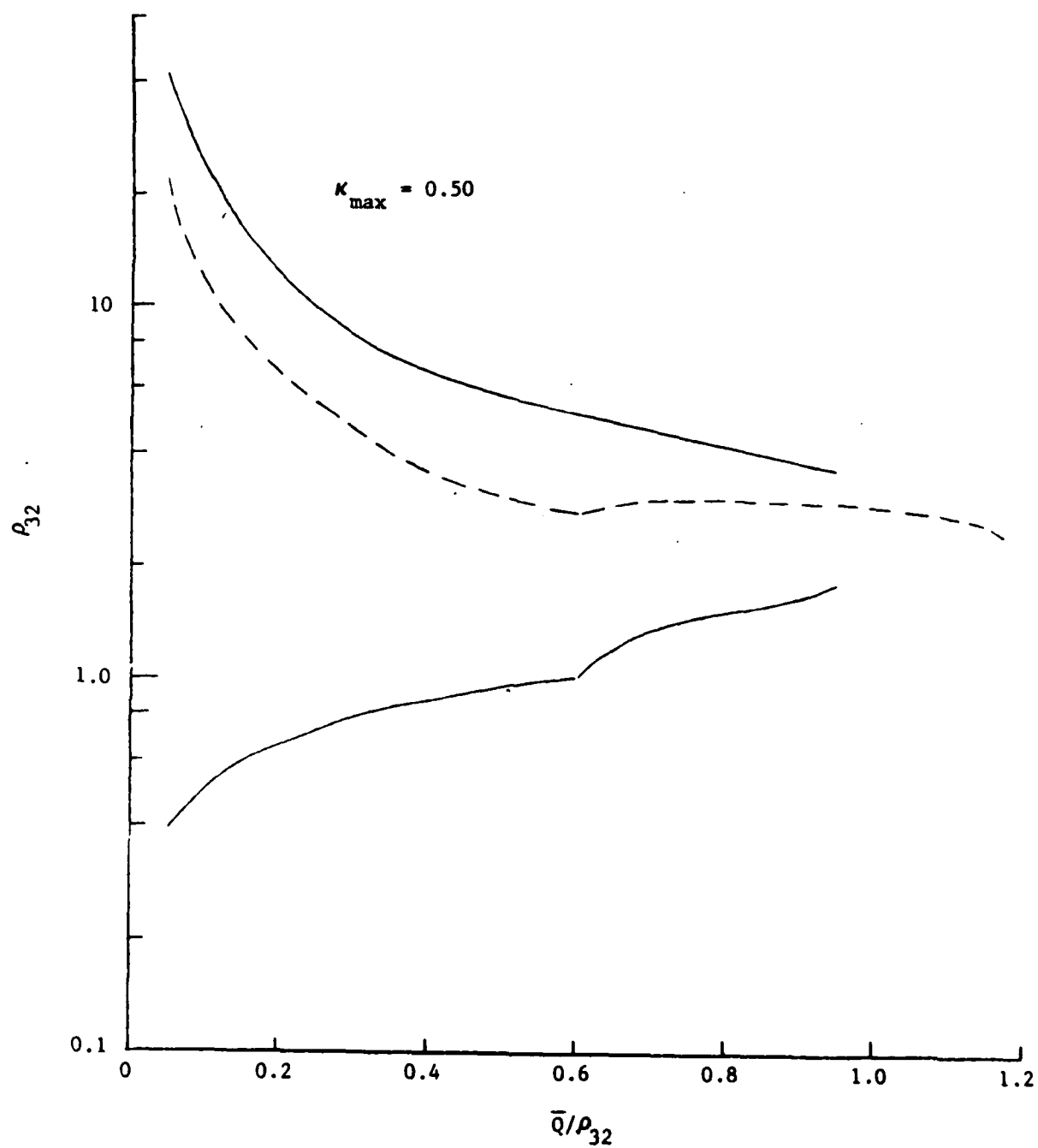


Fig. 34. ρ_{32} Retrieval Results ($\kappa_{\max} = 0.50$)

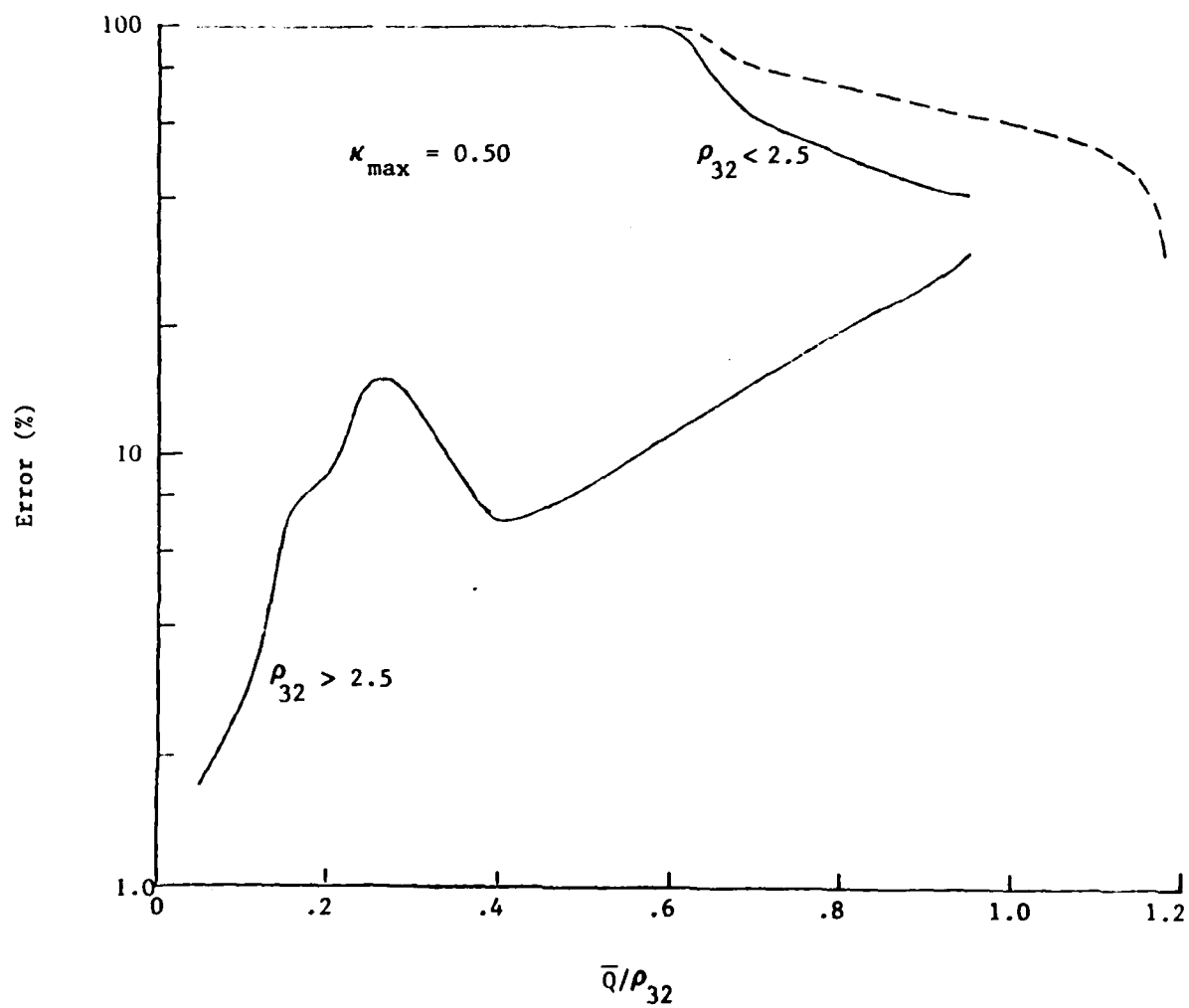


Fig. 35. ρ_{32} Error Results ($\kappa_{\max} = 0.50$)

which branch one is operating. Figures 33 and 35 show the corresponding error in ρ_{32} .

Figure 36 shows a cross-plot of the error in ρ_{32} versus ρ_{32} for both of the κ_{\max} cases. This result merely reiterates the previous conclusion that on the lower branch of the \bar{Q}/ρ_{32} curve, uncertainty in the maximum value of κ makes a large difference in the estimated retrieval error, but that on the upper branch it is not so significant. Using the nominal value $\rho_{32} = 6$ for the AFRPL experiments, the estimated retrieval errors are 4 and 7% corresponding to the assumptions, respectively, that $\kappa_{\max} = 0.02$ or 0.50.

From these curves, ρ_{32} and its error can be determined from a experimentally determined value of \bar{Q}/ρ_{32} . The volume-to-surface mean radius a_{32} is related to ρ_{32} by [Eqs. (43) and (44)]

$$\rho_{32} = 2 (n-1) \frac{2\pi}{\lambda} a_{32}$$

and contains the real part of the index of refraction as a parameter. Consequently, the estimated error in n has to be explicitly included in order to arrive at the final error estimate in a_{32} . If σ_{ρ} is the error estimate obtained from Fig. 36 and σ_n is the estimated error in n , then the error σ_a in a_{32} is

$$\frac{\sigma_a}{a_{32}} = \left(\frac{\sigma_{\rho}}{\rho_{32}}\right)^2 + \left(\frac{\sigma_n}{n-1}\right)^2. \quad (73)$$

For the present analysis, a total range of 1.70 - 1.80 has been used for n . An appropriate σ_n for this range is $\sigma_n = (1.80 - 1.70)/\sqrt{12} = 0.058$. Then, for the AFRPL experimental condition of $\rho_{32} = 6$, $\sigma_{\rho} = 0.07$ (for $\kappa_{\max} = 0.5$), the error in a_{32} is about 10%.

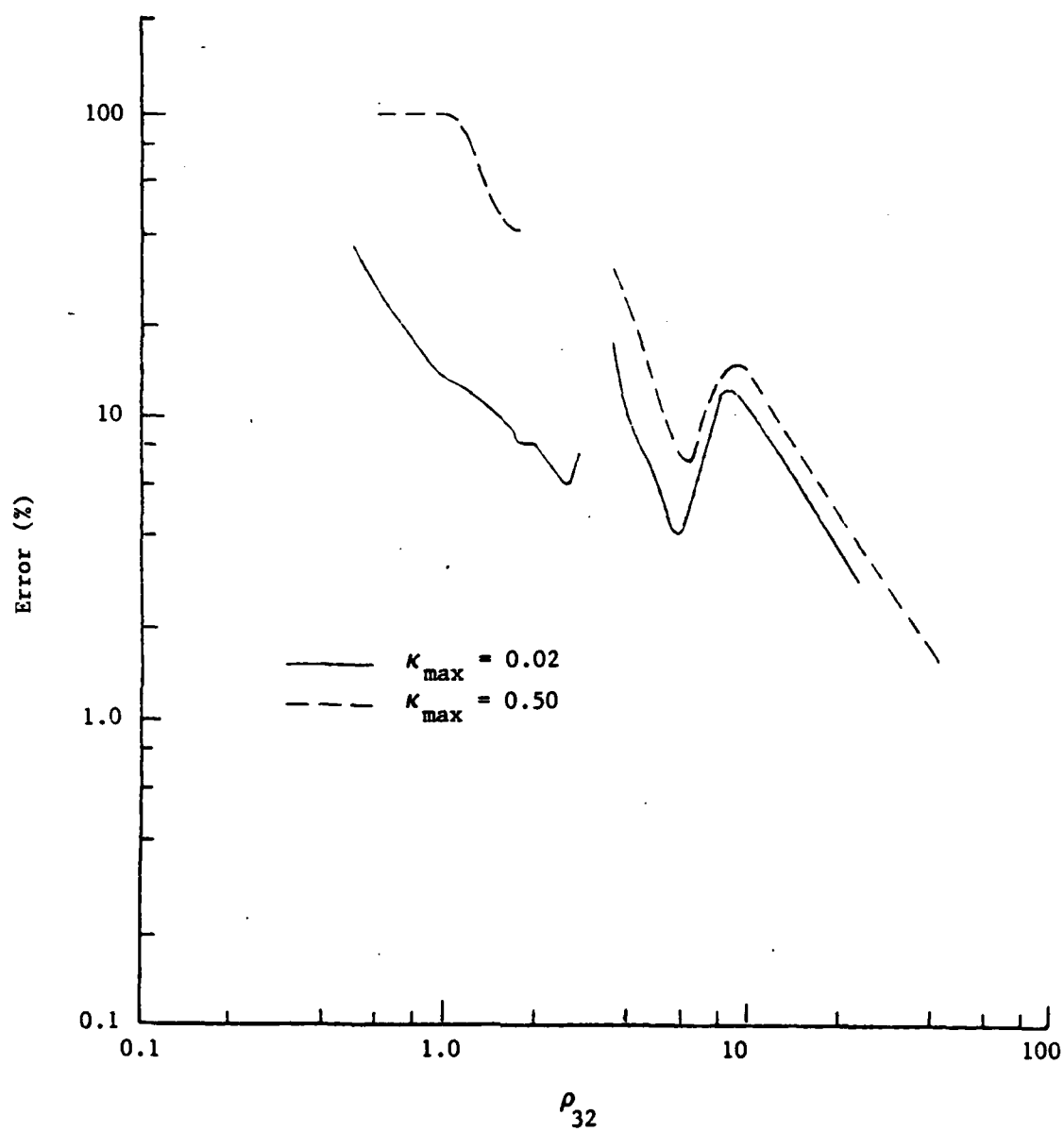


Fig. 36. ρ_{32} Error versus ρ_{32}

The essence of the one-color diagnostic presented here has been coded into a computer program (A32CODE) for analysis of AFRPL data (Ref. 23).

4.3 Two-Color Diagnostic

The basic one-color diagnostic provides for a retrieval of the volume-to-surface mean diameter a_{32} if the mass loading C_m of the plume is known. The two-color diagnostics allow the simultaneous retrieval of a_{32} and C_m . The following paragraphs report some preliminary work that has done on the two-color diagnostic and outlines how the work could be completed if interest revives.

To review, measurements of plume transmittance are made at two wavelengths, λ_1 and λ_2 , and the ratio

$$\frac{Q_1}{Q_2} = \frac{\ln \tau_1}{\ln \tau_2}$$

determined [see Eq. (42)]. From plots of Q_1/Q_2 versus a_{32} , a_{32} is determined; from plots of Q_1 or Q_2 versus a_{32} , and with a_{32} known, Q_1 or Q_2 is determined; and with Q_1 or Q_2 known, C_m is obtained from the basic transmission formula [Eq. (42)].

An important added parameter in the two-color method is the ratio of the two probe wavelengths. The analysis here has been carried out with the ratios $f = 3.16$, 5.01 , and 10 . Table 4 shows the wavelengths of commonly used lasers, and it can be seen that many pair ratios are close to these values of f .

-
23. S. J. Young, Description and Use of the Single-Color Transmissometer Plume Diagnostics Code A32CODE, AFRPL-TR-84-048, U. S. Air Force Rocket Propulsion Laboratory, Edwards Air Force Base, California, August 1984.

Table 4. Laser Wavelengths

| $\lambda(\mu\text{m})$ | Laser |
|------------------------|-----------|
| 3.51 | HeXe |
| 3.39 | HeNe |
| 1.06 | NdYAG |
| 0.633 | NeHe |
| 0.515 | Argon-ion |
| 0.325 | HeCd |
| 0.308 | HeCl |

Results for the ratio Q_1/Q_2 for the three values of f are shown in Fig. 37. ρ_{32} is for λ_1 ($\lambda_1 < \lambda_2$). As for the single-color method, an average of Q_1/Q_2 was made for 11 unimodal rectangular size distributions that cover all possible distributions for a fixed a_{32} . The upper and lower curves of these figures are $\overline{Q_1/Q_2} + \sigma$ at $m = 1.70 - 0.001$ and $\overline{Q_1/Q_2} - \sigma$ at $m = 1.80 - 0.021$, respectively, where σ is the standard deviation in $\overline{Q_1/Q_2}$. The region of retrieval lies between the valley in the upper curve and the peak of the lower curve. That is

$$0.60 < \rho_{32} < 4.0 \quad f = 3.16$$

$$0.55 < \rho_{32} < 4.0 \quad f = 5.01$$

$$0.30 < \rho_{32} < 4.0 \quad f = 10$$

Thus, the larger the wavelength ratio, the larger the retrieval range for ρ_{32} . For $f = 10$, the retrieval range covers about an order of magnitude in retrieval radius.

If one were operating with $f = 10$ and had measured a Q/Q ratio of 0.04, for example, then the retrieved ρ_{32} from Fig. 37 would be $\rho_{32} = 0.93 \pm 0.11$. The error reflects error caused by ignorance of size distribution and index of refraction (except that n is assumed to be in $1.70 - 1.80$ and $\kappa < 0.02$). The value of ρ_{32} and its error would then be used with Fig. 31 (or Figs. 32 through 35) to determine Q_1 and its error caused by ignorance of size distribution and index of refraction. For example, the value $\rho_{32} = 0.93 + 0.11$ yields an upper value of $\bar{Q}_1/\rho_{32} = 0.22$ and the value $\rho_{32} = 0.93 - 0.11$ yields a lower value of $\bar{Q}_1/\rho_{32} = 0.05$ to give a mean value and error of $\bar{Q}_1/\rho_{32} = 0.14 \pm$

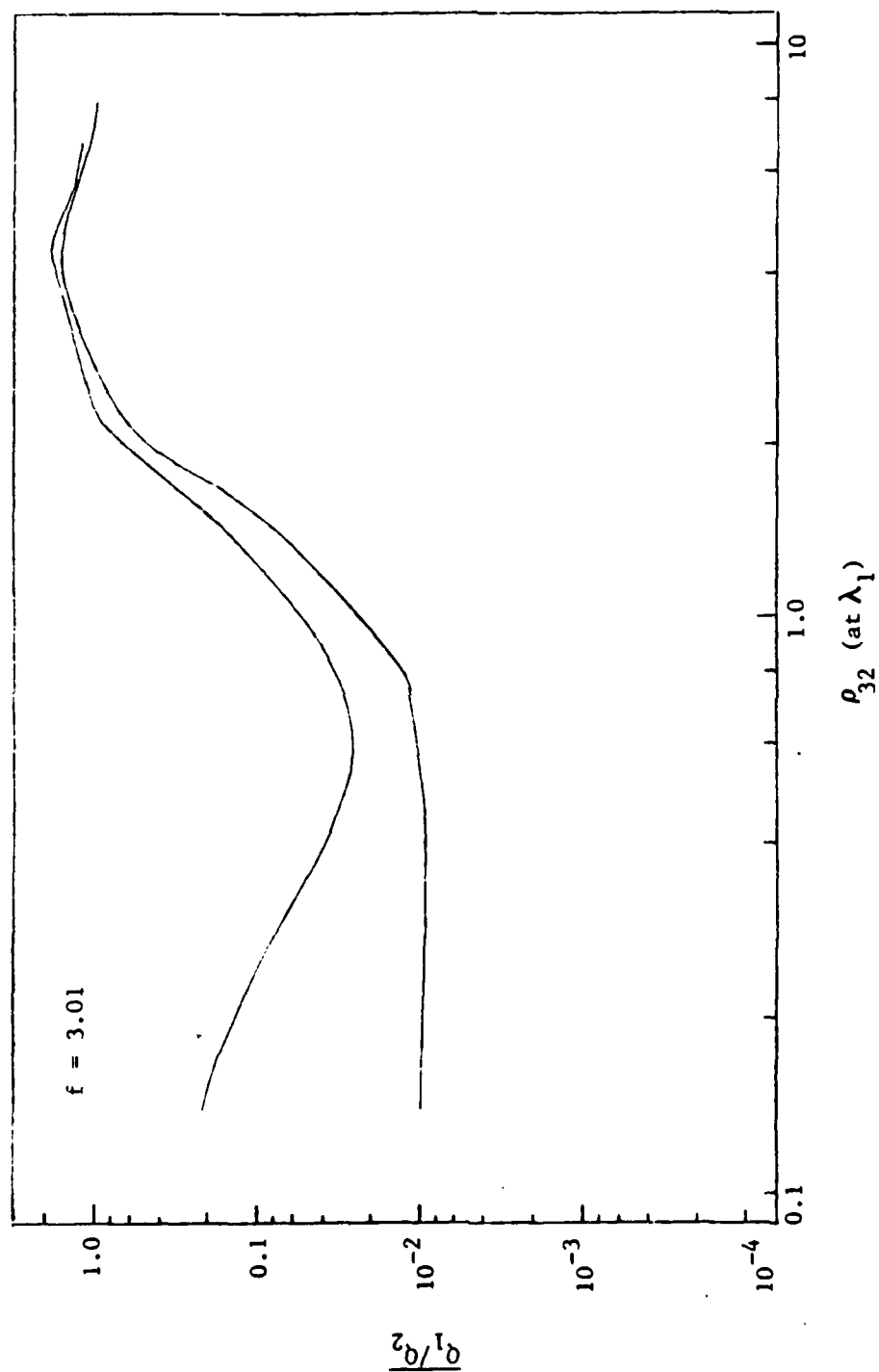


Fig. 37a. Error Bounds in Q Ratio (for $f = 3.01$)

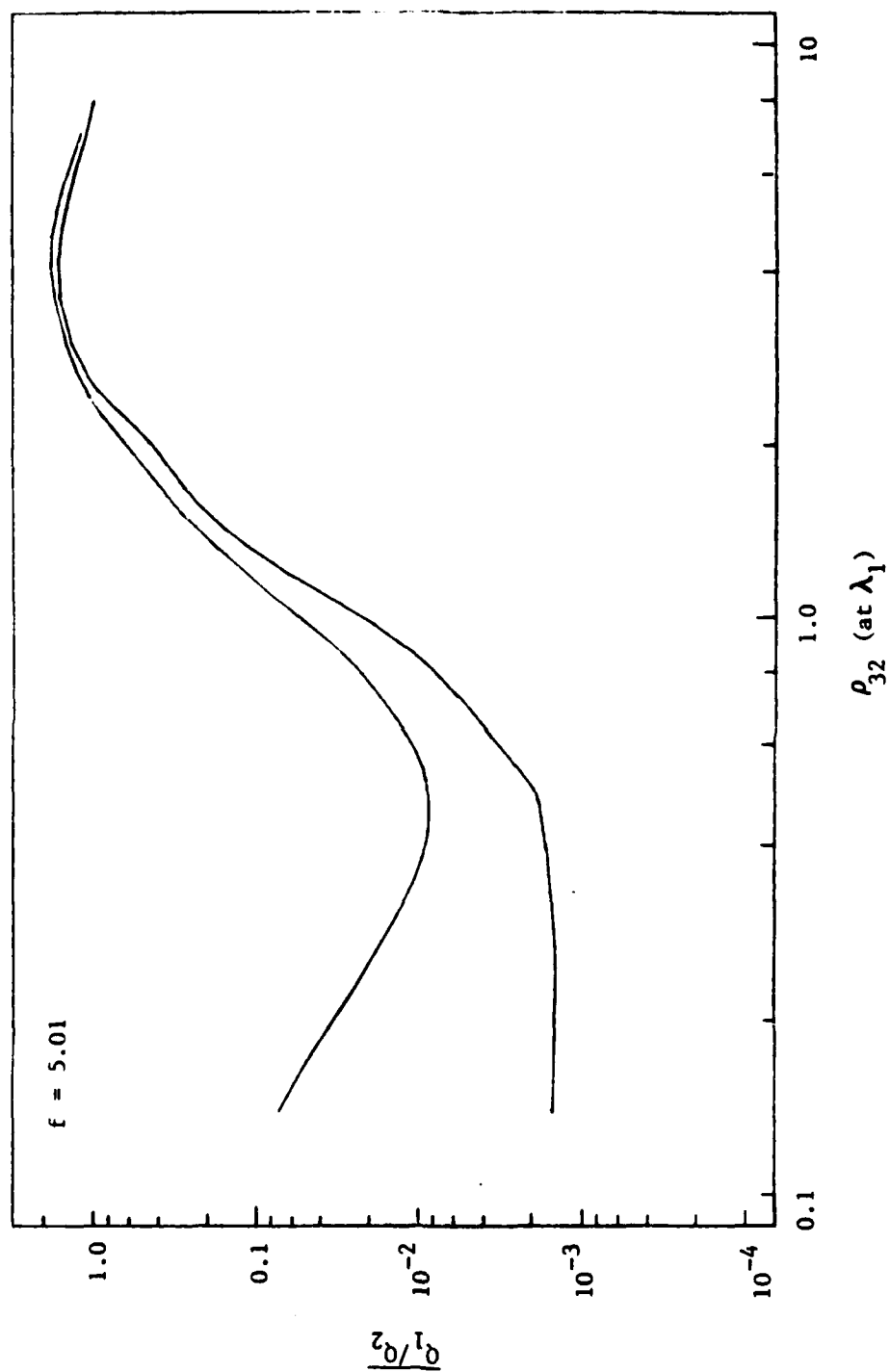


Fig. 37b. Error Bounds in Q Ratio (for $f = 5.01$)

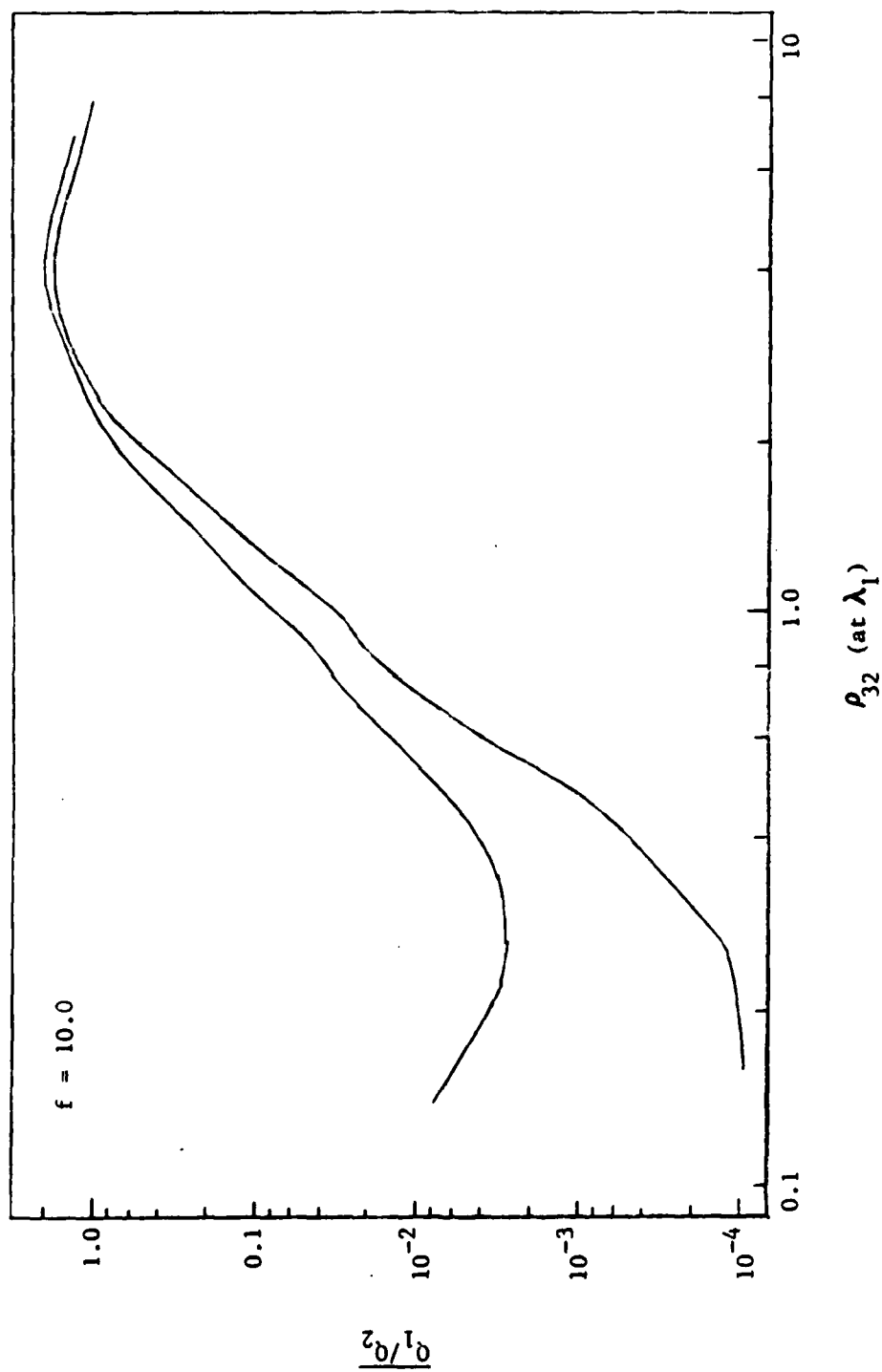


Fig. 37c. Error Bounds in Q Ratio (for $f = 10.0$)

0.08 (~ 60% error). Use of this in the transmission formula would then yield C_m to an accuracy of ~ 60%.

This magnitude of retrieval error for C_m is rather large. One of the reasons for large error is that the retrieval for ρ_{32} from \bar{Q}_1/\bar{Q}_2 occurs in the region of ρ_{32} that is below the peak of the \bar{Q}/ρ_{32} versus ρ_{32} curve (i.e., on the lower branch), and it is this region where the error in \bar{Q}/ρ_{32} is largest. This problem can be overcome by scaling the retrieved value of ρ_{32} and its error to λ_2 . In this case, since $f = \lambda_2/\lambda_1 = 10$, the scale value is $\rho_{32} = 9.3 \pm 1.1$. Then, again using Fig. 31 but using $9.3 + 1.1$ and $9.3 - 1.1$ to determine the lower and upper bounds of $\bar{Q}/\rho_{32} = .26 + 0.06$ (~ 23% error).

Actually, the retrieval error in C_m can probably be reduced even below this value by a more careful analysis. Before abandoning this problem, the following procedure was devised which, if implemented, would yield a more precise diagnostic. The main idea of the new procedure is that the retrieval of ρ_{32} and C_m would be carried out for a specified n , κ , and rectangular size distribution. In effect, plots of ρ_{32} and Q_1 (and or Q_2) versus Q_1/Q_2 (with f fixed) would be generated. These plots would then be regenerated for all n , κ , and size distributions. From this manifold of plots, the mean value of ρ_{32} (and its standard deviation) and Q_1 (and its standard deviation) would be calculated. The final result would be $\rho_{32} + \sigma$ and $\rho_{32} - \sigma$ on a single plot versus Q_1/Q_2 ; $Q_1 + \sigma_{Q_1}$ and $Q_1 - \sigma_{Q_1}$ on a single plot versus Q_1/Q_2 ; and $Q_2 + \sigma_{Q_1}$ and $Q_2 - \sigma_{Q_2}$ on a single plot versus Q_1/Q_2 . In application, one would measure Q_1/Q_2 and go directly to the three plots to determine ρ_{32} , Q_1/Q_2 and their associated errors. From ρ_{32} , one calculates s_{32} as in the one-color method. From Q_1 and Q_2 , one determines two (hopefully consistent) values of C_m via the measured τ_1 , τ_2 , and transmission formula, Eq. (42).

REFERENCES

1. S. J. Young, Inversion of Plume Radiance and Absorptance Data for Temperature and Concentration, AFRPL-TR-78-60, U.S. Air Force Rocket Propulsion Laboratory, Edwards Air Force Base, California, 29 September 1978.
2. C. C. Limbaugh, W. T. Bertrand, E. L. Kiech, and T. G. McRae, Nozzle Exit Plane Radiation Diagnostic Measurements of the Improved Transtage Liquid Rocket Injector Program, AEDC-TR-79-29, ARO Inc., Arnold Engineering Development Center, Arnold Air Force Station, Tennessee, March 1980.
3. S. J. Young, Random Error Propagation Analysis in the Plume Diagnostic Code EMABIC, AFRPL-TR-81-59, U.S. Air Force Rocket Propulsion Laboratory, Edwards Air Force Base, California, July 1981.
4. S. J. Young, Multicolor Inversion Diagnostic for Tactical Motor Plumes, AFRPL-TR-80-30, U.S. Air Force Rocket Propulsion Laboratory, Edwards Air Force Base, California, May 1980.
5. S. J. Young, User's Manual for the Plume Signature Code EAPROF, AFRPL-TR-81-08, U.S. Air Force Rocket Propulsion Laboratory, Edwards Air Force Base, California, January 1981.
6. S. J. Young, Retrieval of Flow-Field Gas Temperature and Concentration of Low-Visibility Propellant Rocket Exhaust Plumes, AFRPL-TR-82-13, U.S. Air Force Rocket Propulsion Laboratory, Edwards Air Force Base, California, March 1982.
7. S. J. Young, Retrieval of Flow-Field Temperature and Concentration of Low-Visibility Propellant Rocket Exhaust Plumes, AFRPL-TR-82-038, U.S. Air Force Rocket Propulsion Laboratory, Edwards Air Force Base, California, January 1983.
8. S. J. Young, User's Manual for the Flow-Field Diagnostic Code EMABIC, AFRPL-TR-82-037, U.S. Air Force Rocket Propulsion Laboratory, Edwards Air Force Base, California, February 1983.
9. S. Twomey, Introduction to the Mathematics of Inversion in Remote Sensing and Indirect Measurements, Elsevier, New York, 1977.
10. C. B. Ludwig et al., Standardized Infrared Radiation Model (SIRRM), AFRPL-TR-81-54, U.S. Air Force Rocket Propulsion Laboratory, Edwards Air Force Base, California, August 1981; American Institute of Physics Handbook, McGraw Hill, New York, 1957.
11. D. Diermendjian, Electromagnetic Scattering on Spherical Polydispersions, Elsevier, New York, 1969.

12. S. Twomey, J. Comp. Physics 18, 188 (1975).
13. M. Z. Hansen, Applied Optics 19, 3441 (1980).
14. T. D. McCay et al., Laser Mie Scattering Measurements of Particulate Size in Solid Rocket Motor Exhaust, JANNAF 12th Plume Technology Meeting, November 1980.
15. E. Trakhovsky et al., Applied Optics 21, 3005 (1982).
16. J. W. L. Lewis et al., Determination of the Size Distribution Function for Particle in a Hypersonic Flow Field, AEDC-TR-77-101, ARO Inc., Arnold Engineering Development Center, Arnold Air Force Station, Tennessee, July 1978.
17. B. P. Curry et al., Development of Mie Scattering Techniques for In-Situ Particle Diagnostics at AEDC, AEDC-TR-80-3, ARO Inc., Arnold Engineering Development Center, Arnold Air Force Station, Tennessee, November 1980.
18. Ariessohn et al., Applied Optics 19, 3775 (1980).
19. Dobbins and Jizmagian, J. Opt. Soc. Amer. 56 1345 (1966).
20. Dobbins and Jizmagian, J. Opt. Soc. Amer. 56, 1351 (1966).
21. The Infrared Handbook, Wolf and Zissis, editors, Office of Naval Research, Department of the Navy, Washington D.C., 1978.
22. W. L. Konopka et al., Infrared Optical Properties of Al_2O_3 Rocket Particles, preprint, Grumman Aerospace Corporation Bethpage, New York, 1983.
23. S. J. Young, Description and Use of the Single-Color Transmissometer Plume Diagnostics Code A32CODE, AFRPL-TR-84-048, U.S. Air Force Rocket Propulsion Laboratory, Edwards Air Force Base, California, August 1984.

